Chemical Engineering Report Series
Kemian laitetekniikan raporttisarja No. 51
Espoo 2006

DEVELOPMENT AND VALIDATION OF MASS TRANSFER MODELS FOR THE DESIGN OF AGITATED GAS-LIQUID REACTORS

Marko Laakkonen

TEKNILLINEN KORKEAKOULU
TEKNISKA HÖGSKOLAN
HELSINKI UNIVERSITY OF TECHNOLOGY
TECHNISCHE UNIVERSITÄT HELSINKI
UNIVERSITE DE TECHNOLOGIE D'HELSINKI

Chemical Engineering Report Series
Kemian laitetekniikan raporttisarja No. 51
Espoo 2006

DEVELOPMENT AND VALIDATION OF MASS TRANSFER MODELS FOR THE DESIGN OF AGITATED GAS-LIQUID REACTORS

Marko Laakkonen

Dissertation for the degree of Doctor of Science in Technology to be presented with due permission for public examination and debate in Auditorium MK 1 at Helsinki University of Technology (Espoo, Finland) on the 10th of November, 2006, at 12 noon.

Helsinki University of Technology
Department of Chemical Technology
Laboratory of Chemical Engineering and Plant Design

Teknillinen korkeakoulu
Kemian tekniikan osasto
Kemian laitetekniikan ja tehdassuunnittelun laboratorio

Distribution:
Helsinki University of Technology
Laboratory of Chemical Engineering and Plant Design
P. O. Box 6100
FIN-02015 HUT
Tel. + 358-9-451 2634
Fax. +358-9-451 2694
E-mail: marko.laakkonen@tkk.fi

ISBN 978-951-22-8460-3
ISBN 951-22-8460-X
ISSN 1236-875X

Otamedia Oy
Espoo 2006

ABSTRACT

Mechanical agitation is used commonly in gas-liquid reactors to improve the homogeneity of dispersion and to enhance the transfer of reacting compounds between gas and liquid. The design and scaleup of gas-liquid reactors is problematic due to non-ideal mixing, heat and mass transfer limitations. In this work, phenomenological models were developed and validated against experiments to investigate local gas-liquid mass transfer in agitated tanks. The aim was to develop more generalized and reliable simulation tools for agitated gas-liquid reactors.

Gas-liquid hydrodynamics and mass transfer are related complicatedly to bubble size. Local Bubble Size Distributions (BSD) were measured from several systems in agitated laboratory tanks. The measurements revealed a wide range of existing bubble sizes and a significant spatial inhomogeneity of BSDs. The comparison between capillary suction probe, phase Doppler anemometry and photography showed that BSDs are biased due to limitations of experimental techniques.

A dynamic multiblock model with a limited number of ideally mixed subregions was developed to investigate the inhomogeneity of dispersion. Mass transfer fluxes were modelled based on the two-film theory and simplified solution of Maxwell-Stefan diffusion. Local BSDs and mass transfer areas were solved from the population balances for bubbles by the method of classes. Unknown parameters in phenomenological bubble breakage, coalescence, turbulent slip and mass transfer models were fitted against experiments. The multiblock model was used to describe macroscopic inhomogeneities of dispersion in the fitting.

The results show that multiblock stirred tank model is an excellent tool for the testing and validation of closure models. The adjusted models describe local BSDs, gas holdups and mass transfer rates under varying agitation conditions and physical properties of dispersion in a limited range. Due to complexity of gas-liquid agitation measured local BSDs alone are not however sufficient for the validation of mechanistic closure models. More basic research and isolated experiments are needed for this.

A comparison between multiblock and CFD simulations shows that multiblock model is an optimal trade-off between the accuracy and CPU time, when local mass transfer rates are of interest. The simulations with the validated models predict a significant inhomogeneity of mass transfer, which mostly results from the spatially varying gas-liquid interfacial areas. The developed models relate mass transfer to local physical properties and micro-scale turbulence. They are less dependent on vessel size and geometry than traditional k_La-correlations and therefore suitable for detailed reactor scale-up and design studies.

The validated population balance and mass transfer closures for aqueous xanthan systems together with the bioreaction kinetics from literature were incorporated to multiblock fermenter model to investigate batch xanthan fermentation. The simulations show the need of population balances for the detailed investigation of reactive, viscous gas-liquid dispersions in which mass transfer and mixing limitations are present. The model describes the effects of mixing on reactor performance successfully. The results highlight the potential of multiblock modelling for the detailed investigation of complex multiphase reactors.

PREFACE

The project for this thesis started in August 2001. The work was carried out at Helsinki University of Technology, Laboratory of Chemical Engineering and Plant Design.

I want to thank Professor Juhani Aittamaa for supervising this thesis and for organizing interesting research projects and cooperation with industry.

Co-authors Pasi Moilanen, Ville Alopaeus, Petri Uusi-Kyyny, Juha-Pekka Pokki, Tatu Miettinen, Markus Honkanen, Pentti Saarenrinne and Kari Saari are acknowledged for their ideas and contributions.

Asta Nurmela, Suvi Jussila, Elina Nauha and Olli Visuri deserve thanks for their contributions to laboratory experiments.

Sirpa Aaltonen and Lasse Westerlund are warmly thanked for help with administrative issues.

The staff in our department's mechanical and electrical workshops is acknowledged for their expertise in building measurement devices.

Financial support from the Academy of Finland through the Graduate School of Chemical Engineering (GSCE) and research projects funded by the National Technology Agency of Finland and several Finnish companies is acknowledged.

Finally I want to thank my parents and sisters for patience.

Espoo 20.10.2006

Marko Laakkonen

LIST OF PUBLICATIONS

This thesis is based on the following publications (Appendices I – VIII), which are referred to in the text by their roman numerals

[I] Laakkonen, M., Pokki, J.-P., Uusi-Kyyny, P., Aittamaa, J., Vapour – Liquid equilibrium for the 1-butene + methanol, + ethanol, + 2-propanol, + 2-butanol and + 2-methyl-2-propanol systems at 326 K, *Fluid Phase Equilibria* **206**(1-2) (2003) 237-252.

[II] Laakkonen, M., Moilanen, P., Aittamaa, J., Local bubble size distributions in agitated vessels, *Chem. Eng. J.* **106**(2) (2005) 133-143.

[III] Laakkonen, M., Moilanen, P., Miettinen, T., Saari, K., Honkanen, M., Saarenrinne, P., Aittamaa, J., Local bubble size distributions in agitated vessels - Comparison of three experimental techniques, *Chem. Eng. Res. Des.* **83A1** (2005) 50-58.

[IV] Laakkonen, M., Honkanen, M., Saarenrinne, P., Aittamaa, J., Local bubble size distributions, gas-liquid interfacial area and gas holdups in a stirred vessel with particle image velocimetry, *Chem. Eng. J.* **109**(1-3) (2005) 37-47.

[V] Laakkonen, M., Alopaeus, V., Aittamaa, J., Validation of bubble breakage, coalescence and mass transfer models for gas-liquid dispersion in agitated vessel, *Chem. Eng. Sci.* **61**(1) (2006) 218-228.

[VI] Laakkonen, M., Moilanen, P., Alopaeus, V., Aittamaa, J., Modelling local bubble size distributions in agitated vessels, accepted for publication in Chemical Engineering Science.

[VII] Laakkonen, M., Moilanen P., Alopaeus, V., Aittamaa J., Dynamic modeling of local reaction conditions in an agitated aerobic fermenter, *AIChE J.* **52**(5) (2006) 1673-1689.

[VIII] Laakkonen, M., Moilanen P., Alopaeus, V., Aittamaa, J., Modelling local gas-liquid mass transfer in agitated vessels in Proceedings of *12th European Conference on Mixing*, eds. Magelli, F., Baldi, G., Brucato, A., Bologna, Italy, 27-30 June, 2006, pp. 193-200.

AUTHOR'S CONTRIBUTION

[I] The author carried out the experiments, derived the error analysis method, analysed the results and wrote the paper together with co-authors.

[II] The author planned the experiments together with co-authors, analysed the results and wrote the paper.

[III] The author planned the experiments together with co-authors, analysed the results and wrote the paper.

[IV] The author planned the experiments together with co-authors, developed the bias correction, analysed the results and wrote the paper.

[V] The author implemented the computer code, fitted the models and wrote the paper.

[VI] The author planned the experiments, developed the analysis method, implemented and fitted the models and wrote the paper.

[VII] The author planned the experiments together with co-authors, analysed the experiments, implemented and adjusted the models, made multiblock fermenter simulations and wrote the paper.

[VIII] The author planned the experiments, implemented and fitted the model and wrote the paper.

TABLE OF CONTENTS

1. INTRODUCTION

Mechanically agitated gas-liquid reactors are widely used in chemical, biochemical, petroleum, mining, pulp and paper industries. Oxidations, hydrogenations and aerobic fermentations are typical examples of stirred tank processes (Zlokarnik, 2001; Ranade, 2002). Agitation improves the homogeneity of mixture and enhances heat and mass transfer improving the flexibility and control of reactor performance. Even small improvements in reactor capacity or selectivity of reaction can result into remarkable savings in process economy.

The scaleup and design of agitated gas-liquid reactors is demanding, because chemical and microbiological reactions are related complicatedly to heat, mass and momentum transfer. Controlling phenomena vary with the reactor size. Reactor scale-up has trusted traditionally on semi-empirical correlations, which are based on vast experimentation. These correlations are extremely useful for the analysis of reactors, but they typically consider only vessel-averaged properties, are applicable to specific vessel geometries and can seldom be used for the testing of new reactor concepts. Large industrial reactors are often strongly inhomogeneous (Ranade, 2002; Gentric et al. 2005). Significant inhomogeneities exist even in laboratory scale tanks (Calderbank, 1958; Barigou and Greaves, 1992a, 1992b, 1996). Physical reactor models, which consider the inhomogeneity of dispersion, provide efficient means for reactor design and scale-up.

Gas-liquid mass transfer is a common rate-limiting step of reactor performance. It is related complicatedly to liquid flow fields (Middleton and Smith, 2004). Mass transfer is described most commonly based on overall mass transfer coefficients (k_La). k_La-correlations have been popular, because the measurement and modelling of mass transfer area is difficult (Calderbank, 1958; Sridhar and Potter, 1980; Middleton and Smith, 2004; Garcia-Ochoa and Gomez, 2005). Mass transfer fluxes and areas originate from different phenomena and should be modelled separately. They should be related to local micro-scale turbulence and physical properties of dispersion in order to predict gas-liquid mass transfer in an arbitrary chemical system, vessel size and geometry.

Local gas-liquid mass transfer areas are obtained readily from Bubble Size Distributions (BSD), which are known to vary in agitated tanks (Barigou and Greaves, 1992a; 1992b; 1996, Khare and Niranjan, 1995; Machon et al. 1997; Alves et al. 2002a). Population balances (PB) are a generalized approach for the modelling of local BSDs (Valentas and Amundson, 1966; Ramkrishna, 2000). Bubble breakage and coalescence are important phenomena and should be described by preferably phenomenological models to close the PBs. The PBs have been widely applied to bubble columns (Jakobsen et al. 2005), but rather few stirred tank studies are available (Venneker et al. 2002). There is a lack of experimental validation studies for the stirred tanks (Ranade, 2002; Khopkar et al. 2005; Lane et al. 2005). The measurement of bubble breakage and coalescence separately is difficult, but their combined effects can be investigated by measuring local BSDs from turbulent gas-liquid dispersions (Chaudhari and Hoffman, 1994). A rigorous approach for the modelling of mass transfer fluxes is to use the two-film theory and Maxwell-Stefan multicomponent diffusion model (Taylor and Krishna, 1993).

In this work, PBs for bubbles and rigorous gas-liquid mass transfer model are used to investigate local mass transfer in agitated tanks. The models are validated against experiments. The aim is to obtain more generalized and accurate tools for the design and scale-up or agitated gas-liquid reactors. The accuracy and the limitations of experimental techniques are evaluated in detail.

Phase equilibrium is a limit for the mass transfer. In the paper [I], Vapour-Liquid Equilibrium (VLE) was investigated from 1-butene – alcohol systems with a static apparatus. A method for the analysis of measurement errors was developed. In the papers [II-IV], emphasis was put to the measurement of local BSDs from agitated laboratory tanks. Several measurement techniques were tested to obtain accurate BSDs and to evaluate their benefits and limitations [III]. Paper [IV] presents a method for the simultaneous measurement of fluid flow fields, local BSDs, gas-liquid interfacial areas and gas hold-ups with Particle Image Velocimetry (PIV).

Computational Fluid Dynamics (CFD) has become a popular tool for the analysis of chemical reactors, because it allows the estimation of fluid flow fields based on momentum balances in almost any vessel size and geometry. At the moment, CFD predictions are fairly good for single-phase flows (Middleton and Smith, 2004). Multiphase CFD predictions are more uncertain and require further development and validation (Ranade et al. 2002). CFD programs together with the PBs and rigorous mass transfer models offer a great potential for the detailed analysis of local mass transfer in agitated gas-liquid reactors. At the moment, CFD is too time consuming for the fitting of unknown model parameters or investigation of long-term dynamics. These problems were addressed in the papers [V-VIII], where dynamic multiblock stirred tank model was developed for the analysis of spatial inhomogeneities of dispersion. The model was used to adjust unknown parameters in bubble breakage, coalescence, turbulent slip and mass transfer closure models [V-VIII]. In the paper [VII], multiblock model was used to analyse dynamic effects of mixing on batch xanthan fermentation.

Commercial CFD programs include few rigorous chemical engineering models and their physical property databases are very limited. The applicability of CFD for chemical engineering problems was improved by linking the validated models, physical property and component databases of Flowbat flowsheet simulator program (Aittamaa and Keskinen, 2005) to a commercial CFD program. The coupled ‘mass transfer – PB – CFD’ -model was then used to investigate local gas-liquid mass transfer in an agitated laboratory tank [VIII].

2. MEASUREMENT OF BUBBLE SIZE DISTRIBUTIONS

2.1 Experimental setup and investigated systems

Local BSDs were measured from geometrically similar, transparent 14 L (T=0.26 m) and 200 L (T=0.63 m) tanks [II-VII]. The vessel geometry is presented in Figure 1. Surface baffling is an exception to the standard vessel configuration. It minimises the surface aeration, which cannot be described easily as a source term in the stirred tank modelling. Rushton Turbine (RT) impeller ($D_I/T=1/3$) was used in other except paper [IV], where Flat-Blade Turbine (FBT) ($D_I/T=1/3$) was used. Gas was injected to the bottom of vessel below the impeller through a single tube nozzle [II, IV], metal sinter [II, III] or ring sparger [VI-VIII].

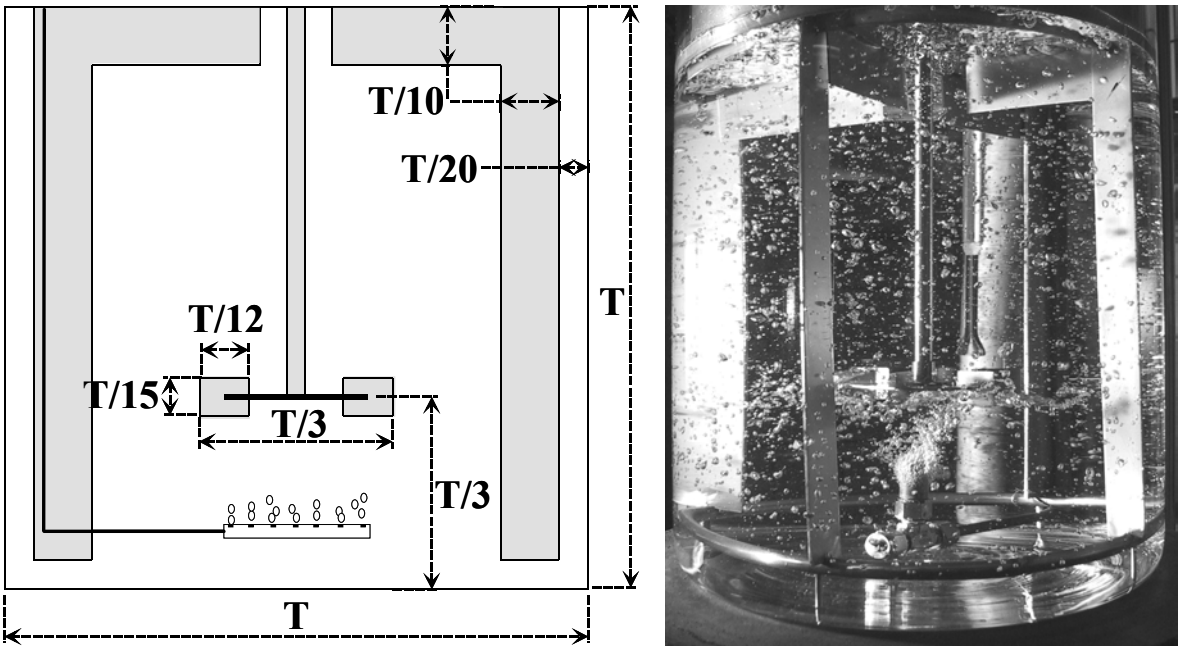

Figure 1. The laboratory stirred tank.

Local bubble size experiments are summarized in Table 1. The measurements were carried out mainly with air-water dispersion, because the hydrodynamics of even this system is poorly understood. Other systems were investigated, because earlier studies are mainly from aqueous dispersions with few exceptions (Machon et al. 1997; Schäfer et al. 2000; Hu et al. 2005). Another aim was to investigate the effect of physical properties. Agitation speeds and gas feed rates were selected so that gas was completely dispersed (Nienow et al. 1977). The vessels were operated in turbulent flow regime ($Re_I > 1 \cdot 10^4$). Due to higher apparent viscosity of liquid, aqueous xanthan experiments were carried out mostly in transient flow regime (Re_I = 20 – 2000).

In the papers [II-V], measurements were carried out with lean dispersions (Q < 0.1 vvm). This allowed easier investigation of the inner structure of dispersion and a comparison between measurement techniques. Gas feed rates were extended to 0.9 vvm in later studies [VI]-[VIII] to meet better operating conditions in industrial gas-liquid reactors. Measurement locations were selected evenly throughout the tank.

Table 1. A summary of local bubble size distribution measurements.

System	Paper	Vessel [dm^3]	Impeller	Gas feed rate [vvm]	Agitation speed [rpm]	Technique
Air – deion. water	II, III	14	RT	0.018 – 0.072	260 – 490	CSP, DI, PDA
	IV	14	FBT	0.018 – 0.072	400 – 500	DI
Air – tap water	II, III, V, VI	14	RT	0.018 – 0.7	260 – 700	CSP, DI
	II, V, VI	200	RT	0.018 – 0.9	155 – 500	CSP, DI
	IV	14	FBT	0.013 – 0.072	400 – 500	DI
Air – aq. NaCl	II	200	RT	0.052 – 0.093	250	CSP
CO_2 – n-butanol	II, III, VI	14	RT	0.018 – 0.9	260 – 700	CSP, DI
	IV	14	FBT	0.018 – 0.072	400 – 500	DI
Air – aq. starch	II	14	RT	0.29	340	CSP
	II	12	3 x RT	0.38 – 0.94	400 – 800	CSP
Air – aq. xanthan	VII	200	RT	0.1 – 0.9	155 – 475	DI

2.2 Measurement techniques

2.2.1 Measurement accuracy

A wide range of techniques is available for bubble size measurements (Boyer et al. 2002). Capillary suction probes (Barigou and Greaves 1992ab; Alves et al. 2002a), photography (Takahashi and Nienow, 1992; Machon et al. 1997; Honkanen and Saarenrinne, 2003; Galindo 2005; Hu et al. 2005) and phase Doppler anemometry (Schäfer et al. 2000) are probably the most common ones and were used also in this work. Optical probes (Chaumat et al. 2005) and viewing chamber technique (Grau and Heiskanen, 2002) are more recent techniques for the measurement of BSDs. Viewing chamber technique tries to combine the benefits of capillary and photographing technique. This method is most suitable for non-coalescing systems, because otherwise coalescence may occur in the sampling tube before the analysis with photography. In optical probe technique, the phase change around the probe tip is detected based on different refraction indexes of gas and liquid. Optical probes apply best to gas holdup measurements, but BSDs can be detected indirectly by using a multisensor probe (Guet et al. 2005). The accuracy depends on the alignment of probe relative to the direction of bubbly flow. Optical probes have therefore limited applicability for agitated tanks. The fragility of probe tip and poor wetting/dewetting properties with some chemical systems are other limitations of this technique.

The measurement accuracy of local BSDs depends on many issues, which can be related to the characteristics of measurement technique and the investigated system. A single technique can rarely detect all bubble sizes, which vary in a wide range in agitated tanks. In viscous systems, bubble size can vary from few micrometers up to the diameter of impeller (Khare and Niranjan, 1995; [VII]). This makes the measurement of representative BSDs a demanding task. Bias errors can be minimised by calibrating and adjusting the measurement apparatus carefully. In some cases, mathematical bias corrections can be developed [IV].

Not only number BSDs but also higher moments of distribution (length, area, volume etc.) should be detected accurately. This issue has been pointed out in few studies. In agitated tanks, number BSDs are skewed strongly towards small bubble size (Machon et al. 1997; [II]-[VII]). Long tails of number BSDs however include a significant fraction of the gas volume. Due to strong skewing of BSDs, sample size must be large enough (>>1000) to detect a statistically relevant number of large bubbles. Manual analysis of large bubble samples is laborious. Automatic identification algorithms are preferred but may be inaccurate especially with dense and opaque dispersions. Most techniques detect only the relative fractions of different sized bubbles. The measurement of actual bubble number, area or volume concentrations may require other techniques like optical probe.

The sensitivity of bubble size to small amounts of contaminants such as dust from air causes easily scatter to the results (Clift et al. 1978; Barigou and Greaves, 1992a). Other sources of measurement uncertainty are the inaccurate machining of vessel internals or agitation system, vibrations of impeller or uncertainties in gas feed rate or agitation speed measurements (Kraume and Zehner, 2001).

2.2.2 Capillary suction probe technique

The measurement principle of Capillary Suction Probe (CSP) is presented in Figure 2. Dispersion is sucked through a thin glass capillary, where gas bubbles transform into cylindrical slugs of equivalent volume. Light sensitive sensors that enclose the capillary detect the front and rear edges of slugs. Slug lengths are calculated from the bypassing times and the known distances between sensors.

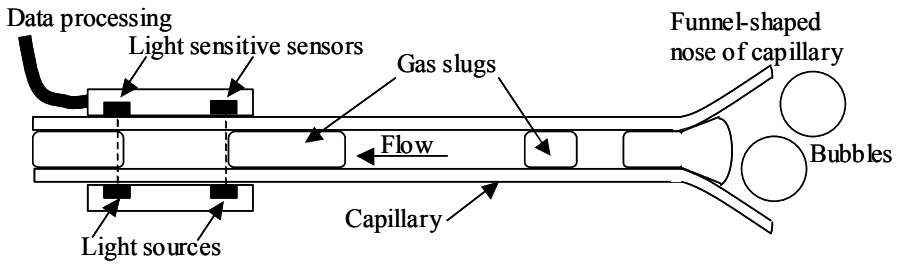

Figure 2. The measurement principle of capillary suction probe (CSP).

The accuracy of CSP has been criticized in some studies (Machon et al., 1997; Pacek and Nienow, 1995). The benefits and the limitations of CSP were discussed in the papers [II] and [III]. A weakness of CSP is that bubbles notably smaller than the capillary diameter do not transform into slugs and are not detected reliably. The maximum detectable bubble size is limited, because long slugs are prone to detection errors and can break during the transformation to the slugs or due to elongation caused by the pressure drop inside a capillary. A rule thumb is that bubbles from one to five times of the capillary diameter can be detected. The diameter of capillary should be selected carefully so that majority of existing bubble sizes can be detected. The minimum capillary diameter is limited to 0.4 mm even in low-viscosity liquids due to pressure drop and problems with mechanical plugging. The main benefits of CSP in contrast to optical techniques are its low price, simplicity and the applicability for rather opaque and dense dispersions.

The CSP experiments were carried out with Hydromess® apparatus (Genenger and Lohrengel, 1992). The details of experimental procedure are given in the paper [II]. The reproducibility tests showed generally smaller than 10 % deviation. High-speed photography showed that some breakage and coalescence occur at the nose of funnel-shaped capillary. A comparison to photography indicated that these phenomena should have minor impact on the measurement accuracy. The volume BSDs and Sauter mean diameters (d_{32}) were detected accurately from air-water dispersion, although number BSDs and arithmetic mean diameters (d_{10}) were biased due to limitation of minimum detectable bubble size [II]. The correction of measured bubble sizes based on ideal gas law and the measured pressure after the capillary improved the measurement accuracy and minimised the influence of varying suction speed on the results [II].

2.2.3 Phase Doppler Anemometry (PDA)

Phase Doppler anemometry detects bubble size based on the curvature of bubble surface (Boyer et al. 2002). Coherent laser beams are directed to intersect in the investigated position, the measurement volume. A bubble that passes the measurement volume scatters waves from two incident laser beams. Detectors receive the signal in different phases and the phase shift between these signals is proportional to bubble diameter.

The PDA was used to investigate local BSDs from air-water system in the 14 L tank [III]. The apparatus provided by Aerometrics® was used. The optical layout of apparatus allowed the detection of bubble diameters from few micrometers up to 1.5 mm. Optics could have been changed to detect a wider size range, but large bubbles are not spherical, which is the major assumption of PDA.

The PDA experiments showed that smaller than 0.1 mm bubbles exist. Laser beams found an optical path to the measurement position occasionally even in relatively dense (~1 vol-%) dispersions [III]. Some number BSDs were strongly bimodal. This seems not reasonable and has been noted to be a general tendency of PDA (Nilars et al. 2000). No improvement was

achieved even by adjusting the settings of PDA apparatus or by placing the agitated tank into a rectangular tank filled with water to eliminate optical distortions from the rounded walls of tank. It seems that the software did not eliminate inaccurate measurements completely.

2.2.4 Digital photography

The photographing experiments were carried out with a 1024 x 1280 pixel CCD camera that was a part of Particle Image Velocimetry (PIV) apparatus [III, IV] and with a 2048 x 3072 pixel CMOS Canon 300D digital systems camera [VI], [VII]. The accuracy and the limitations of photographing technique were discussed in the papers [III], [IV]. In the papers [VI] and [VII], local BSDs were measured with photography near the tank wall from dense dispersions.

A major benefit of photography compared to CSP and PDA is its wide detectable bubble size range, which depends on the resolution of CCD cell and the size of the imaged area i.e. the optics. In the present experiments the minimum detectable bubble size was approximately 0.1 mm.

The success of bubble size analysis depends on the quality of photograph and lighting conditions. Backlighting, where camera and light source are opposite each other showed to be the best [III], but was difficult to arrange with dense and opaque dispersions [VI], [VII]. The analysis of bubble sizes from the photographs is the most critical step of photography. The automatic identification of bubbles succeeded fairly well from lean dispersions (Figure 3, left) [III], [IV]. The two-level threshold identification algorithm (Chigier, 1991) failed with some overlapping (pointer A) bubbles, overexposed (pointer B) bubbles and some small bubbles, which are out of focus or image resolution (pointer C).

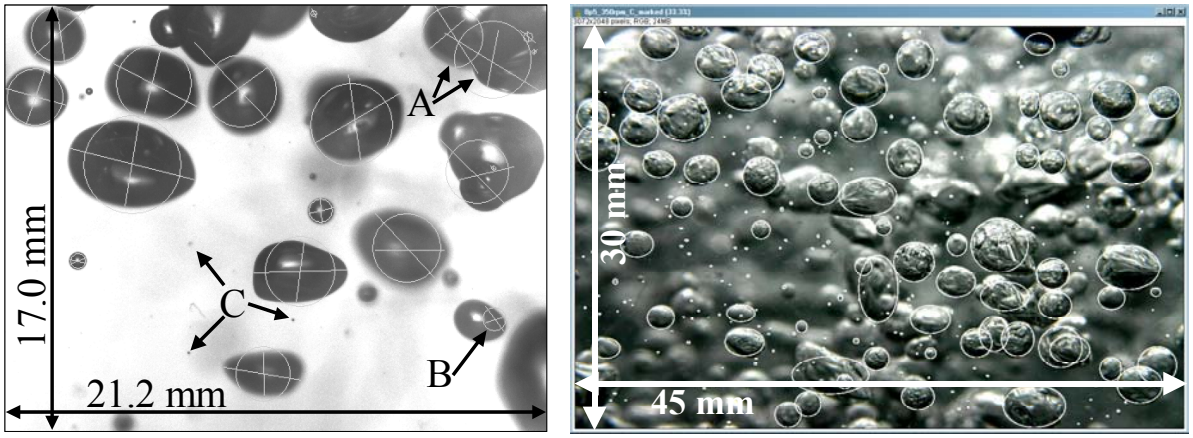

Figure 3. An illustration of automatic (left) and manual (right) bubble size analysis from the photographs.

The automatic identification of bubbles from dense dispersions is demanding, because bubbles are distorted, they overlap in the images and the background is blurred due to bubbles out of focus (Figure 3, right). Therefore manual analysis was preferred in the papers [VI] and [VII]. The success of manual bubble identification is illustrated in Figure 3 (right). The analysis of BSDs accelerated notably, when marked ellipsoidal bubbles in thresholded images were detected by using the particle analysis tool of ImageJ-1.32 freeware. The number of analysed bubbles for one BSD was 500-1500. A statistically relevant number of large bubbles in such a small sample was ensured by identifying large and small bubbles separately and then combining these two identifications by weighting with the area of image [VII]. Calibration experiments showed that large bubbles are more likely in focus than small

bubbles. This causes a slight overestimation of bubble size. Therefore measured BSDs were corrected with the probabilities for a bubble to touch the depth of focus [VI].

2.3 Analysis of bubble size measurements

The measured BSDs were processed into comparable form, because the range of detected bubble sizes and the number of sampled bubbles varied from a technique and experiment to another. Dimensionless bubble number densities are defined by

$$n(d_n) = \frac{d_{max} - d_{min}}{\Delta d_n} \frac{n_{b,n}}{\sum_{p=1}^{NP} n_{b,p}}. \tag{1}$$

and volume densities by

$$v(d_n) = \frac{d_{max} - d_{min}}{\Delta d_n} \frac{n_{b,n} d_n^3}{\sum_{p=1}^{NP} n_{b,p} d_p^3}. \tag{2}$$

Simple formulas were developed to calculate characteristic sizes and widths of bubble size classes. The sizes are calculated from

$$d_n = \frac{d_{max} - d_{min}}{\sum_{p=1}^{NP} Z^{p-1}} \left(\sum_{p=1}^{n-1} Z^{p-1} + \frac{1}{2} Z^{p-1} \right) \tag{3}$$

and the corresponding widths from

$$\Delta d_n = \frac{Z^{n-1}}{\sum_{p=1}^{NC} Z^{p-1}} \left(d_{\max} - d_{\min} \right), \tag{4}$$

where d_{min} and d_{max} are the smallest and largest observed bubble size and Z is the discretization parameter. Setting Z = 1 produces equal-sized discretization, Z < 1 gives dense discretization for large bubbles and sparse discretization for small bubbles and Z > 1 vice versa. Values larger than unity are suitable for number BSDs, which are skewed towards small bubble size. Volume BSDs are typically closer to a normally distributed so that Z can be set to unity.

A program was implemented to make the analysis experiments easier. The program reads bubble size measurements from text files, combines the results, if there are several measurements from the same position, makes bias corrections and calculates the BSDs from Eqs. (1) and (2) with an appropriate discretization from Eqs. (3) and (4). Statistical values like arithmetic d_{10} and Sauter mean bubble diameters d_{32} and standard deviation are calculated. The results are written to a text file.

2.4 Comparison of measurement techniques

Alves et al. (2002a) reviewed experimental bubble size stirred tank studies. They concluded that scatter in available bubble size measurements is significant and cannot be attributed to chemical system, variation of vessel geometry or to the accuracy of experimental technique. Pacek and Nienow (1995) compared capillary probes and photography and recommended the use of photography, because capillary diameter limits the minimum detectable bubble size. Hernandez-Aquilar et al. (2004) compared capillary and viewing chamber techniques (Grau and Heiskanen, 2002) and concluded that in general they are in good agreement.

Capillary, PDA and photographing techniques were compared to evaluate their accuracy and limitations [III]. Local BSDs were measured from the Rushton turbine agitated 14 L tank. Figures 4a and 4b present the measured local number and volume BSDs from air-water dispersion near the wall above the impeller. Only the volume BSDs from CSP and photography show good agreement. This was a general trend in air-water system in all investigated locations of tank. In CO_2 – n-butanol system, bubbles were small and also volume BSDs from CSP and photographing measurements showed a clear difference. Evidently, none of the techniques detected both number and volume BSDs accurately. A limited detectable size range seems to be a major reason. The CSP cannot detect bubbles smaller than the capillary diameter, which causes the biasing of number BSDs. The PDA cannot detect larger than 1.5 mm bubbles causing a significant biasing of volume BSDs. The photography is the most promising technique, because it has the widest detectable bubble size range. The image resolution must however be sufficient to detect small bubbles. The inner structure of dispersion can be investigated only from lean and opaque dispersions.

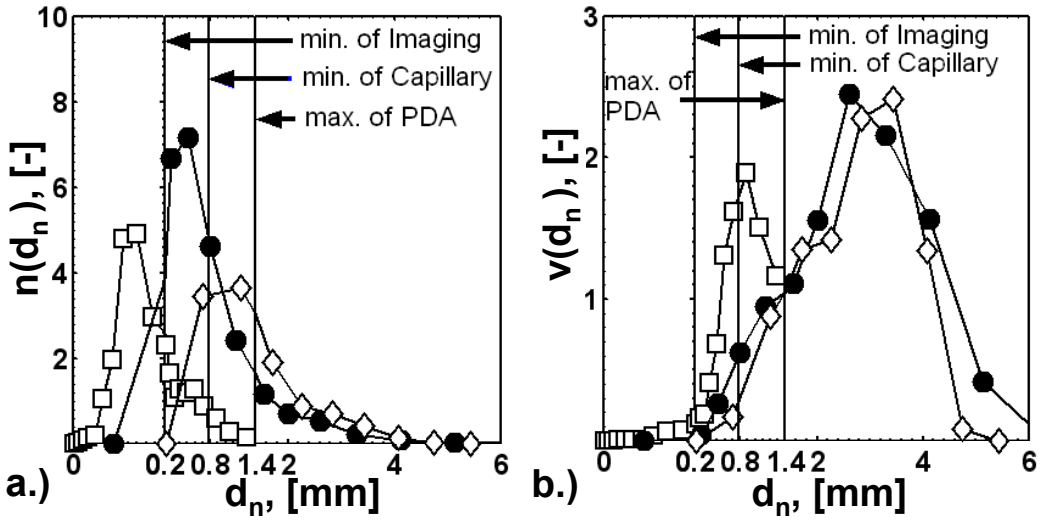

Figure 4. a.) number and b.) volume BSDs in the air-water system near the wall below the impeller, Q=0.018 vvm, N=490 rpm, PDA Photography (Imaging), Capillary probe.

2.5 Comparison to literature correlations

A quantitative comparison of local bubble size measurements to the literature is difficult, because chemical systems, vessel geometries and operating conditions vary from a study to another. In most studies (e.g. Calderbank, 1958; Alves et al. 2002a; Hu et al. 2005) vessel-averaged bubble sizes have been correlated based on the theory of Hinze (1955), although gas-liquid dispersions are inhomogeneous even in small tanks. A comparison is however tried to further evaluate present measurements.

Walter and Blanch (1986) measured bubble sizes from pipe flows and obtained the following correlation for the maximum stable bubble size

$$d_{max}/m = 1.12 \cdot \bar{\varepsilon}^{-0.4} \left(\frac{\sigma}{\rho_L}\right)^{0.6} \left(\frac{\mu_L}{\mu_G}\right)^{0.1} . \quad (5)$$

Figure 5 presents a comparison between present measurements and Eq. (5). The measured surface tension against air needed in Eq. (5) is for tap water 0.069 kg/s^2, n-butanol 0.023 kg/s^2, and aqueous xanthan 0.069 kg/s^2. The apparent viscosities of aqueous xanthan are calculated from the adjusted viscosity model [VII] based on the approach of Metzner and Otto

(1958) with shear rate 11.5·N. The vessel-averaged turbulent energy dissipation rates are evaluated based on power consumption measurements. The comparison in Figure 5 shows fair agreement with slightly higher measured values compared to Eq. (5). The fact that Eq. (5) neglects the influence of bubble coalescence could explain the difference. It is also possible that breakage mechanisms are different in pipe flows and in agitated tanks.

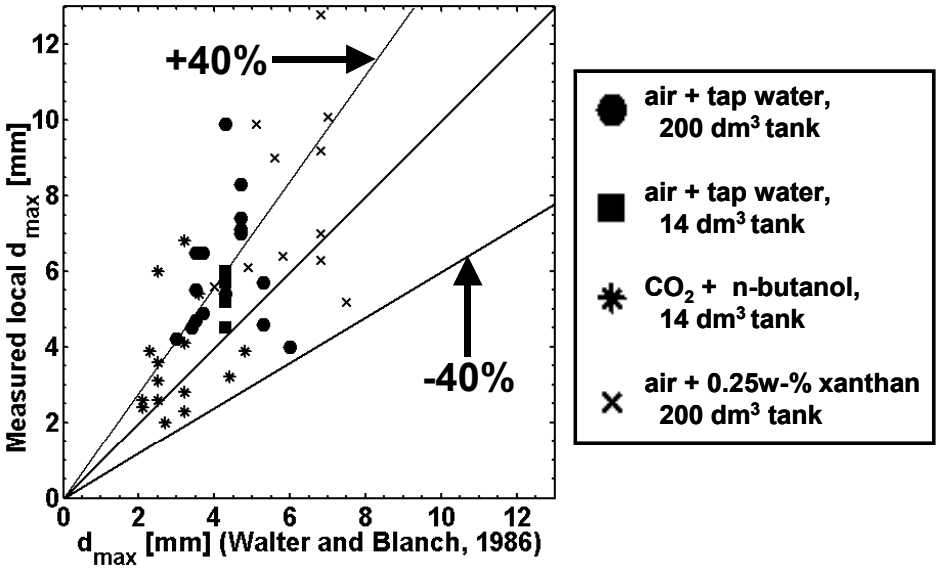

Figure 5. Measured maximum bubble diameters vs. the correlation of Walter and Blanch (1986).

The PDA experiments showed that minimum bubble size is approximately 30 μm in the air-water system. This agrees with the observations of Machon et al. (1997) and is comparable to the Kolmogorov's length scale ($=(\mu_L^3/\rho_L^3/\varepsilon)^{1/4}$) under typical agitation conditions.

Number BSDs were skewed strongly towards small bubble size in all investigated systems [II]-[VII]. Arithmetic mean bubble diameters were generally smaller than 1 mm. Sauter mean bubble diameters d_{32} were notably larger. This shows that large bubbles include a significant fraction of the overall gas volume. These observations agree with some earlier stirred tank studies (Takahashi and Nienow 1992, Machon et al. 1997). In bubble columns number BSDs are more symmetrical and the range of bubble sizes is narrower (Lehr et al. 2002; Wang et al. 2005).

Calderbank (1958) developed the following widely used correlation for vessel-averaged bubble diameters in coalescing systems

$$\overline{d}_{32}/m = 4.15 \cdot \overline{\varepsilon}^{-0.4} \left(\frac{\sigma}{\rho_L} \right)^{0.6} \overline{\alpha}_G^{0.5} + 0.0009/m, \qquad (6)$$

whwere gas holdup is included to describe the effect of coalescence. Some later correlations such as that of Alves et al. (2002a) consider the coalescence indirectly through gassed power consumption of mixing. This seems to be inadequate for dense coalescing dispersions. Measured local Sauter mean bubble diameters d_{32} are compared to Eq. (6) in Figure 6. The comparison shows that present measurements are in the same range. A significant spread mostly results from spatial inhomogeneities in the agitated tanks. Evidently, another reason is the biasing due to measurement techniques.

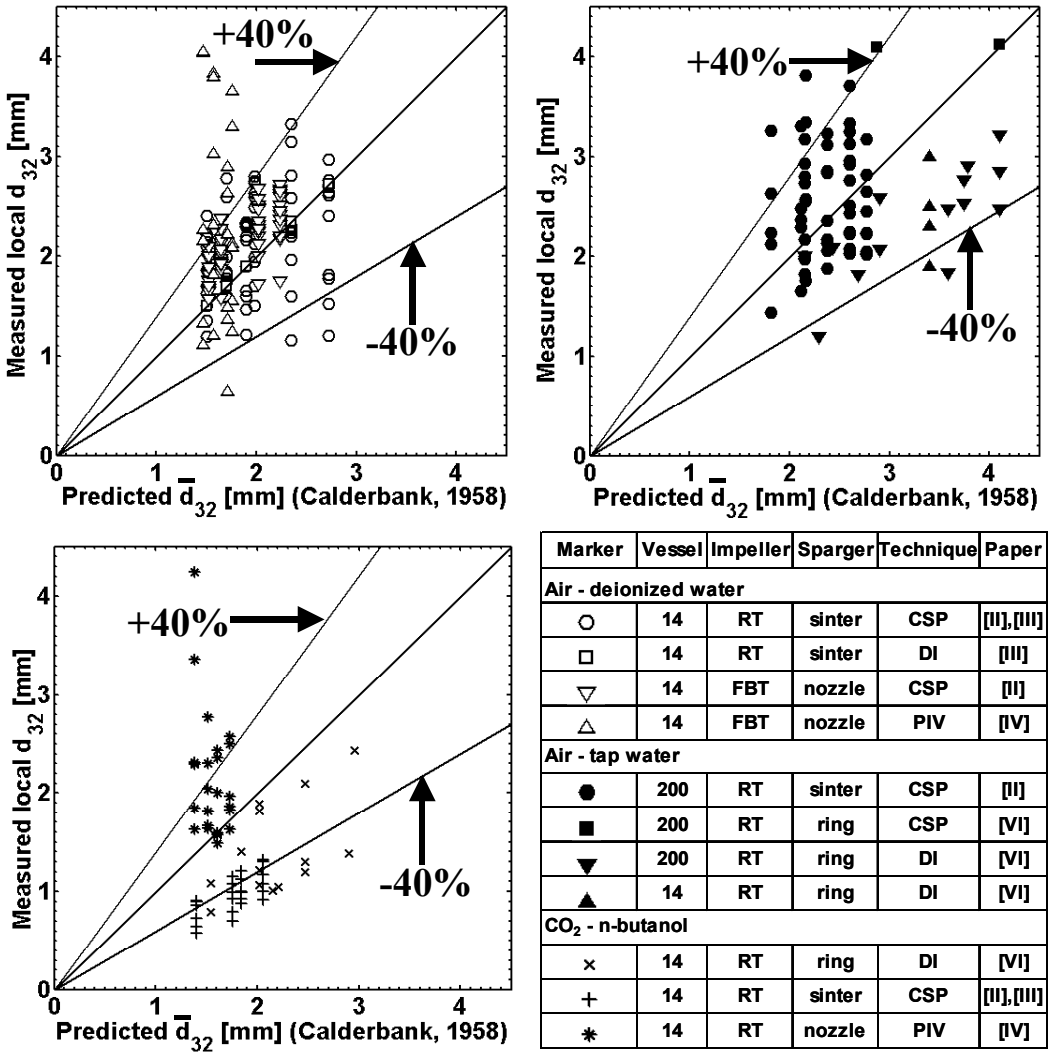

Marker	Vessel	Impeller	Sparger	Technique	Paper
Air - deionized water					
○	14	RT	sinter	CSP	[II],[III]
□	14	RT	sinter	DI	[III]
▽	14	FBT	nozzle	CSP	[II]
△	14	FBT	nozzle	PIV	[IV]
Air - tap water					
●	200	RT	sinter	CSP	[II]
■	200	RT	ring	CSP	[VI]
▼	200	RT	ring	DI	[VI]
▲	14	RT	ring	DI	[VI]
CO_2 - n-butanol					
×	14	RT	ring	DI	[VI]
+	14	RT	sinter	CSP	[II],[III]
*	14	RT	nozzle	PIV	[IV]

Figure 6. Measured local vs. predicted vessel-averaged (Eq. 6) Sauter mean bubble diameter.

2.6 Observed trends of local BSDs

The spatial variations of BSD result from local dynamic balances between bubble breakage, coalescence and transportation due to convection and slip. In a Rushton Turbine (RT) agitated tank, the structure of dispersion can be described by roughly six characteristic zones (Figure 7). The observed qualitative trends [II], [III], [V], [VI] can be summarized as follows

• **Zone Z1**: Bubbles are very small and gas holdup is low at other but high agitation speeds.

• **Zone Z2**: Gas sparger controls the bubble size and gas holdup is high.

• **Zone Z3**: Bubble size and gas holdup increase with increasing stirring speed, because bubbles are trapped by the downward flowing liquid and can then coalesce.

• **Zone Z4**: Bubbles are slightly smaller than elsewhere in the tank and their size decreases with increasing stirring speed due to high turbulence energy dissipation rates, which promote the breakage. Larger bubbles originate from trailing vortices behind impeller blades (van't Riet and Smith, 1974) or from the gas feed so that BSDs may be bimodal.

• **Zone Z5**: Bubble size may decrease (CO_2 – n-butanol, [II], [VI]) or increase (air – water, [II], [VI]; air – aqueous xanthan, [VII]) near the wall from the impeller plane towards the surface of dispersion. The decrease of bubble sizes towards surface is unexpected but agrees with some earlier observations (Machon et al. 1997, Schäfer et al. 2000). A region of low gas

holdup is generated near the wall in the vicinity of liquid surface at high gas feed, because rising bubbles concentrate towards the centre of tank and may generate secondary liquid circulation loops (Nienow et al. 1977; Khopkar et al. 2005).

• **Zone Z6**: Bubble size increases with increasing stirring speed, because bubbles are trapped by the downward liquid flow. Gas holdup increases in low-pressure region in the middle of the liquid circulation loop at high stirring speeds and gas feed rates.

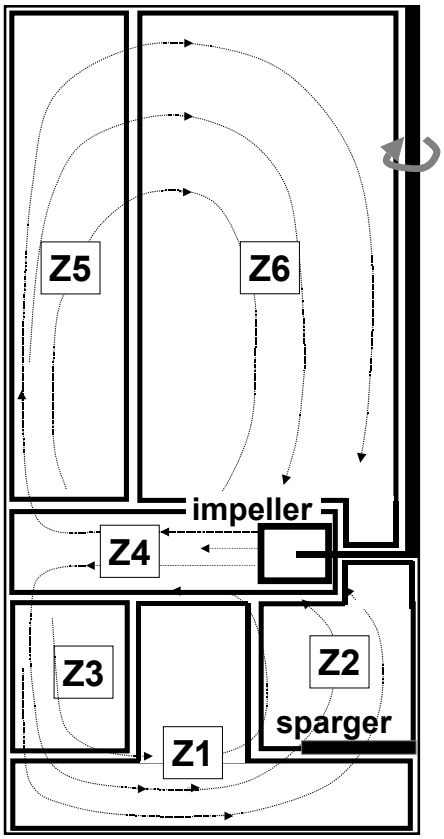

Figure 7. The characteristic zones of varying bubble size in a Rushton turbine agitated tank.

A general trend in all measurement locations was that bubble size increases with increasing gas feed rate [II-VII]. Bubbles collide and coalesce more frequently at high gas holdups and their breakage rates decrease as the power consumption of impeller decreases.

Air – tap water experiments in the vicinity of dispersion surface showed that bubbles are larger in the mid-plane between baffles and in the leeward side than in the windward side of baffle [II]. This agrees with the observations of Barigou and Greaves (1992a). Apparently, high turbulent energy dissipations promote breakage in the windward side, while low pressure causes gas accumulation and coalescence in the leeward side.

The arrangement of zones in Figure 7 is not applicable to other impeller types as they generate different flow fields. This was confirmed by comparing local BSDs from the measurements with FBT and RT impellers [II, IV]. In contrast to the experiments with RT, bubble size decreased with increasing stirring speed in all investigated locations and more homogeneous BSDs were observed with the FBT. Schäfer et al. (2000) made a similar observation from the mixtures of silicone oils with PDA.

The addition of NaCl decreases bubble size more clearly near the surface of dispersion than in the impeller discharge flow [II]. This agrees with the observations of Barigou and Greaves (1992a). The addition of electrolytes decreases the efficiency of bubble coalescence

(Chaudhari and Hoffman, 1994), which controls bubble size in coalescing systems in the quiescent regions of tank.

2.7 Simultaneous measurement of local hydrodynamic parameters

A wide range of flow visualization techniques is available for multiphase flows (Chaouki et al. 1997; Mavros, 2001; Boyer et al. 2002). Particle image Velocimetry (PIV) allows non-invasive monitoring of flow fields. It has been used in many studies for the analysis of agitated gas-liquid dispersions (Morud and Hjertager, 1996; Ranade et al. 2001; Deen et al. 2002; Khopkar et al. 2003; Aubin et al. 2004). The measurement of two-phase flow fields simultaneously with other interesting hydrodynamic parameters including BSDs, gas-liquid interfacial areas and gas holdups produces more consistent information for model validation. In the paper [IV] such a method was developed for 2D-PIV.

Gas-liquid hydrodynamics was investigated with the 2D-PIV. The dispersion was illuminated with a laser light sheet. Laser sheet illumination is necessary in flow field measurements. It also minimises the blurred image background allowing the use of automatic bubble identification algorithms. Local gas-liquid interfacial areas and gas holdups were calculated from the BSDs. The effective depth of laser light sheet was determined from the calibration experiments.

A numerical method was developed to correct the overestimations of gas-liquid interfacial area and gas holdup due to reason that large bubbles touch the laser light sheet more probably than small bubbles [IV]. The method also considers the biasing of BSDs due to reason that some bubbles touch the light sheet partially and are smaller in the images than is their actual size. Calibration experiments with varying particle size and depth of laser light sheet verified the need and the relevance of correction. The correction becomes significant at narrow depths of light sheet. A narrow light sheet is needed for accurate flow field measurements and is also favourable for automatic bubble identification, because bubbles overlap then less in the photographs.

Local gas-liquid hydrodynamics was investigated in the 14 L vessel agitated by FBT. The liquid flow fields (Honkanen and Saarenrinne, 2002) were measured simultaneously. They were utilized in the analysis of results. The PIV measurements indicate that liquid flow is directed axially towards the bottom of tank in the air – water system. This could explain why small bubbles were observed below the impeller plane. In the CO_2 – n-butanol system, instead, liquid was pumped more radially according to PIV, from the impeller tip towards the wall. Apparently, the bubbles below the impeller originated mainly from the gas distributor in these experiments. This could explain why bubbles were larger below the impeller plane in CO_2 – n-butanol than in air-water system.

3. GAS-LIQUID MASS TRANSFER EXPERIMENTS

3.1 Dissolved oxygen measurements

Mass transfer measurement techniques can be classified based on the method of how a departure from the gas-liquid equilibrium is generated. In sulfite oxidation techniques (Ruchti et al. 1985; Linek et al. 2005a) Dissolved Oxygen (DO) concentration decreases below the level of saturation, when DO and sulphite react to sulphate in a diffusion controlled slow reaction regime. Oxygen transfer rates can then be analysed based on the titration or exit gas analysis. Due to presence of salts, sulphite oxidation technique is applicable only for non-coalescing systems. Based on the Danckwerts' plot method it is possible to determine volumetric mass transfer coefficients and specific mass transfer areas simultaneously in a fast

reaction regime with this technique. In the dynamic pressure change method, small upward change of pressure (15-20 kPa) is generated to increase gas solubilities (Poizat et al. 1992). The agitation power can be transmitted to the closed tank by magnetic gearing. The concentration of dissolved gas and/or pressure is then monitored.

Dynamic gassing-in – gassing-out method (van't Riet, 1979) seems to be the most commonly used technique for mass transfer measurements nowadays. It is cheap and easy to use and was used also in this work. At the start of experiment gas feed is changed to generate a departure from equilibrium. The DO concentration vs. time is then measured until new equilibrium state is reached. A drawback of this technique is that non-ideal mixing of gas must be considered in the analysis of results. Air can be replaced with pure oxygen to generate a larger driving force.

Oxygen transfer rates were measured from air – tap water [V], [VIII] and air – aqueous xanthan dispersions [VII] in the Rushton turbine agitated 200 L vessel. The DO concentrations were measured with a polarographic probe (LT Lutron, Model DO-5510). The probe was tied on the leeward side of baffle near to liquid surface in air – water experiments and near the impeller plane in air – aqueous xanthan experiments to minimise lag due to stagnant liquid around the probe tip. The probe tip was faced upwards to avoid disturbances due to rising bubbles.

Middleton (1992) has noted that most of the published overall mass transfer coefficient ($k_L a$) data is suspect due to numerous simplifying assumptions in the analysis of experiments. Often volumetric mass transfer coefficients ($k_L a$) are determined from the measured DO concentration profiles based on the following assumptions

- Liquid film resistance controls mass transfer.
- Gas and liquid are ideally mixed.
- Concentrations of gas remain constant during the experiment.
- Pressure variations inside the tank are small.

Based on these assumptions following equation is obtained by solving the dissolved oxygen mass balance

$$ln\left(\frac{c_{O2}-c_{O2,\infty}}{c_{O2,0}-c_{O2,\infty}}\right)=-k_L a\cdot t\,, \tag{7}$$

where $k_L a$ can be fitted against concentration profiles by means of least squares. The above-mentioned simplifications are avoided in this work by using rigorous mass transfer and stirred tank models for the analysis of experiments.

The response time of oxygen probe becomes important at intense agitation when mass transfer rates are high [VIII]. A simple first order model is used to consider probe dynamics

$$\frac{dc_{P,O2}}{dt}=\frac{1}{\tau_P}\left(c_{L,O2}-c_{P,O2}\right), \tag{8}$$

where lag time τ_P was obtained from step response measurements by moving the probe from oxygen free liquid to oxygen saturated liquid or vice versa. The time constant increased from 6.5 s in water up to 25 s in 1.0 w-% xanthan. Apparently, the thickness of the liquid film increases at the surface of membrane in viscous liquids and causes a larger mass transfer resistance. Due to long lag times, oxygen transfer measurements showed to be unreliable at higher than 0.75 w-% xanthan concentrations [VII]. Local concentration of oxygen in liquid ($c_{L,O2}$) in Eq. (8) is obtained from the stirred tank model.

3.2 Exit gas measurements

Gas phase concentrations change with both time and position in the tank during a dynamic mass transfer experiment. Instant gas solubilities and the driving force of mass transfer depend on the partial pressures of components. Gas phase dynamics has therefore a significant effect on mass transfer.

Gas phase dynamics was investigated by measuring exit gas concentrations during oxygen desorption. The concentrations were analysed with a Mass Spectrometer (MS) (Pfeiffer Vacuum Omnistar, GSD 301-O3). The MS allowed simultaneous dynamic analysis of oxygen (~32 m/e) and nitrogen (~28 m/e) intensity peaks.

The arrangement of exit gas measurements is presented in Figure 8. A part of the rising bubbles is collected to a funnel. A small fraction of the collected gas is then sampled through a three-way sampling valve and a 0.1 mm pipe. Due to narrow pipe diameter plug flow is assumed in the sampling tube. The time delay from the sampling point to MS was therefore subtracted from the measured concentration profiles. Gas funnel itself causes a time delay that is described by

$$\frac{dn_F}{dt} = A_F \sum_{i=1}^{NC} \left[U_{s,i} Y_i \right] \left(c_G - c_F \right), \tag{9}$$

where c_G is the concentration of O_2 or N_2 in gas, which rises to the funnel. Eq. (9) is solved simultaneously with the population and mass balances of stirred tank model.

The measured intensities of oxygen and nitrogen were calibrated with known calibration gas concentrations. The calibration gases were prepared by mixing synthetic air (20 % O_2, 80 % N_2, 99.99 %, AGA Finland) and pure nitrogen (99.999 %, AGA Finland). Air flow rates were measured with the mass flow controller (Bronkhorst, F200C-FDC). The combined air-nitrogen flow rate was checked with a soap bubble flow meter.

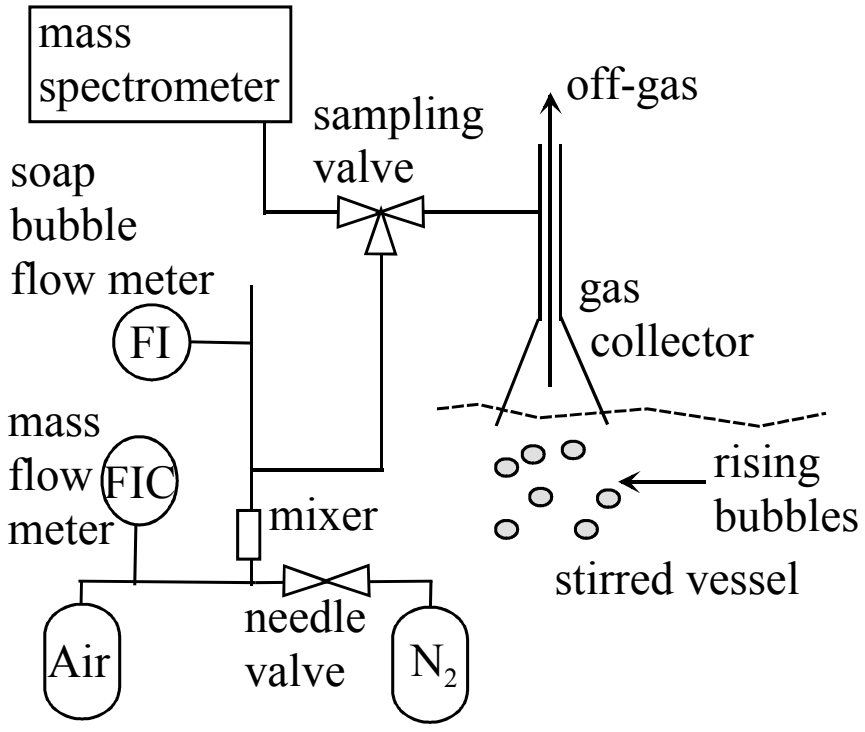

Figure 8. The arrangement of exit gas experiments.

4. MULTIBLOCK STIRRED TANK MODEL

4.1 Balance equations

Multiblock ('network-of-mixed-zones', 'compartmental') models have been applied in many studies to the investigation of local gas-liquid hydrodynamics in agitated tanks (Mann and Hackett, 1988; Vasconcelos et al. 1995; Vrábel et al. 2000; Vlaev et al. 2000; Zahradnik et al. 2001; Hristov et al. 2001; Alves et al. 2002b). Recently, Bezzo et al. (2003) and Wells and Ray, 2005) have incorporated multiblock models to commercial CFD programs.

Multiblock model is a trade-off between ideal mixing assumption and CFD. The vessel is divided into a limited number of ideally mixed subregions. Internal flow rates between subregions are obtained from either measurements or CFD simulations. Multiblock approach applies best to the cases where local conditions in the tank are of interest but small computational effort is needed.

Earlier studies have trusted mostly on the simplified modelling of mass transfer and the assumption of constant/single bubble size. Local bubble size measurements showed that assuming a constant bubble size is a crude approximation in the case of agitated tanks. Bubble size controls gas-liquid hydrodynamics and mass transfer. Modelling of local BSDs is therefore needed for the detailed analysis of gas-liquid reactors.

The developed multiblock model is based on the work of Alopaeus et al. (1999a). It includes dynamic mass, scalar and population balances for each subregion. Heat balances are not included, because the variation of temperature was small in the studied cases. A schematic illustration of multiblock model subregion is presented in Figure 9.

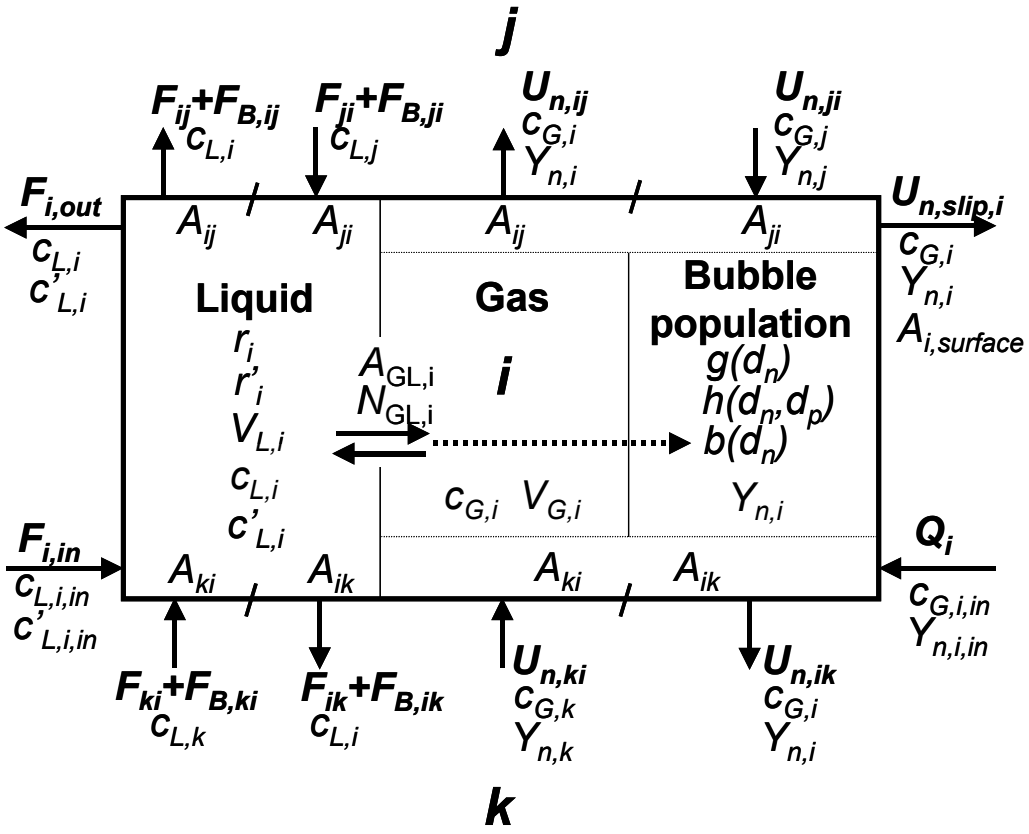

Figure 9. A schematic illustration of multiblock model subregion.

The included balance equations in each subregion (NB) are

c_G	mass balances for chemical compounds in gas phase	NC
c_L	mass balances for chemical compounds in liquid phase	NC
c'_L	scalar component balances in liquid phase	NS
Y_n	population balances for bubble size classes	NP

Overall number of balances in the multiblock model becomes then NB•(NP + NS + 2•NC).

Based on Figure 9 following mass balance is obtained for the components in gas

$$\frac{dn_{G,i}}{dt} = c_{G,i,in}Q_i - c_{G,i}A_{i,surface}\sum_{n=1}^{NP} v_n U_{n,slip,i} Y_{n,i} + \sum_{j=1}^{NB}\left[c_{G,j}A_{ji}\sum_{n=1}^{NP} v_n U_{n,ji} Y_{n,j} \right] - c_{G,i}\sum_{j=1}^{NB}\left[A_{ij}\sum_{n=1}^{NP} v_n U_{n,ij} Y_{n,i} \right] - N_{GL}A_{GL,i}V_{L,i}, \quad (10)$$

where i is the index of subregion. The indexes of chemical compounds are omitted for clarity. Terms on the right hand side are **1)** primary gas feed to the tank, **2)** rise of bubbles out of tank, **3)** internal flow in and **4)** out of subregion and **5)** gas-liquid mass transfer. Mass transfer fluxes N_{GL} are defined to be positive from gas to liquid. Bubble velocities U_{ij} at subregion interfaces are a resultant of the convective and slip velocity.

Liquid phase mass balances can be presented as

$$\frac{dn_{L,i}}{dt} = c_{L,i,in}F_{i,in} - c_{L,i}F_{i,out} + \sum_{j=1}^{NB} c_{L,j}(F_{ji} + F_{B,ji}) - c_{L,i}\sum_{j=1}^{NB}(F_{ij} + F_{B,ij}) + N_{GL}A_{GL,i}V_{L,i} + r_i V_{L,i}, \quad (11)$$

where terms on the right hand side are **1)** primary liquid feed, **2)** product outlet, **3)** internal flow in and **4)** out of subregion, **5)** gas-liquid mass transfer rate and **6)** reaction rate. Internal liquid flows include the mixing (F_{ij}) and bubble ($F_{B,ij}$) induced flow.

Scalar balances are included in the liquid phase, because components such as biomass cannot be described easily as conventional chemical species with well-defined physical properties [VII].

$$\frac{dm_{L,i}}{dt} = c'_{L,i,in}F_{i,in} - c'_{L,i}F_{i,out} + \sum_{j=1}^{NB} c'_{L,j}(F_{ji} + F_{B,ji}) - c'_{L,i}\sum_{j=1}^{NB}(F_{ij} + F_{B,ij}) + r'_i V_{L,i}, \quad (12)$$

where terms are same as in liquid mass balances with an exception that gas-liquid mass transfer term is neglected.

Population balances for bubbles are solved by using the method of classes. In this method, a set of ordinary differential equations for discrete bubble size classes is solved to obtain BSD. Accurate solution of PBs requires large number of classes. This increases the computational cost. The method of classes is however preferred due to its good stability (Marchisio et al. 2003). Another benefit of this method is that BSDs are obtained directly as the solution of PBs in contrast to other commonly used techniques such as the method of moments (Ramkrishna, 2000). This allows easier visualisation and comparison of results to the experiments. The breakage, coalescence, growth and transportation due to convection and slip are assumed to be the most important bubble phenomena in agitated tanks. A balance for a bubble size class in a subregion becomes

$$\begin{aligned}\frac{dY_{n,i}}{dt} &= \frac{1}{V_i}Q_i Y_{n,i,in} - \frac{1}{V_i}U_{slip,n,i}A_{i,surface}Y_{n,i} \\ &+ \frac{1}{V_i}\sum_{j=1}^{NB}U_{n,ji}A_{ji}Y_{n,j} - \frac{Y_{n,i}}{V_i}\sum_{j=1}^{NB}U_{n,ij}A_{ij} \\ &+ \sum_{p=n}^{NP}\beta(d_n,d_p)\Delta d_n g(d_p)Y_{p,i} + Y_{n,i}\sum_{p=1}^{\#(v_p/2)}h\left((d_n^3-d_p^3)^{1/3},d_p\right)Y_{p,i} \\ &- g(d_n)Y_{n,i} - Y_{n,i}\sum_{p=1}^{\#(v_{NP}-v_p)}h(d_n,d_p)Y_{p,i} + \frac{\Delta\left(b(d_n)Y_{n,i}\right)}{\Delta d}\end{aligned}, \tag{13}$$

where terms on the right hand side are **1)** primary gas feed, **2)** rise out of dispersion, **3)** internal flow in and **4)** out of subregion, **5)** birth of bubbles by breaking and **6)** coalescing, **7)** death by breaking and **8)** coalescing and **9)** growth due to mass transfer or varying pressure.

Besides balances (10)-(13) BSDs at gas inlet, gas and liquid flow fields and physical properties of dispersion are needed. Phenomenological closure models are needed for bubble breakage, coalescence, slip and gas-liquid mass transfer fluxes. In addition, appropriate discretization strategy with schemes for ensuring the conservation of various moments is needed to solve the PBs.

4.2 Flow field modelling

4.2.1 Liquid flows

Experimental studies have shown that liquid flow numbers F_{ij}^* are independent on the stirring speed and vessel size in turbulent flow regime (Coster and Couderc, 1988; Ranade and Joshi, 1990). Internal liquid flow rates are defined in the multiblock model according to

$$F_{ij} = F_{ij}^* \cdot N \cdot D_I^3 . \tag{14}$$

The decrease of impeller pumping capacity due to gassing is assumed to be proportional to the power consumption of mixing based on (Bakker and van den Akker, 1994; Vasconcelos et al. 1995)

$$F_{g,ij}^* = F_{u,ij}^* \frac{N_{p,g}}{N_{p,u}} \tag{15}$$

Gray (1966) has shown that this assumption should be valid for turbine impellers. The power numbers are obtained from the measured torques on impeller.

Liquid flows are assumed to be bi-directional at the interfaces between subregions. Bezzo et al. (2002) have made a similar assumption in their compartmental model. Bi-directional flows improve the accuracy of flow field prediction, if there are few subregions and especially if these subregions are not optimally arranged. The flow matrix becomes then less sparse resulting into stronger coupling between balance equations. This slightly increases the computational cost.

The rise of bubbles due to slip causes a backward liquid flow of equivalent volume as

$$F_{B,ij} = A_{ji}\sum_{n=1}^{NP}v_n U_{n,slip,ji}Y_{n,j} \tag{16}$$

The backflow of liquid ensures that relative volumes of subregions remain unchanged under gassed conditions.

4.2.2 Gas flows

Bubble velocities at subregion interfaces are calculated by summing the convective and slip velocity as

$$U_{n,ij} = \frac{F_{ij} + F_{B,ij}}{A_{ij}} + U_{n,slip,ij}\,, \tag{17}$$

where A_{ij} is the area between subregions over which liquid flows from subregion i to j. The sum of A_{ij} and A_{ji} is the physical contact area between subregions i and j (Figure 9). The implementation of Eq. (17) needs some care, because the direction of flow may depend on bubble size. Eqs. (16) and (17) induce a two-way coupling between gas and liquid flow. This coupling is not however complete, because flow field is not solved from momentum balances in the multiblock model.

4.2.3 Local dissipation rates of turbulent energy

Bubble breakage and coalescence rates, slip velocities and mass transfer fluxes depend on local dissipation rates of turbulent energy. Experimental studies have shown that turbulence energy dissipations can vary by more than two orders of magnitude in a Rushton turbine agitated tank. They are largest in the impeller swept volume constituting approximately 35 % of the total dissipation (Ranade and Joshi, 1990). Therefore dissipation rates are defined locally for each subregion.

It is assumed that all energy due to impeller motion is converted into turbulent energy, which dissipates to heat in liquid. Overall energy dissipation due to mixing is calculated from

$$\bar{\varepsilon}_{mix} = \frac{N_{p,g} D_I^5 N^3}{V_{Lt}}\,, \tag{18}$$

Local dissipation rates are related to overall dissipation by

$$\varepsilon_{mix,i} = \varphi_i \bar{\varepsilon}_{mix}\,, \tag{19}$$

where relative dissipations φ_i are scaled so that

$$\sum_{i=1}^{NB} \omega_{L,i} \varphi_i = 1\,. \tag{20}$$

$\omega_{L,i}$ is the mass fraction of liquid in a subregion of the total mass of liquid in the tank. The scaling ensures that the mass integral of local dissipation is equal to the overall power consumption (Eq. 18).

Local dissipation rates are calculated by summing turbulence energy inputs due to mixing, buyoancy and kinetic energy of gas injection

$$\varepsilon_i = \varepsilon_{mix,i} + \frac{\sum_{n=1}^{NP} Y_n \left| F_{drag,n} \right\| U_{n,slip} \right|}{\rho_{L,i}(1-\alpha_{G,i})} + \frac{Q_i \rho_{G,i} U_{sparger,i}^2}{2 V_{L,i} \rho_{L,i}}\,. \tag{21}$$

Impeller motion is a major source of energy dissipation constituting generally more than 90 % of the overall dissipation. Turbulent energy due to kinetic energy of gas injection becomes dominant in a limited area near the sparger at high gas feeds. Rising bubbles may generate up to 40 % of the local dissipation near the surface of dispersion at high gas feeds.

4.2.4 Local pressures and pressure gradients

Local bubble sizes and gas solubilities depend on the hydrostatic pressure. The variation of hydrostatic pressure can be significant in large industrial reactors. In the multiblock model, local pressures are related to the vessel-averaged density of dispersion by

$$p_i = p_{ref} + \left[\overline{\alpha_G} \cdot \overline{\rho}_G + \left(1 - \overline{\alpha}_G\right) \cdot \overline{\rho}_L\right] g \cdot L_i , \tag{22}$$

where p_{ref} is pressure at the surface of dispersion and L_i is the distance to the surface.

The dynamic and hydrostatic pressure gradients act as a driving force for bubble motion (Ranade et al. 2002). Dynamic pressure variations also cause the accumulation of gas to low-pressure regions such as behind the impeller blades (Van't Riet and Smith, 1974; Deen et al. 2002) and in the middle of upper liquid circulation loop. Dynamic pressure gradients are included in the multiblock model. They are scaled with the second power of stirring speed based on mechanical energy balance

$$\nabla p = \nabla p^* N^2 . \tag{23}$$

Test simulations with CFD indicated that scaled pressure gradients are fairly independent on stirring speed.

4.2.5 The change of flow fields

Gas and liquid flow fields, turbulence energy dissipations, pressure gradients and shear rates depend on vessel operating conditions and physical properties of dispersion and may change with time especially in batch processes. For instance, in batch xanthan fermentations physical properties of broth are initially similar to water, but fluid becomes highly viscous and shear-thinning at the end [VII]. The change of liquid flow fields due to varying liquid viscosity must be considered in the modelling of reactor, because local mass transfer and reaction conditions depend on local physical properties and gas-liquid hydrodynamics.

Internal liquid flow rates can be related to the quantity that causes the change of flow field. Simple relations such as power law seem to be sufficient for most cases

$$F_{ij}^* = F_{ij}^\circ \, exp\left(a_{ij} s + b_{ij} s^2\right), \tag{24}$$

where F°_{ij} is the flow rate in a reference case, e.g. fermentation broth without xanthan at the start of fermentation [VII]. The adjusted flow rates are constrained so that the sum of inflows is equal to the sum of outflows for each subregion ($\Sigma F^*_{ij} = \Sigma F^*_{ji}$). Parameters a_{ij} and b_{ij} are adjusted against flow fields obtained from the CFD simulations. Similar mathematical relations are adjusted to describe the changes of local dissipation rates, dynamic pressure gradients, shear rates and flow areas between subregions.

4.3 Population balance discretization

The numerical accuracy of the PB solution can be improved by using more size classes, but this causes the increase of computational cost. With appropriate discretization accurate solutions can be obtained with fewer size categories. Optimal discretization strategies are available (e.g. Litster et al. 1995), but they are often related to certain physical processes. The use of a sufficient number of classes was therefore a more practical approach. The accuracy of solution was compared to more accurate solutions with large number of size classes [VI]. Numerical tests showed that with 20 size classes arithmetic and Sauter mean diameters are overpredicted by few percents while the use of 85 classes resulted into ~0.5 % numerical error compared to accurate solution with 400 classes. Denser discretization was used for small bubbles to describe strongly skewed number BSDs accurately. It also produces more accurate solution than equal-sized discretization when the same number of classes is used. The

discretization was calculated from Eqs. (3) and (4). A typical value of discretization parameter Z was 1.05.

The discretization was made adaptive to describe the increase of bubble size during xanthan fermentation [VII]. The need for rediscretization is evaluated during the computation by monitoring the gas volume fraction in the last size class. If gas fraction in that category exceeds a predefined maximum value, the integrator is stopped and the PBs are rediscretized by using a larger maximum bubble size. Similarly, if gas fraction in the last category decreases below a predefined minimum value, rediscretization is made with a smaller maximum bubble size. New populations are then interpolated based on old populations so that bubble numbers and gas volume are conserved. The integration is continued after the rediscretization from the moment when it was stopped. The adaptive discretization not only improves the accuracy of solution but also speeds up the computation. The faster computation can be reasoned by the fact that large bubbles have large breakage rates even though their number is small. This necessitates a short integration time step. The computation becomes slow, if discretization covers a larger size range than is predicted by the PB.

Special care is needed to ensure the conservation of gas volume in breakage events, because finite number of discretization categories is used. The number of generated bubbles results from Daughter Size Distribution (DSD), but additional scaling is made to avoid small discrepancies in the conservation of gas volume. It is assumed that bubbles in the first size class do not break. The conservation of gas volume during coalescence and the generation of one coalesced bubble are ensured by dividing the resulting bubble into two nearest size classes. If coalesced bubble is larger than the maximum bubble size, it is put to the last size class by relaxing the requirement that one coalesced bubble is generated.

4.4 Numerical solution and implementation aspects

The Gill's modification of the 4^{th} order Runge-Kutta ODE-solver is used to solve the multiblock model. The solver has an adaptive time-step, which is adjusted based on the computation accuracy. The accuracy is tested by comparing the result of a single and double increment of time-step. Numerical methods for stiff ODEs were tested, but they showed no improvements in computation speed. The solution of mass transfer fluxes and bubble slip velocities introduces non-linear algebraic equations to the model. They could be solved simultaneously with ordinary differential equations as a DAE system. The Newton-Raphson iteration of mass transfer fluxes and slip velocities inside the model is preferred, because good initial guess from previous time step ensures the convergence typically within just few iteration steps.

The fitting of unknown model parameters and the simulation of long-term batch reaction dynamics can be time-consuming even with the multiblock model. A small number of subregions ensures the rapid computation, but there are some tricks that further speed up the computation. It is often possible to decrease the updating frequency of variables during the dynamic simulation. This produces significant saving in computation time. Turbulent energy dissipations, shear rates, pressure gradients, internal flow rates, reaction rates, bubble slip, breakage and coalescence rates are not updated at every time step. All values must then be saved to the workspace vector during these updates, but computation speed increases substantially without reducing the accuracy. Furthermore, it is not necessary to loop over all subregions in the summation terms of balance equations (10)-(13), but only between neighbouring subregions, which are saved to tables before the start of dynamic solution. The coalescence kernel is calculated beforehand and needs to be updated only when PBs are rediscretized. The daughter size distribution of bubble breakage can be calculated beforehand, when it is independent on local hydrodynamics and physical properties of dispersion.

Polynomial approximations are used for empirical power draw, bubble drag and bubble shape correlations around their discontinuity points. This ensures the continuity of variable and its first derivative thus improving the numerical solution.

The volumes of subregions are allowed to vary in the multiblock model. They are calculated based on material balances and molar volumes, which are related to known local mole fractions, temperature and pressure. The volumes are forced to follow material balances and phase densities so that their relative sizes remain approximately constant. This necessitates additional terms in the impeller speed independent liquid flow rates. The excess volume causes the increase of internal liquid flow rates according to

$$F_{ij}^{*} = F_{ij,0}^{*} + \frac{A_{ij}}{\sum_{j=1}^{NB} A_{ij}} \left(\frac{V_i}{V_{i,0}} - \frac{V_j}{V_{j,0}} \right) \cdot \frac{1}{\tau_{flow}}, \tag{25}$$

where τ_{flow} is a relaxation parameter, which describes the residence time of extra volume in a subregion. $V_{i,0}$ and $V_{j,0}$ refer to original subregion volumes without gassing. The relaxation parameter is needed, because momentum balances are not solved.

Gas volume fractions can be calculated from both gas phase mass balances (Eq. 10) and population balances for bubbles (Eq. 13) and they should be equal at each moment of simulation. This can be ensured only if pressure, temperature, mass transfer, reaction and other phenomena that affect the gas volume are included in the PBs. This is difficult in practice. Small discrepancies between mass and population balances are avoided in the simulations by scaling bubble populations so that their volume corresponds exactly the overall gas volume from mass balances.

The multiblock model was implemented as a collection of Fortran routines. The initial conditions, computation parameters and the multiblock model geometry together with the flow matrices are defined through namelists in the input file. The simulation can also be continued from an old state file. Dynamic and state files can be printed during the simulation as requested. Absolute and relative errors of balances are monitored during the calculation.

4.5 The created multiblock models

Multiblock models were created for the 14 and 200 L laboratory stirred tanks [V, VI, VIII] and 640 L xanthan pilot fermenter [VII]. Due to lack of experimental information flow fields were obtained from the CFD simulations. The subregions were defined as volumes and subregion interfaces were defined as planes in the CFD post-processor program for this purpose. The processing of flow matrices and turbulent dissipation rates etc. from the CFD results is time-consuming and requires matching of minor errors in mass balances. Automatic generation of subregions and internal flows (Bezzo et al. 2003; Wells and Ray, 2005) would speed up this stage but was outside the scope of this work. Subregions were selected based on the following heuristic criteria

- Subregions are arranged so that their number is minimal but still large enough to allow accurate description of gas and liquid flow fields and macroscopic spatial inhomogeneities of dispersion.
- Spatial inhomogeneity of dispersion should be minimal inside a subregion.
- Variable gradients should be nearly constant along subregion interfaces.
- The model should be applicable for varying liquid viscosities and gas feeds.

Bubble size experiments and CFD simulations indicated that 20 tangentially averaged subregions is sufficient for describing local BSDs and gas-liquid mass transfer in a Rushton turbine agitated tank. The created models for laboratory stirred tanks include 23 [V] and 21 [VI, VII] subregions. The pilot fermenter is agitated by three Rushton turbines and described by a model with 42 subregions.

Liquid flow rates, turbulent energy dissipations, pressure gradients and shear rates were evaluated from the CFD simulations [V]-[VII]. The simulations were made with the standard k-ε turbulence model and the sliding grid [V] or Multiple Reference of Frames (MRF) technique of impeller motion [VI], [VII]. This should be a reasonable approximation, because single-phase CFD predictions are fairly accurate at the moment (Middleton and Smith, 2004). For dense gas-liquid dispersions CFD predictions include substantial uncertainties but also measurement of flow fields is demanding (Ranade et al. 2001; Deen et al. 2002; Khopkar et al. 2003, 2005; Aubin et al. 2004; Lane et al. 2005; Gentric et al. 2005).

In the paper [V], liquid flow fields were estimated from single-phase CFD simulations. The investigated dispersions were lean and gas was assumed to have minor influence on liquid flow field. In the impeller region, volume was divided into two subregions, one behind and one in front of impeller blades. This allowed to describe gas accumulation behind the impeller blades.

In the paper [VI], investigated dispersions were dense and the effect of gassing on flow field was expected to be more significant. Flow fields were evaluated initially from single-phase CFD simulations. The final multiblock simulation results were calculated with the updated flow fields, which were related to gas feed rate. The change of liquid flow fields due to gassing was evaluated based on Eulerian gas-liquid CFD simulations (CFX-5.7) with the MUSIG population balance model (Lo, 2000) and the adjusted breakage and coalescence models. MUSIG is a framework in which discretized population balances are solved simultaneously with Navier-Stokes equations for Eulerian gas and liquid phases. The maximum number of bubble size classes was limited to 20 in the MUSIG model. This is barely enough for the discretization independent solution. A geometric discretization based on mass was adopted, because number BSDs are skewed strongly towards small bubble size.

The effect of gassing on liquid flow field is shown in Figure 10. The decrease of impeller pumping capacity due to gassing is proportional to the power consumption of impeller according to Eq. (15). The change of flow field is most significant near the wall in the vicinity of surface, where upward liquid flow turns earlier towards the centre of vessel at high gas feed. This agrees with some experimental observations (e.g. Khopkar et al. 2005). High flow numbers in the impeller region result mainly from the rotational flow between the subregions behind and in front of impeller blades.

A comparison to experimental studies (Revill, 1982; Coster and Couderc, 1988; Ranade and Joshi, 1990) indicated that CFD simulations underestimate impeller pumping rates. The impeller flow number was calculated from the CFD results at distance $0.05 \cdot D_I$ from the blade tip based on

$$F^*_{I,CFD} = \frac{1.1 \cdot D_I \int_{-B/2}^{+B/2} \int_0^{\pi} \alpha_L U_{L,r} \, d\theta \, dz}{N D_I^3} \tag{26}$$

The ungassed flow numbers obtained from the CFD were scaled with the measured impeller flow number 0.75 for Rushton turbines (Revill, 1982) before passing them to the multiblock model. The scaling factor becomes

$$C_{flow} = \frac{0.75}{F^*_{I,CFD}} \tag{27}$$

Similarly, the predicted mass integrals of turbulent energy dissipation rate were smaller than measured power consumptions. The deficiencies of k-ε turbulence model and the dependences on the simulation grid are apparent reasons for this. The problem was avoided by taking only the distribution of dissipation rates from the CFD. Relative dissipation rates φ_i in a subregion of multiblock model are calculated from

$$\varphi_i = \frac{\varepsilon_{CFD,i}}{\sum_{i=1}^{NB} \omega_{L,i} \varepsilon_{CFD,i}}, \tag{28}$$

where local dissipation rates are obtained from the CFD results by averaging over the subregion volumes as

$$\varepsilon_{\mathrm{CFD,i}} = \frac{\int_{V_i} \alpha_L \rho_L \varepsilon \, dV}{\int_{V_i} \alpha_L \rho_L dV}. \tag{29}$$

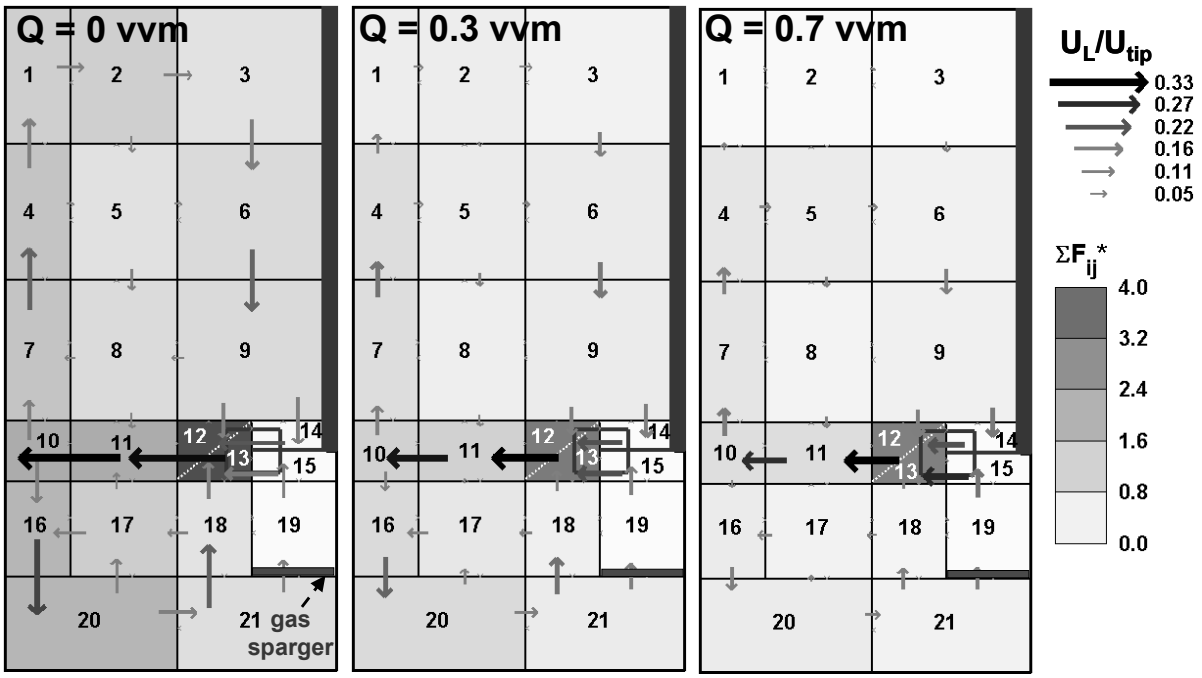

Figure 10. The effect of gassing on liquid flow field in the 200 L tank. Dimensionless velocities U_L/U_{tip} and local flow numbers (ΣF_{ij}*).

In the paper [VII], liquid flow fields were evaluated from Eulerian gas-liquid simulations at varying xanthan concentrations. The created models for air – aqueous xanthan systems in the Rushton turbine agitated laboratory tank and pilot fermenter [VII] are presented in Figure 11. Flow fields, local dissipation rates, shear rates and dynamic pressure gradients were related to xanthan concentration according to the procedure presented in the section 4.2.5 above. The adjusted flow fields showed generally smaller than 10 % relative errors compared to the CFD at varying xanthan concentrations. The resulting multiblock models (Figures 11a and 11b) predict the cavern formation, which is typical for shear-thinning aqueous xanthan solutions (Elson et al. 1986). Liquid flow rates decrease in the middle between impeller planes and near the surface of dispersion at high viscosities. At the bottom of tank, impeller discharge flow is directed towards the bottom at low xanthan concentrations but it becomes more radial at

higher than 2 w-% concentration being similar to middle and top impellers. Local dissipation rates decrease with increasing liquid viscosity in the quiescent regions of tank.

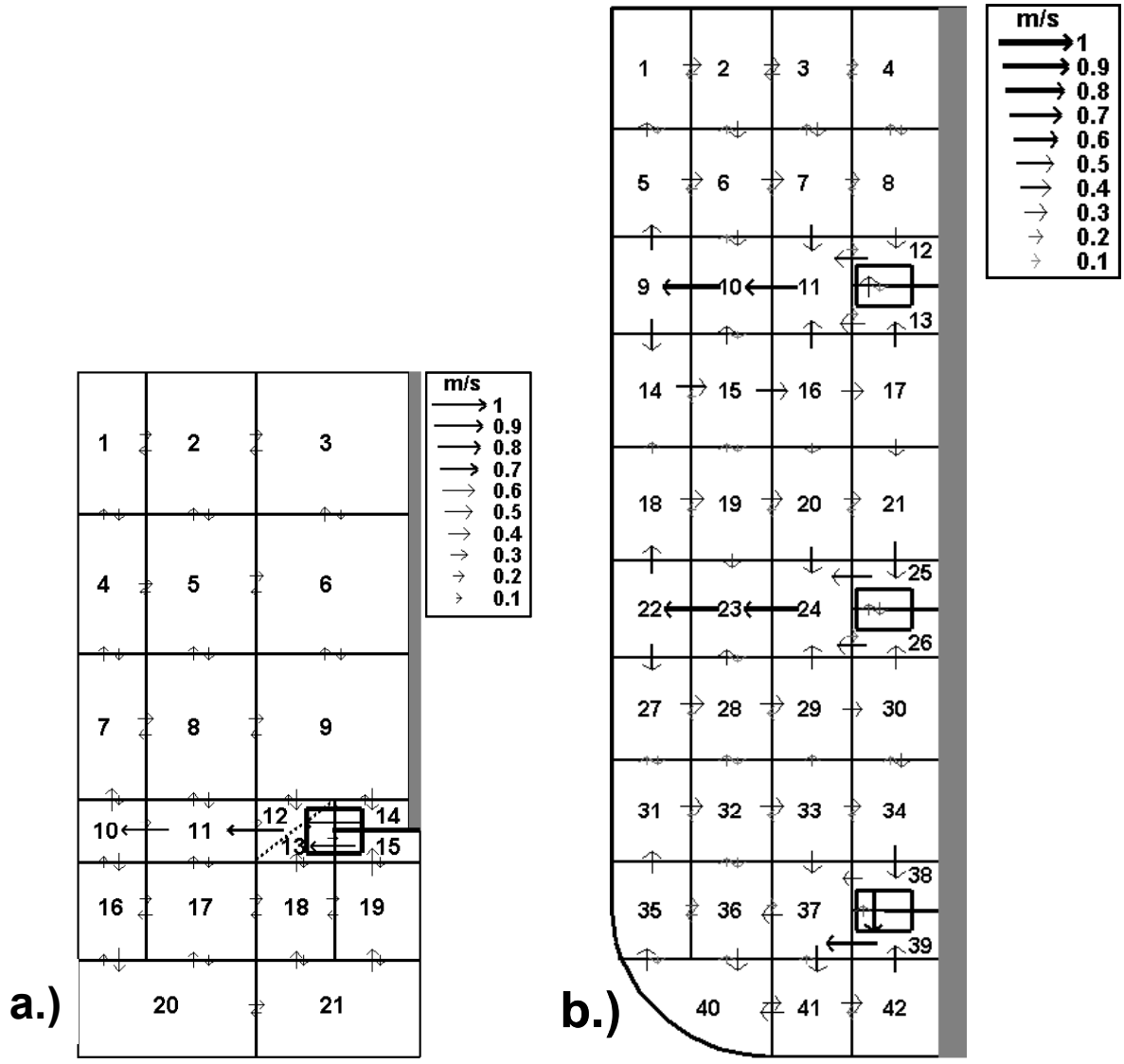

Figure 11. The division of a.) 200 L laboratory stirred tank and b.) 640 L pilot fermenter into subregions and the predicted liquid flow fields for 2 w-% xanthan.

5. CLOSURE MODELS

5.1 Bubble slip velocity

Relative velocities between bubbles and liquid (slip) are solved from the force balance on bubble by Newton-Raphson iteration

$$v_n\left(\rho_G-\rho_L\right)\left(\frac{\nabla p}{\rho_L}-g\hat{z}\right)=\frac{1}{2}a_h C_D \rho_L \overline{U}_{n,slip}\,|\,\overline{U}_{n,slip}\,| \tag{30}$$

Hydrostatic and dynamic pressure gradients are the included driving forces in Eq. (30). Other forces such as virtual mass or lift force are assumed to have minor effect and are neglected. The simulations of Khopkar et al. (2005) support this assumption. The driving forces are

balanced by the drag. The projected area of bubble a_h in the drag term is related to the definition of bubble drag coefficient and must be defined accordingly.

Bubble drag coefficients need to be determined from empirical correlations. Most correlations are valid for individual bubbles rising in stagnant liquids. Surface-active agents stabilize bubble surface resulting into larger drag coefficients and smaller slip velocities (Clift et al. 1978, Tomiyama, 1998). In addition, swarm (Ishii and Zuber, 1979) and turbulence (Poorte and Biesheuvel, 2002) effects are known to have effect on drag. The measurement of these effects is difficult due to bubble breakage and coalescence. The correlation of Ishii and Zuber (1979) predicts the increase of drag for small bubbles and the reduction of drag for large bubbles with increasing gas holdup. Test simulations with this correlation, however, showed no significant differences compared to the correlations for isolated bubbles. The reason is that swarm effects become significant only at relatively high gas holdups (>20 vol-%). The correlation of Tomiyama (1998) for isolated bubbles in slightly contaminated liquids was used for Newtonian liquids [V], [VI], [VIII].

$$C_D = \max\left\{\min\left(\frac{24}{\mathrm{Re}}\left(1+0.15\mathrm{Re}^{0.687}\right), \frac{72}{\mathrm{Re}}\right), \frac{8}{3}\frac{Eo}{Eo+4}\right\} \tag{31}$$

Many experimental (Brucato et al. 1998; Poorte and Biesheuvel, 2002) and modelling studies (Bakker and Van den Akker, 1994; Spelt and Biesheuvel, 1997; Alves et al. 2002b; Lane et al. 2005; Khopkar et al. 2005) have shown that turbulence causes the decrease of bubble slip. Brucato et al. (1998) found that the ratio of turbulent and quiescent settling velocities can be as low as 0.15 for under 0.5 mm sized particles. Poorte and Biesheuvel (2002) made experiments with active turbulence generating grids and observed that mean bubble rise velocities can reduce up to 35 % compared to quiescent conditions. The need for turbulent correction of slip has been noted also in many gas-liquid stirred tank studies (Alves et al. 2002b; Khopkar et al. 2003; Lane et al. 2005).

The exact mechanisms of turbulent dampening of slip are poorly understood. Brucato et al. (1998) developed an empirical correction for drag coefficients based on particle settling measurements. Khopkar et al. (2005) modified it for the gas-liquid stirred tanks. Lane et al. (2005) suggested that turbulent drag could be related to the ratio of bubble/particle relaxation time and integral time scale of turbulence, but did not specify the calculation procedure of these time scales. Bakker and Van den Akker (1994) proposed that increased momentum transport around the bubble could be related to the ratio of bubble size and turbulent length scale. They introduced the effective viscosity concept, which is used here with a slight modification. A modification was made to relate turbulent drag to the quantities, which are available in the multiblock model. Drag coefficients are calculated by using the effective viscosity, which is a sum of the molecular and turbulent viscosity. From the definition of kinetic energy concentration $k_e = 0.5 \cdot u'^2$, and the relation of turbulent velocity fluctuation $u' \propto \varepsilon^{1/3} \cdot d^{1/3}$ we obtain

$$\mu_{eff} = \mu_L + C_1 \rho_L \varepsilon^{1/3} d^{4/3}, \tag{32}$$

where adjustable parameter C_1 is of magnitude 0.02 (Bakker and Van den Akker, 1994). The correction predicts that bubble slip decreases with increasing turbulent energy dissipation rates. Figure 12 shows bubble slip (rise) velocities at varying values of C_1 for air bubbles in stagnant water. The parameter C_1 can be adjusted by comparing the simulated and measured gas holdup from the agitated tanks. It would be preferable to validate the correction separately based on the measured bubble rise velocities in turbulent flows (Poorte and Biesheuvel, 2002), but this was not possible in the present work.

In viscous xanthan solutions, apparent viscosity of liquid rather than turbulent viscosity controls the effective viscosity (Eq. 32). For aqueous xanthan, bubble drag coefficients were calculated from the model of Tzounakos et al. (2004) for shear-thinning fluids with a slight modification [VII], namely, that local shear rates are a sum of the liquid and bubble flow induced shear as

$$\gamma = \gamma_i^* N + \frac{U_{slip}}{d} E(d) \,. \tag{33}$$

where dimensionless liquid shear rates γ_i^* were obtained from the CFD simulations [VII]. Bubble aspect ratios were determined from the correlation of Miyahara and Yamanaka (1993).

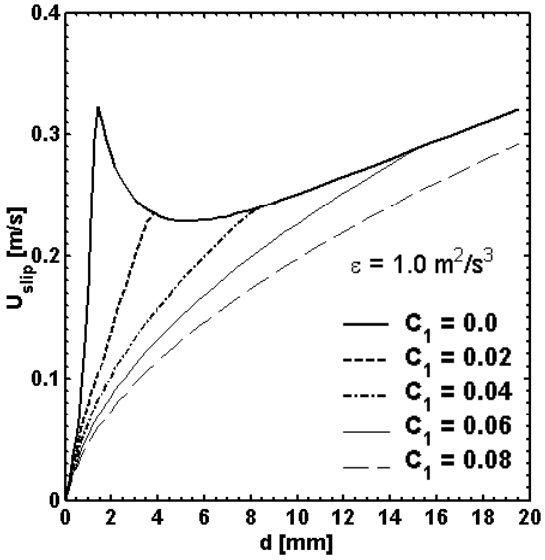

Figure 12. The effect of turbulence correction parameter C_1 on bubble slip velocity.

5.2 Bubble breakage

Bubble breakage rates depend on the balance between external stresses that disrupt the bubble and surface/viscous stresses that resist its deformation (Hinze, 1955). Turbulent deformations, viscous shear or interfacial instabilities are possible causes for the breakage (Jakobsen et al. 2005). In most studies, turbulent deformations are assumed to be the controlling mechanism of breakage. Risso and Fabre (1998) measured bubble deformation dynamics under turbulent, low-gravity conditions and observed that bubble breakage can occur suddenly as a result of large deformations or due to gradual accumulation of bubble deformation energy. Instant breakup due to large deformations was encountered more frequently in their experiments. Many experimental studies have shown that under turbulent conditions bubble breakage occurs through a dumb-bell stretching mechanism (Otake et al. 1977; Walter and Blanch, 1986; Hesketh et al. 1991a; Wilkinson et al. 1993).

The breakage can be related to the arrival of turbulent eddies on the bubble surface (Narsimhan et al. 1979; Lee et al. 1987a; Luo and Svendsen, 1996; Lehr et al. 2002; Hagesaether et al. 2002; Wang et al. 2003). Narsimhan et al. (1979) developed a model by assuming that the arrival of eddies on the surface of droplet is a Poisson process. This means that breakage events are independent on the history i.e. they occur instantly. It is assumed that only turbulent eddies smaller than the droplet diameter and with enough energy can cause breakage. Lee et al. (1987a) developed a model for bubble breakage based on the ideas of Narsimhan et al. (1979). Alopaeus et al. (2002) extended the model of Narsimhan et al. (1979) for droplets by including viscous stresses as a resisting force for breakage

$$g(d) = C_2 \varepsilon^{1/3} erfc\left(\sqrt{C_3 \frac{\sigma}{\rho_L \varepsilon^{2/3} d^{5/3}} + C_4 \frac{\mu_L}{\sqrt{\rho_L \rho_G} \varepsilon^{1/3} d^{4/3}}} \right), \tag{34}$$

where C_2, C_3 and C_4 are adjustable parameters. Eq. (34) should be applicable for gas-liquid systems, because the mechanisms of bubble and droplet breakage are very similar (Hesketh et al. 1991a). This model was tested in the papers [V] and [VI]. The dispersed phase viscosity is replaced with continuous phase viscosity in the viscous term of Eq. (34). Viscous stresses that resist the breakage are assumed to be proportional to the viscosity of liquid surrounding the bubble rather than viscosity of gas, which is small. The observations of Walter and Blanch (1986) support this assumption.

The model of Luo and Svendsen (1996) has been the basis of many modelling and simulation studies. It has been used without criticism even in recent studies (e.g. Chen et al. 2005; Dhanasekharan et al. 2005), although it has some well-known deficiencies (Hagesaether et al. 2002; Jakobsen et al. 2005; Wang et al. 2003, 2005). A significant deficiency is its dependence on the size discretization, which can be avoided by integrating the breakage rates over all breakup volume fractions and by using a separate model for the daughter size distribution. This results into following equation for overall breakage rates

$$g(d) = C_5 \cdot (1-\alpha)\left(\frac{\varepsilon}{d^2}\right)^{1/3} \int_0^1 \int_{\xi_{min}}^1 \frac{(1+\xi)^2}{\xi^{11/3}} \exp\left(- \frac{6 \cdot \sigma \left[f^{2/3} + (1-f)^{2/3} - 1 \right]}{\rho_L \varepsilon^{2/3} d^{5/3} \xi^{11/3}} \right) d\xi \, df \,, \tag{35}$$

where C_5 has a theoretical value of 0.46 (Luo and Svendsen, 1996) and ξ_{min} is the ratio of minimum eddy size and bubble size ($=\lambda_{min}/d$). The minimum eddy size is related to the Kolmogorov's microscale by $\lambda_{min} = 11.4 \cdot (\mu_L^3/\rho_L^3/\varepsilon)^{1/4}$. Eq. (35) was tested in the papers [V] and [VII].

Some deficiencies in the model of Luo and Svendsen (1996) have been avoided either by adding capillary (Lehr et al. 2002) or kinetic energy density constraints (Hagesaether et al. 2002) or both of them (Wang et al. 2003). These additional constraints lead to a minimum breakage fraction thus avoiding the evolution of infinitely small daughter bubbles. Hagesaether (1999) has noted that kinetic energy density constraint limits the breakage rate in most cases and favours the evolution of equal-sized daughter bubbles. This contradicts with some experimental observations (Hesketh et al. 1991b). A major drawback of adding kinetic energy density constraints is the increased complexity of model and, hence, high computational cost. Computation time becomes a critical issue in CFD calculations, where high number of closure model calls is needed to obtain a converged solution. It has been pointed out in many studies, that high CPU demand limits the combination of CFD and PBs at the moment. There is need for simple while still accurate breakage closures.

Kostoglou and Karabelas (2005) reviewed available bubble breakage models. They concluded that similar physical arguments used by various authors lead to quite different forms of breakage model thus resulting into great uncertainties. This is illustrated in Figure 13 were some breakage models are compared. Note the logarithmic scale! The comparison shows a significant spread thus highlighting the need of experimental validation.

Besides Eqs. (34) and (35) Daughter Size Distribution (DSD) is needed for the calculation of bubble breakage rates. Both phenomenological and purely mathematical relations are available (Wang et al. 2003). Many physical models have been suggested, but due to lack of reliable experimental information, there is no general agreement, which one is the most accurate one. Some physical models predict preferably equal-sized breakage (Martínez-Bazán et al. 1999) while some others predict non-equal sized breakage (Wang et al. 2003). The DSDs may also depend on the size of mother bubble, physical properties and turbulence

energy dissipation (Lehr et al. 2002; Wang et al. 2003), but these dependences still mostly lack the experimental validation.

Binary breakage has been a common assumption in the modelling of breakage (Wang et al. 2005; Kostoglou and Karabelas 2005). The experiments of Risso and Fabre (1998) showed that binary breakage occurs most frequently (48 % of the events), but 3-7 fragments are evolved in 37 % and even more than 10 fragments in 15 % of the events. These observations can be interpreted so that multibreakage events (more than 3 fragments) are a major source of bubbles, which are born by breakage.

Lee et al. (1987b) investigated BSDs from air – tap and air – salt water systems in airlift column and found the best agreement against experiments, when multibreakage assumption was used. This was reasoned by noting that turbulent eddies seldom provide exact minimum work required by the breakage. It was also found that DSDs have a strong influence on the steady-state BSDs.

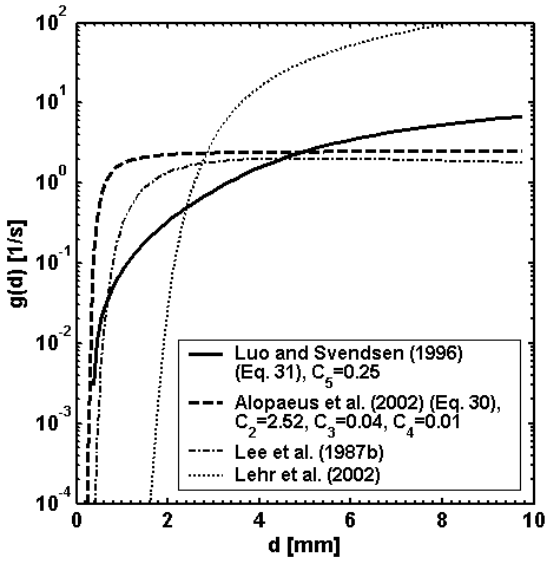

Figure 13. Predicted bubble breakage rates, $\varepsilon = 1\ m^2/s^3$, $\sigma = 0.07$ N/m, $\mu_L = 0.001$ Pa·s.

The DSD was calculated from the following mathematical expression in the papers [V], [VI], [VIII]

$$\beta\left(d_n, \mathrm{d}_p\right) = 0.5\left(1+C_6\right)\left(2+C_6\right)\left(3+C_6\right)\left(4+C_6\right)\left(\frac{d_n^2}{d_p^3}\right)\left(\frac{d_n^3}{d_p^3}\right)^2\left(1-\frac{d_n^3}{d_p^3}\right)^{C_6} . \tag{36}$$

where C_6 is an adjustable parameter. The integration of Eq. (36) from zero to the size of mother bubble results into 4/3 + C_6/3 daughter bubbles. The breakage is binary when C_6 is 2.0. The C_6–dependent scaling factor of Eq. (36) results analytically from the requirement that gas volume must conserve in a breakage event i.e.

$$\int_0^{d_p} \beta(d, d_p) d^3 dd = d_p^3 . \tag{37}$$

DSDs similar as Eq. (36) have been applied to the droplets (Hsia and Tavlarides, 1983; Alopaeus et al. 2002) and bubbles (Lee et al. 1987b). Depending on the value of adjustable parameter C_6 unequal or equal-sized breakage can be predicted. Therefore fitting can give information about DSDs. Eq. (36) predicts zero probability, when daughter bubble size approaches zero. In contrast to some more elaborated models (Hagesaether et al. 2002; Wang et al. 2003) it requires no evaluation of double or triple integrals. Eq. (36) is also independent

on the hydrodynamics and physical properties. It can be calculated beforehand and need not to be updated during the simulation. This produces substantial savings in computation times.

Lehr et al. (2002) developed a breakage model, which is still rather simple and includes no adjustable parameters. In the paper [VI], this model was tested as an alternative to Eqs. (34) and (36). According to Wang et al. (2005) both the model of Lehr et al. (2002) and the more complicated model of Wang et al. (2003) predict BSDs successfully in bubble columns. According to the Lehr's model, breakage frequencies are calculated from

$$g(d) = 0.5 \cdot \frac{d^{5/3} \rho_L^{7/5} \varepsilon^{19/15}}{\sigma^{7/5}} \exp\left(-\sqrt{2} \frac{d^3 \varepsilon^{6/5} \rho_L^{9/5}}{\sigma^{9/5}} \right). \tag{38}$$

The daughter size distribution is obtained from

$$\beta_v\left(d_n, d_p\right) = \begin{cases} \dfrac{6}{\pi^{3/2} d_n^3} \dfrac{\exp\left(-9/4 \cdot C_7 \left[\ln\left(2^{2/5} d_n \varepsilon^{2/5} (\rho_L/\sigma)^{3/5}\right)\right]^2\right)}{1 + erf\left(3/2 \cdot \ln\left[2^{1/15} d_p \varepsilon^{2/5} (\rho_L/\sigma)^{3/5}\right]\right)}, & 0 \le d_n^3 \le \dfrac{d_p^3}{2} \\ \beta_v\left(d_p - d_n, d_p\right), & \dfrac{d_p^3}{2} \le d_n^3 \le d_p^3 \end{cases}, \tag{39}$$

which assumes binary breakage. The DSD depends on turbulent energy dissipation, physical properties and the size of mother bubble. This means that it must be calculated for each location of tank and needs to be updated during the simulation.

The DSD from Eq. (39) was tested for air – aqueous xanthan in the paper [VII]. The parameter C_7 had to be included to improve the fitting against measured local BSDs. Due to same reason the assumption of binary breakage had to be relaxed.

5.3 Bubble coalescence

The coalescence is described by combining the frequency of bubble collisions and the efficiency of coalescence based on macroscopic approach (Jakobsen et al. 2005). Turbulent fluctuations are considered to be the dominant driving force for bubble collisions. The results of Prince and Blanch (1990) and Hagesaether (1999) from bubble columns support this assumption. In agitated tanks, turbulent collisions are even more dominant. The buoyant, laminar shear or wake entrainment induced collisions have been included in some studies (Prince and Blanch, 1990; Wang et al. 2005), but have been mostly neglected (Jakobsen et al. 2005).

Turbulent collisions are described most commonly based on analogy to the kinetic gas theory. Actually, this is a rough assumption, because fluid particles are neither rigid nor their collisions are elastic. A moving bubble sweeps a collision tube at turbulent velocity according to the Kolmogorov's theory. Based on these assumptions following expression can be derived for coalescence rates (Coulaloglou and Tavlarides, 1977; Prince and Blanch, 1990; Alopaeus et al. 1999)

$$h\left(d_n, d_p\right) = C_8 \cdot \varepsilon^{1/3} \left(d_n + d_p\right)^2 \left(d_n^{2/3} + d_p^{2/3}\right)^{1/2} \lambda\left(d_n, d_p\right), \tag{40}$$

where theoretical values of C_8 are in the range 0.28 - 1.11 depending on the effective collision cross-sectional area and the expression for turbulent fluctuations (Jakobsen et al. 2005).

The coalescence efficiencies $\lambda(d_n,d_p)$ are described based on a film drainage process. The coalescence occurs, if collided bubbles remain in contact for sufficient time (collision time) so that liquid film between them drains out until a critical film thickness for rupture is reached (coalescence time) (Coulaloglou and Tavlarides, 1977).

Collision times are related typically to the characteristic length scale and turbulent dissipation rate based on dimensional considerations ($t_{col} \propto r_c^{2/3}/\varepsilon^{1/3}$), because information about particle contact times is scarce (Prince and Blanch, 1990).

Coalescence times depend on the mobility of bubble surface. Different functional forms can be derived for fully or partially mobile and rigid surfaces (Chesters, 1991). In pure, low-viscosity liquids ($\mu_C \leq$ ~0.01 Pa·s) inertial forces control the film drainage. In viscous systems, coalescence times are longer due to laminar film drainage. In the mixtures, film drainage depends not only on bulk physical properties, but also on interfacial phenomena such as diffusional effects (Marangoni effect), van der Waals attractions and electrical attraction/repulsion forces (Chaudhari and Hofmann, 1994). Numerous simplifying assumptions are needed to obtain an explicit expression for the coalescence. Hagesaether (1999) analysed film drainage in detail and concluded that proper parametrization of coalescence efficiency is extremely difficult.

Several phenomenological expressions were tested for the calculation of coalescence efficiency [V]-[VII]. The model of Coulaloglou and Tavlarides (1977) is based on the film drainage between deforming droplets with immobile surfaces

$$\lambda(d_n, d_p) = exp\left(-C_9 \frac{\mu_L \rho_L \varepsilon}{\sigma^2} \left(\frac{d_n d_p}{d_n + d_p} \right)^4 \right) \tag{41}$$

The model assumes that the force compressing the droplets is proportional to the mean-square velocity difference at the ends of fluid eddy of size $d_n + d_p$. The initial and critical thicknesses of film rupture are assumed to be constant and lumped to the parameter C_9. Eq. (41) was tested in the paper [V]

Prince and Blanch (1990) developed a model based on the assumption that inertia of draining liquid and surface tension forces control the drainage of a fully mobile bubble surface

$$\lambda(d_n, d_p) = \exp\left(-C_{10} \sqrt{\frac{\rho_L \varepsilon^{2/3} d_{np}^{5/3}}{\sigma}} \right). \tag{42}$$

The initial and critical film thickness are lumped to parameter C_{10}, which is of magnitude 2.3 (Prince and Blanch, 1990). The term inside the square root is Weber number. A chance of coalescence is smaller for high-Weber-number collisions, because bubbles bounce apart before the drainage is completed. Equivalent bubble diameter d_{np} in Eq. (43) is obtained from

$$d_{np} = 2\left(\frac{1}{d_n} + \frac{1}{d_p} \right)^{-1} \tag{43}$$

The model of Prince and Blanch (1990) is identical to the model of Chesters (1991) who proposed a smaller value 0.71 for C_{10}. Eq. (42) was tested in the papers [V-VII]. Laari and Turunen (2005) adjusted the coalescence efficiency parameter C_{10} based on bubble collision and bubble size measurements from a bubble column. The resulting values of C_{10} varied from 14 in the deionized water to much larger values in liquids with surfactants.

Coalescence efficiency models similar as Eqs. (42) and (43) have been suggested in numerous works (e.g. Lee et al. 1987a; Luo 1993; Venneker et al. 2002). An interesting exception is the work of Lehr et al. (2002) who investigated bubble coalescence with a high-speed camera. They observed that only gentle collisions lead to coalescence. For air bubbles in distilled water critical approach velocity of 0.08 m/s was measured. The critical velocity was proposed to be constant and independent on physical properties in pure liquids. In liquids with additives

or in liquid mixtures critical velocity was suggested to be lower than in distilled water. The resulting model for coalescence rates is (Lehr et al. 2002)

$$h(d_n,d_p)=\frac{\pi}{4}(d_n+d_p)^2\min\left(u',0.08\frac{m}{s}\right)\exp\left(-\left(\left(\frac{\alpha_{G,\max}}{\alpha_G}\right)^{1/3}-1\right)^2\right), \tag{44}$$

where $\alpha_{G,max} = 0.6$. This model was tested in the paper [VI] together with Eqs. (38) and (39) for the breakage from the same study. The velocity difference between colliding bubbles in Eq. (44) is calculated from

$$u'=\max\left(\sqrt{2}\varepsilon^{1/3}\sqrt{d_n^{2/3}+d_p^{2/3}},\left|\overline{U}_{slip,i}-\overline{U}_{slip,j}\right|\right), \tag{45}$$

which includes the effect of both turbulent and buoyant collisions.

Coalescence efficiency models are compared in Figure 14. The models of Coulaloglou and Tavlarides (1977) and Venneker et al. (2002) predict larger efficiencies for small bubbles than other models, which show similar dependence on bubble size. The model of Coulaloglou and Tavlarides (1977) for rigid droplets predicts a much steeper decreasing trend than other models. The influence of proportionality parameter C_{10} can be evaluated by comparing the models of Prince and Blanch (1990) and Chesters (1991).

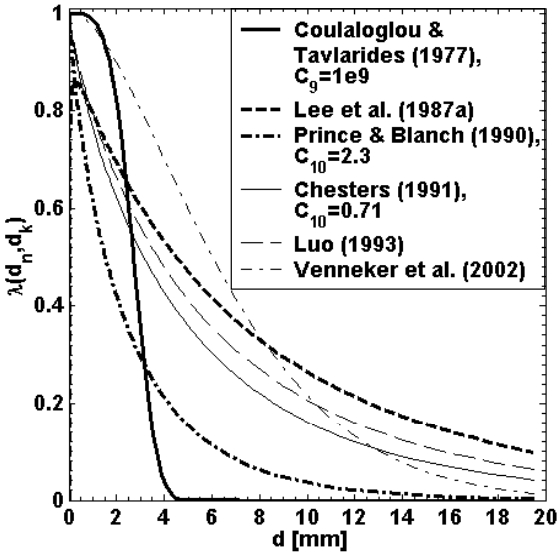

Figure 14. Predicted coalescence efficiencies for two equal-sized bubbles of diameter d, ε = 1 m^2/s^3, σ = 0.07 N/m, μ_L = 0.001 Pa·s.

5.4 Bubble growth

The growth of bubbles due to mass transfer and variation of pressure is described based on first order upwind scheme by a sink term to next larger size class and a source term from next smaller size class

$$\frac{\Delta(b(d_n)Y_{n,i})}{\Delta d}=\frac{B_{n-1,i}Y_{n-1,i}}{v_n-v_{n-1}}\bigg|_{B_{n-1,i}>0}-\frac{B_{n+1,i}Y_{n+1,i}}{v_{n+1}-v_n}\bigg|_{B_{n+1,i}<0}-\frac{B_{n,i}Y_{n,i}}{v_{n+1}-v_n}\bigg|_{B_{n,i}>0}+\frac{B_{n,i}Y_{n,i}}{v_n-v_{n-1}}\bigg|_{B_{n,i}<0}, \tag{46}$$

where volumetric growth rates are obtained from

$$B_{n,i} = -a_n \sum_{m=1}^{NC} N_{GL,m,i} \overline{V}_{G,m,i} + \sum_{j=1}^{NB} \left(1 - \frac{\overline{V}_{G,j}}{\overline{V}_{G,i}} \right) U_{n,ji} A_{ji} Y_{n,j} v_n \quad (47)$$

The first term on right hand side of Eq. (47) is growth due to gas-liquid mass transfer. The second term considers the effect of pressure variation, when bubble moves from a subregion to another. In the last size class the number of bubbles, not their diameter increases as a result of growth. Similarly, in the first size class number of bubbles decreases with decreasing bubble size.

5.5 Bubble size distributions at gas inlet

The BSD at gas inlet is a necessary input information in the stirred tank modelling. Depending on the position of sparger, primary bubbles may have influence on local BSDs everywhere in the tank. If bubbles are injected below the impeller, they typically rise directly to the impeller zone and mostly break before reaching other regions. Numerous empirical correlations are available for predicting bubble sizes at gas spargers (Kulkarni and Joshi, 2005), but information about BSDs is scarce and had to be measured [V]-[VI].

The photographing experiments with the ring sparger showed that BSDs are close to a normal distribution [VI]. The measured mean bubble diameters were in good agreement with the model of Geary and Rise (1991). The measurement of feed size distributions would have been difficult from opaque xanthan dispersions [VII]. The size distribution was assumed to follow normal distribution with the mean bubble size from the correlation of Gaddis and Vogelpohl (1986), which has been validated for a wide range of liquid viscosities and gas feeds.

5.6 Gas-liquid mass transfer

5.6.1 Mass transfer fluxes

Mass transfer fluxes are described based on the two-film theory and Maxwell-Stefan diffusion model, which assumes the conservation of momentum in molecular collisions and considers the interactions between diffusing components. Mass transfer across the gas-liquid interface is illustrated in Figure 15.

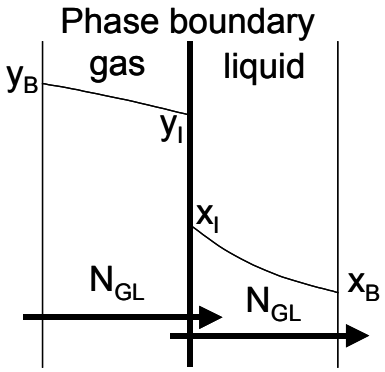

Figure 15. A schematic illustration of mass transfer process at gas-liquid interface.

The present implementation follows the linearized theory of mass transfer (Taylor and Krishna, 1993) and makes the following assumptions

- Mass transfer fluxes are at steady state at the phase boundary.
- Mass transfer resistances exist in both gas and liquid side.
- Gas and liquid concentrations are in equilibrium at the phase boundary
- No reactions occur in either gas or liquid film.

• Total concentration and diffusion coefficients are constant across the diffusion path.

Liquid side mass transfer fluxes are then obtained from

$$(N_{GL}) = c_t [k_L] \cdot [\Xi_L](x_I - x_B) + (x_I) N_{GLt} . \quad (48)$$

Similar flux equations are formulated for the gas side. The overall flux N_{GLt} and the mole fractions at the phase boundary (x_I) are solved by Newton-Raphson iteration so that fluxes in the gas and liquid side are equal and the mole fractions sum to unity in the both sides of phase boundary.

Low flux mass transfer coefficient matrices [k_L] are calculated from empirical correlations, because the film thickness required by the film theory (Lewis and Whitman, 1924) or contact time distribution required by the penetration theory (Higbie, 1935) is rarely known. The approximate formula of Alopaeus and Nordén (1999) is used to avoid time-consuming matrix multiplication and power calculations. High flux correction matrices [Ξ] are estimated based on the method of Alopaeus et al. (1999b) to further speed-up the computation.

Molar compositions and fluxes are assumed to be independent on bubble size, because breakage and coalescence smooth out concentration differences between different sized bubbles. These assumptions are necessary due to limitations of computational capacity and also get some support from the recent observations of Linek et al. (2004; 2005ab).

5.6.2 Mass transfer coefficients

Surface renewal theory is a frequently used concept for the calculation of mass transfer at gas-liquid interfaces. Liquid side mass transfer coefficients can be related to the mobility of bubble surface, which depends on bubble size and the presence of surfactants. For rigid bubbles, mass transfer coefficients approach values obtained from the equation of Frössling (1938) based on the laminar boundary layer theory. For mobile bubble surfaces mass transfer coefficients are larger by a factor ~5 approaching the penetration theory of Higbie (1935). Experimental studies have shown that mass transfer coefficients fall generally between these two extremes.

Kawase et al. (1992) derived Eq. (49) for liquid film mass transfer coefficients in power-law fluids based on the Higbie's (1935) penetration theory and the Danckwert's (1951) surface renewal theory. The model is based on the assumption that small scale turbulent eddies cause the renewal of liquid at the surface of bubble.

$$[k_L] = C_{11} [D_L]^{1/2} \left(\frac{\varepsilon \cdot \rho_L}{K} \right)^{1/(2(1+n))} , \quad (49)$$

where n = 1 and K = μ_L for Newtonian fluids. The proposed values of proportionality constant C_{11} vary from 0.301 (Kawase et al. 1992) to 0.523 (Linek et al. 2004). Linek et al. (2004) concluded that "eddy" models such as Eq. (49) describe gas-liquid mass transfer more accurately under turbulent conditions than "slip velocity" models, where contact time is related to bubble diameter (the rigidity of bubble) and the slip velocity. Garcia-Ochoa and Gomez (2004) made the sensitivity analysis and comparison of Eq. (49) with C_{11} = 0.301 to available empirical correlations for fermentation broths and found generally a good agreement. Liquid side diffusion coefficients at infinite dilution are evaluated from the correlation of Wilke and Chang (1955).

The instantaneous gas side mass transfer coefficients are estimated from the rational approximation for the transient diffusion inside a spherical fluid particle (Alopaeus, 2000)

$$\frac{[k_G]\cdot d_{32}}{[D_G]} = \frac{2}{\sqrt{\pi}}[Fo]^{-1/2} + \frac{117346\cdot[Fo]^{0.5} + 39596\cdot[Fo] + \frac{2\pi^2}{3}337258\cdot[Fo]^{1.5}}{1 + 62166\cdot[Fo]^{0.5} + 31169\cdot[Fo] + 337258\cdot[Fo]^{1.5}}, \tag{50}$$

which follows the exact solution accurately for both short and long contact times. Gas side diffusion coefficients at infinite dilution are obtained from the Chapman-Enskog theory (Poling et al. 2000). The Vignes-relation is used to convert them to finite concentrations (Taylor and Krishna, 1993). Fourier number ($Fo=D_G\cdot t_{life}/d_{32}^2$) includes bubble lifetime, which is estimated for a local bubble population from local bubble number densities Y_n and death rates by breaking and coalescing as

$$\bar{t}_{life} = \frac{1}{\sum_{n=1}^{NP} Y_n} \sum_{n=1}^{NP} \frac{Y_n}{g(d_n) + \sum_{p=1}^{\#(V_{NP}-V_p)} h(d_n, d_p) Y_p}. \tag{51}$$

5.6.3 Gas-liquid interfacial area

Local gas-liquid mass transfer areas are calculated from the BSDs. In Newtonian systems, bubbles are assumed to be oblate ellipsoids. The aspect ratio of an ellipsoid is obtained from the correlation of Wellek et al. (1966), which was actually developed for liquid-liquid dispersions. Recent measurements of Guet et al. (2005) with a four-point optical fibre probe have shown that it should be applicable to bubbles as well. In shear-thinning solutions like aqueous xanthan, small bubbles are similar to a tear-drop (Miyahara and Yamanaka 1993, [VII]) and can be approximated as prolate ellipsoids. The surface area of an oblate ellipsoid is

$$a = \frac{\pi\cdot d^2}{4}\left[2\cdot R_{ab}^{-2/3} + \frac{R_{ab}^{4/3}}{\left(1-R_{ab}^2\right)^{1/2}} ln\left(\frac{1+\left(1-R_{ab}^2\right)^{1/2}}{1-\left(1-R_{ab}^2\right)^{1/2}}\right)\right], \tag{52}$$

and the surface area of prolate ellipsoid

$$a = \frac{\pi\cdot d^2}{2}\left[R_{ab}^{2/3} + \frac{R_{ab}^{-1/3}}{\left(1-R_{ab}^2\right)^{1/2}} sin^{-1}\left[\left(1-R_{ab}^2\right)^{1/2}\right]\right], \tag{53}$$

where d is the characteristic diameter of size category and R_{ab} is the ratio of minor and major axes. The gas-liquid interfacial area per liquid volume is then obtained from

$$A_{GL,i} = \frac{V_i}{V_{L,i}} \sum_{n=1}^{NP} Y_n a_n \tag{54}$$

5.6.4 Phase equilibrium

Phase equilibrium is a limit for the mass transfer. It is needed for relating gas and liquid mole fractions at the phase boundary (Figure 15). The modelling of phase equilibrium is a rather well-established field of chemical engineering and fully predictive methods like ASOG or UNIFAC are available (Poling et al. 2000). Predictive methods are particularly useful at early stages of process development, when sufficient amount and quality of information is not available. The accuracy of predictive method is however seldom sufficient, when the process of interest is sensitive to phase equilibrium. The distillation of azeotropic mixtures is a typical example.

Chemical components do not exist as pure liquid at temperatures, which are above their critical temperature. This is typical for slightly soluble gases in agitated gas-liquid reactors.

The standard state fugacities for pure components must be defined in this case based on infinitely dilute solutions according to the Henry's law. Assuming that gas phase is ideal we have

$$x_I H(T,p) = y_I p, \tag{55}$$

where Henry's coefficients H(T,p) can be estimated from empirical correlations (e.g. Fogg and Gerrard, 1991; Hamme and Emerson, 2004). For water, Henry's coefficient can be approximated to be equal to its vapour pressure.

The gas solubilities typically decrease in aqueous solutions of organic compounds or electrolytes. This is known as 'salting-out' effect. The contributions of various components are log-additive at low concentrations according to the Sechenov's relation. In the paper [VII], the group contribution method of Weissenberger and Schumpe (1996) was applied to aqueous electrolyte solutions of xanthan.

In the cases, where all compounds are condensable at the system's temperature, pure liquid is a more convenient definition of the standard state fugacity. Such systems were investigated in the paper [I], where Vapour-Liquid Equilibrium (VLE) was investigated from binary 1-butene + alcohol mixtures with a static apparatus at constant temperature of T = 326 K. In the static measurement technique, known amounts of investigated components are injected to a thermostated cell from syringe pumps. Total pressure (p) and temperature (T) are measured. Total molar composition of binary mixture (z) is obtained from material balances. The measured pTz–data is then converted to pTxy–data by using the method of Barker (1953). Uusi-Kyyny et al. (2002) have reported the scheme for data reduction in detail. A method for the analysis of errors in the static measurement technique was presented in the paper [I].

All investigated binary systems exhibit positive deviation from the Raoult's law [I]. The isotherm of 1-butene – methanol mixture at 326 K showed azeotropic behaviour. The error analysis showed that the uncertainty of liquid density is a major error source in static VLE measurements. The parameters of Wilson, NRTL and UNIQUAC activity coefficient models were adjusted to the measured binaries. The measured VLE data and the adjusted models are useful for the design of oxygenate processes. Oxygenates are widely used fuel additives, which increase the octane number, enhance the combustion and reduce exhaust gas emissions.

6. MODEL VALIDATIONS

6.1 Power consumption of mixing

In the agitated tanks, turbulent energy originates mainly from the impeller motion. Turbulence controls bubble breakage and coalescence. It also influences bubble drag and mass transfer coefficients. Turbulent energy dissipation is therefore a key parameter in the mass transfer modelling.

Overall dissipation rates of turbulent energy were investigated by measuring impeller power consumption based on torque. The mixing motor was mounted on sensitive bearing. The torque needed to prevent the rotation of motor was measured with a strain gauge (0-100 N), which was installed in a lever arm. The strain gauge was calibrated with known weights.

As expected, power numbers N_p were independent on the impeller Reynolds number in turbulent flow regime ($Re_I > 1 \cdot 10^4$)

$$N_p = \frac{P}{\rho_L N^3 D_I^5}, \tag{56}$$

The measured power numbers for ungassed agitation are presented in Table 2. The results agree with earlier observations (Middleton, 1992). In aqueous starch and xanthan, power numbers are smaller than in Newtonian systems, because vessel was operated in transient flow regime (Re_I=20-2000). Similarly, this agrees with earlier observations (Tatterson, 1991; Khare and Niranjan, 1995; Vlaev et al. 2002). Smaller power numbers of aqueous xanthan may partly result from the presence of stagnant tiny bubbles in viscous liquids.

Table 2. Power numbers of ungassed agitation.

Liquid	Vessel [L]	Impeller	$N_{p,u}$
tap water	200	Rushton	5.6
tap water	14	Rushton	5.4
tap water	14	Flat-blade	4.5
n-butanol	14	Rushton	5.4
aq. starch, 15.6 g/L	14	Rushton	4.5
aq. xanthan, c'_X [w-%]	200	Rushton	$5.6 - 1.1 \cdot (c'_X/\text{w-\%})$

The gassed power consumption is related typically to the ungassed power consumption (Tatterson, 1991; Middleton, 1992). Cui et al. (1996) developed the following correlation for Rushton turbines

$$\frac{P_g}{P_u} = \begin{cases} 1 - 9.9\left(\dfrac{\left(Q/m^3 \cdot s^{-1}\right)\left(N/s^{-1}\right)^{0.25}}{\left(D_I/m\right)^2}\right), & \dfrac{\left(Q/m^3 \cdot s^{-1}\right)\left(N/s^{-1}\right)^{0.25}}{\left(D_I/m\right)^2} < 0.055 \\ 0.48 - 0.62\left(\dfrac{\left(Q/m^3 \cdot s^{-1}\right)\left(N/s^{-1}\right)^{0.25}}{\left(D_I/m\right)^2}\right), & \dfrac{\left(Q/m^3 \cdot s^{-1}\right)\left(N/s^{-1}\right)^{0.25}}{\left(D_I/m\right)^2} > 0.055 \end{cases} . \tag{57}$$

The parity plot of Figure 16 shows that Eq. (57) fits all measurements within reasonable accuracy, when ungassed power numbers from Table 2 are used.

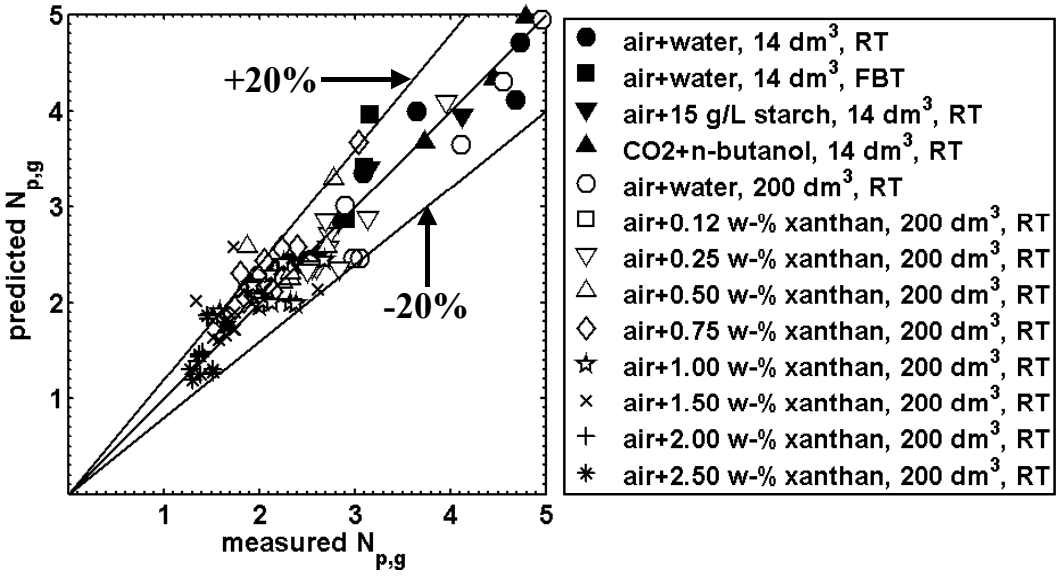

Figure 16. Measured vs. predicted (Cui et al. 1996) power numbers of gassed agitation.

6.2 Fitting of model parameters

As was pointed out in the section 5 theoretical bubble breakage, coalescence and mass transfer models include uncertain/unknown parameters and can give at best only order of magnitude estimates. The selection of appropriate phenomenological closures and the fitting of unknown/uncertain model parameters against experiments was therefore necessary for accurate BSD and gas-liquid mass transfer predictions.

Local BSDs, gas volume fractions, flow fields and mass transfer are related complicatedly to each other, microscale turbulence and physical properties of dispersion. This makes the parameter fitting a demanding task. The fitting against stirred tank experiments is motivated by the fact that creating similar turbulence conditions or investigating bubble slip, breakage and coalescence separately is difficult even in a simpler flow apparatus. By comparing simulations to the stirred tank experiments it is possible to validate the overall performance of a set of closure models. Another point of view is that parameter fitting can give valuable information for the development of new breakage and coalescence closures.

The multiblock model was used in the parameter fitting, because CFD is too time consuming for that purpose at the moment. The multiblock model considers macroscopic inhomogeneities of dispersion in the fitting. In this way, bubble breakage, coalescence, turbulent drag and mass transfer can be related to local gas-liquid hydrodynamics and physical properties of dispersion and the dependence of model parameters on vessel geometry can be avoided. The resulting models should then be more general and applicable to an arbitrary vessel size and geometry.

The multiblock model was incorporated to KINFIT parameter-fitting program (Aittamaa and Keskinen, 2005). The predicted local BSDs were compared to local measurements by means of least squares. The Levenberg-Marquardt (LM) algorithm was used to adjust unknown model parameters. The multiblock model was solved to stationary state for each experimental operating condition of tank within each LM step. The closure models were adjusted against experiments to describe arithmetic and Sauter mean diameters, number and volume BSDs. It is emphasized that all moments of BSD should be fitted accurately. This issue has been neglected in most studies by comparing number BSDs or Sauter mean diameters only. It is much easier to obtain a good fit for some specific moment of BSD than describe several or hopefully all moments of BSD accurately.

The largest weight in the fitting was set to Sauter mean diameters, because accurate prediction of mass transfer area was the main objective. The fitting was started from several sets of initial parameter values to ensure that global optimum was found. The fitting of all unknown parameters was not feasible according to the sensitivity analysis. Some insensitive and correlating parameters were fixed to decrease the parameter space. It is emphasized that fitting relies on the accuracy of experimental data. The comparison of experimental techniques showed that biasing of BSDs is possible. Heuristic evaluation of results was therefore equally important besides algorithmic approach. The correlation for liquid side mass transfer coefficients was adjusted at the final stage of fitting by comparing simulated and measured ‘oxygen concentration vs. time’ -profiles. Local mass transfer areas were obtained from the PBs with the validated bubble breakage, coalescence and turbulent slip models [V], [VII], [VIII].

6.3 The resulting parameter values

In the paper [V], bubble breakage, coalescence and mass transfer models were adjusted based on the measured BSDs from lean air – water dispersions. The fitting was extended in the paper [VI] to cover both air – water and CO_2 – n-butanol dispersions and a wider range of

vessel operating conditions. Parameter C_1 in the turbulent drag correction (Eq. 32) was adjusted by matching the simulated and measured overall gas holdups [V], [VI]. The manual adjustment of parameters was preferred in the air – aqueous xanthan case [VII], because the amount and the quality of experimental data was not sufficient to allow the use of algorithmic approach.

The adjusted parameters for different model combinations are presented in Table 3. The R-square values of Sauter mean bubble diameter d_{32} are also presented. The fitting C has the largest R-square value thus suggesting that it is the most accurate one. It is however noted that the same experimental data set was used only in the fittings A and B so that R-square values are not fully comparable. The fitting C covers a much wider range of vessel operating conditions and two chemical systems in contrast to the fittings A and B. The fitting A is slightly better than B. A detailed comparison between the simulated and measured local BSDs and mass transfer is presented below.

The adjusted parameters vary from the fitting to another (Table 3). This shows that available models are not fully predictive at the moment. The parameters seem to be correlated, because it is difficult to make experiments, which allow accurate parameter identification. The breakage and coalescence rates can be separated only, if transient or local BSDs from varying vessel-operating conditions can be included in the fitting. The present approach based on multiblock modelling is an improvement into this direction. The differences partly result from experimental uncertainties.

The adjusted collision rate parameters C_8 (Table 3) are systematically larger than theoretical values 0.28 – 1.1 (Jakobsen et al. 2005). This may indicate that kinetic gas and/or turbulent theories cannot fully describe bubble motion and their interactions. It is possible that actual diameter of collision tube is larger than $d_n + d_p$, because large bubbles are non-spherical and fluctuate even under quiescent conditions. Another reason for larger collision rates could be that collision rate and coalescence efficiency parameters are correlated. High collision rates are balanced by rather small coalescence efficiencies compared to theoretical values like C_{10}=2.3 proposed by Prince and Blanch (1990). The measurements of Laari and Turunen (2005), however, give some support to the present fittings. They adjusted coalescence efficiency parameters based on bubble persistence time and bubble column experiments and found that C_{10} should be much larger than 2.3. It is pointed out that Prince and Blanch (1990) approximated bubble collision times in their model based on purely dimensional considerations.

The adjusted models predict smaller breakage rates (fittings B and D) compared to some theoretical models (Luo and Svendsen, 1996; Lehr et al. 2002; Wang et al. 2003; Kostoglou and Karabelas, 2005). Previous validation studies are based mostly on bubble column experiments. In bubble columns, turbulence dissipations are generally much lower (< 1 W/kg) than in agitated tanks. Turbulence is the driving force of in most bubble breakage and coalescence models. This arises a question whether breakage and coalescence closures can be validated reliably against the experiments under so mild turbulence conditions. Furthermore, the estimation of turbulent energy dissipations for bubble columns is more difficult than it is for agitated tanks, where turbulence mainly originates from the impeller motion. In bubble columns, rising bubbles are a major source of turbulent energy. It is possible that a part of the hydrostatic and kinetic energy of gas may convert directly into heat in the viscous sublayer at the surface of bubble thus complicating the estimation of turbulent dissipation rates. Another important aspect related to turbulence energy dissipation is that many modelling studies have been made with CFD. The CFD often underestimates dissipations by 20-50 % unless extremely fine grids are used. In the present work, this was avoided by scaling local

dissipations so that their mass integral corresponds the measured power consumption of impeller.

In the case of air – aqueous xanthan (fitting D), the breakage rate parameter $C_5 = 0.14$ is smaller than $C_5 = 0.46$ suggested by Luo and Svendsen (1996). The lower value may partly result from the fact that viscous stresses are not included as a resisting force of bubble deformation in the breakage model Eq. (35).

Table 3. The adjusted parameters. #95 % confidence limit. *fixed at the final stage of fitting.

Fitting		Closure models	Parameter values	$R^2(d_{32})$
A	**Paper [V]** Air – water Q = 0.018 – 0.1 vvm $\bar{\varepsilon}_{mix}$= 0.2 – 0.8 W/kg	Breakage (Eqs. 34, 36) Coalescence (Eqs. 40, 41) Turbulent drag (Eq. 32) Mass transfer (Eq. 49)	C_2=6.0 ± 1.1#; C_3=0.04*; C_4=0.01*; C_6 = 4.3±0.9# C_8=4.6 ± 0.4#; C_9=6.0·10^9* C_1=0.2* C_{11}=0.54	0.49
B	**Paper [V]** Air – water Q = 0.018 – 0.1 vvm $\bar{\varepsilon}_{mix}$= 0.2 – 0.8 W/kg	Breakage (Eqs. 35, 36) Coalescence (Eqs. 40, 42) Turbulent drag (Eq. 32) Mass transfer (Eq. 49)	C_5=0.25±0.06#; C_6=12.4±3.4# C_8=3.5±0.3#; C_{10}=4.0* C_1=0.2 C_{11}=0.50	0.43
C	**Papers [VI], [VIII]** Air – water & CO_2 – n-butanol Q = 0.1 – 0.9 vvm $\bar{\varepsilon}_{mix}$= 0.1 – 3 W/kg	Breakage (Eqs. 34, 36) Coalescence (Eqs. 40, 42) Turbulent drag (Eq. 32) Mass transfer (Eq. 49)	C_2=2.52; C_3=0.04*; C_4=0.01*; C_6 = 18.25 C_8=2.65; C_{10}= 5.17 C_1=0.06 C_{11}=0.46	0.80
D	**Paper [VII]** Air – aq. xanthan Q = 0.1 – 0.9 vvm $\bar{\varepsilon}$ = 0.1 – 3.0 W/kg	Breakage (Eqs. 34, 39) Coalescence (Eqs. 40, 42) Mass transfer (Eq. 49)	C_5=0.14, C_7=0.3 C_8=0.88; C_{10}=0.6$\sqrt{0.5}$ ≈ 0.42 C_{11}=0.3	0.45

The adjusted daughter size distributions predict that unequal-sized breakage into more than two fragments is favoured. This shows some agreement to the measurements of Risso and Fabre (1998) and is interesting in a view that binary breakage has been a common assumption in the modelling (Kostoglou and Karabelas, 2005). Similarly, in the case of air – aqueous xanthan, unequal-sized breakage showed to be a necessary assumption and was obtained by setting $\beta(d_p\text{-}d_n,d_p) = \beta(d_n,d_p)$ for $d_n^3 \geq d_p^3/2$ in Eq. (39). It is noted that breakage, coalescence, slip are related complicatedly to each other in agitated tanks. Unfortunately this means that deficiencies in one model may be compensated by the adjusted parameters in some others.

The adjusted turbulent drag parameter C_1 was 0.2 in the fittings A and B while notably smaller value 0.06 was obtained for dense dispersions in the fitting C (Table 3). A reason for the difference is that fitting of C_1 partly compensates the uncertainties of flow field and BSD predictions. Therefore turbulent drag correction should be validated preferably based on isolated experiments (Poorte and Biesheuvel, 2002). It is emphasized that the fitting of C_1 was necessary, because neglecting it would have roughly halved simulated overall gas holdup compared to the measurements. The overall gas holdup must be predicted accurately, because local gas holdups and BSDs are related complicatedly to each other through bubble slip, coalescence rates and turbulence. Significant under-prediction of gas holdup would result into inaccurate bubble coalescence and mass transfer rate predictions.

The adjusted bubble breakage, coalescence and turbulent slip closures (Table 3) were used to estimate local gas-liquid interfacial areas available for mass transfer [V], [VII], [VIII]. Mass transfer fluxes were solved from the rigorous model presented in the section 5.6. The simulated and measured local dissolved oxygen concentration profiles were compared by

means of least squares to adjust parameter C_{11} in the correlation for liquid side mass transfer coefficients (Eq. 49).

In the paper [V] oxygen transfer rates were measured from lean air – water dispersions. The dynamics of oxygen probe was assumed to have minor importance, because mass transfer rates were low. In the paper [VIII], oxygen transfer was investigated at more intense agitation conditions and probe dynamics was incorporated to the analysis of results. The model for the oxygen probe (Eq. 8) was solved simultaneously with the multiblock model balances. The simulated 'DO vs. time'-profiles of oxygen probe were compared to oxygen transfer measurements.

The adjusted values of C_{11} from the fittings A and B (Table 3) are slightly larger compared to the fitting C. It seems that the fitting of C_{11} compensates the differences in the predicted gas-liquid interfacial areas. The resulting values of C_{11} for air – water system agree closely with the value 0.523 proposed by Linek et al. (2004). This gives further confidence to the present results. For the aqueous xanthan the value of C_{11}=0.3 (fitting D) is the same as Kawase et al. (1992) suggested for gassed bioreactors. Similarly, Garcia-Ochoa and Gomes (2004) have found that this model agrees with empirical $k_L a$-correlations for actual fermentation broths.

6.4 Predicted vs. measured local bubble size distributions

6.4.1 Air – water / CO_2 – n-butanol

Figure 17 presents the parity plots of local arithmetic (d_{10}) and Sauter (d_{32}) mean bubble diameters in the fitting case C (Table 3). Sauter mean diameters have smaller deviation because their weight was larger in the fitting. The model describes measured mean bubble diameters fairly well in a view that it covers a wide range of agitation conditions, two chemical systems and fits both number and volume BSDs.

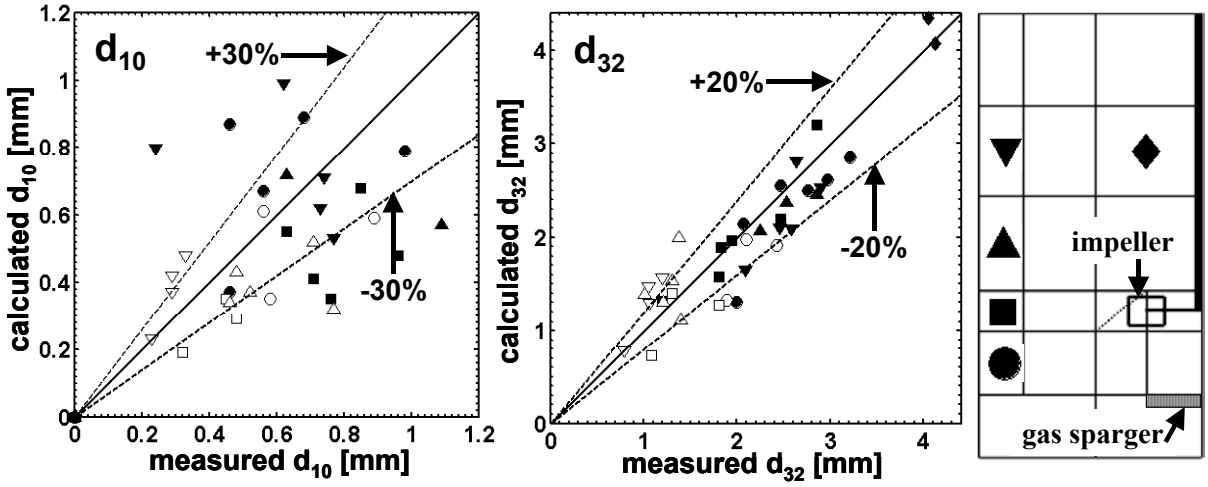

Figure 17. The calculated (fitting C) vs. measured, local arithmethic d_{10} (left) and Sauter mean bubble diameters d_{32} (right), air – tap water (closed markers) CO_2 – n-butanol (open markers).

The simulated (fitting C, Table 3) gas volume fractions are compared to the measurements from air – tap water in the 200 L tank in Figure 18. Gas holdups were measured based on the change of dispersion level inside a submerged tube, which minimised the measurement uncertainty due to fluctuating surface. The following empirical correlation of Calderbank (1958) is included to the comparison

$$\bar{\alpha}_G = \left(\frac{U_s \bar{\alpha}_G}{U_t} \right)^{0.5} + 0.000216 \cdot \bar{\varepsilon}^{0.4} \left(\frac{\rho_L}{\sigma} \right)^{0.6} \left(\frac{U_s}{U_t} \right)^{0.5}, \quad (58)$$

where all values are in SI units and U_t is 0.265 m/s. The measurements, multiblock and CFD simulations are in good agreement. The correlation of Calderbank (1958) predicts somewhat smaller gas holdup at high mixing intensities. It is emphasized that the turbulence correction of slip was necessary in all modelling approaches for ensuring reasonable gas holdup predictions. Even the ideal mixing assumption predicts gas holdup in a satisfactory manner. This indicates that overall gas holdup mostly depends on the sizes and velocities of bubbles rising out tank.

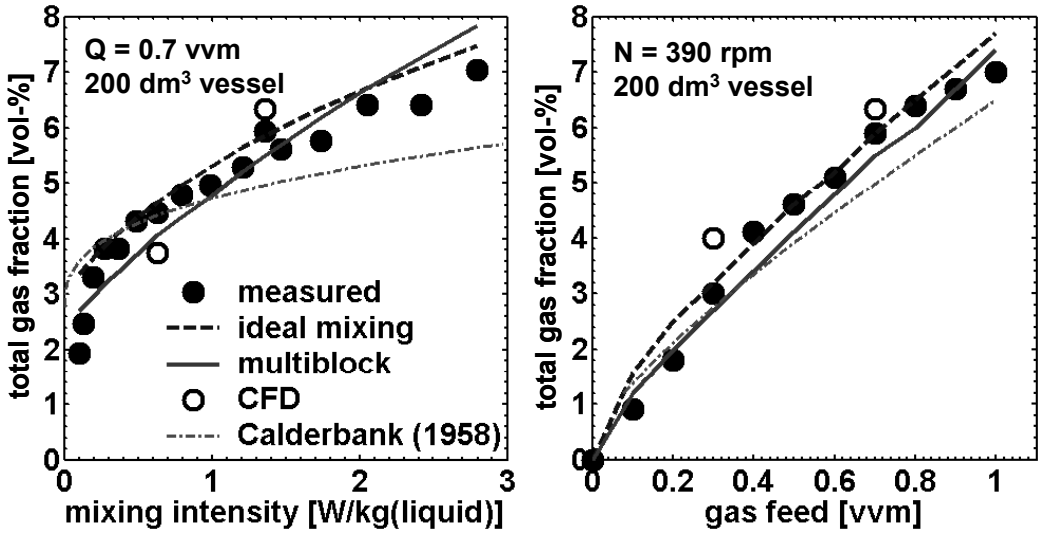

Figure 18. The simulated and measured gas volume fractions [vol-%], air – tap water, 200 L tank.

An example of local gas volume fractions predicted by the multiblock and CFD model (fitting C) in 'air–tap water'-case is presented in Figure 19. The averaged CFD results for subregions are compared to the multiblock simulations. Both modelling approaches predict the largest gas holdup above the sparger. Gas accumulates to the regions near the wall below the impeller plane where liquid flows downwards and to the centre of upper liquid circulation loop. The smallest gas holdups are found below the impeller plane in the middle, and close to the bottom of tank. In the impeller discharge flow, gas holdup decreases towards the wall. The simulated trends agree with the measurements of Barigou and Greaves (1996) from a Rushton turbine agitated tank with a conductivity probe technique.

It is interesting that the multiblock and CFD models predict a very similar distribution of gas, while the computational cost of CFD is more than 1000-fold. There are also some differences. The multiblock simulations predict larger gas holdup near the wall in the vicinity of surface and near the gas sparger than CFD. CFD simulations agree better with the visual observations, namely, that rising bubbles move towards the centre of vessel. Above the impeller and below the gas sparger multiblock model predicts lower gas holdup than CFD. In the CFD model gas sparger located closer to the bottom of tank. In the multiblock simulations it showed to be more realistic to feed the gas to the upper subregion. This is justified by the low number of subregions and the observation that most of gas rises directly to the impeller.

The fittings A and B are compared to the experiments in Figure 20 where local volume BSDs are presented. The agreement is good elsewhere but near the wall below the impeller. Liquid

flow field rather than bubble breakage, coalescence or slip model is an apparent cause for the difference in this region. It is emphasized that the multiblock model assumes a stationary flow field. This actually contradicts with the inherently transient nature of turbulent flow. The simulations describe successfully the presence of small bubbles in the impeller region and the increase of bubble sizes in the quiescent regions of tank and with increasing gas feed.

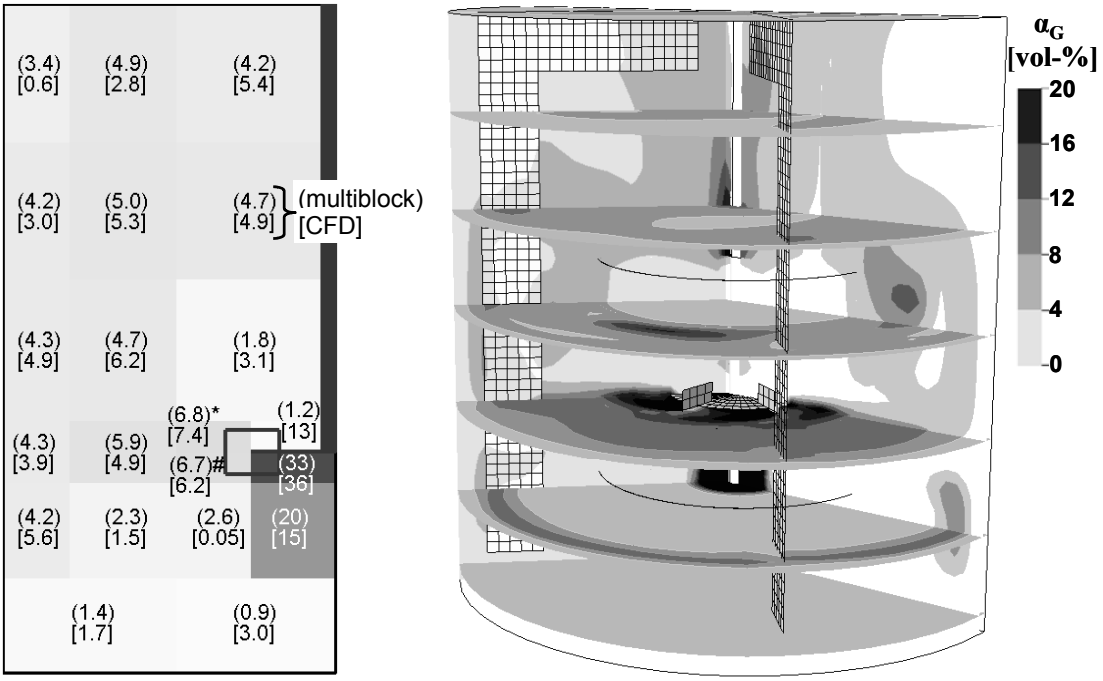

Figure 19. Predicted local gas holdups [vol-%], air – tap water, N = 300 rpm, Q = 0.7 vvm, 200 L tank (multiblock simulation left, CFD right). Numerical values: multiblock simulation in (parentheses) and CFD in [brackets], *behind, #in front of impeller blades.

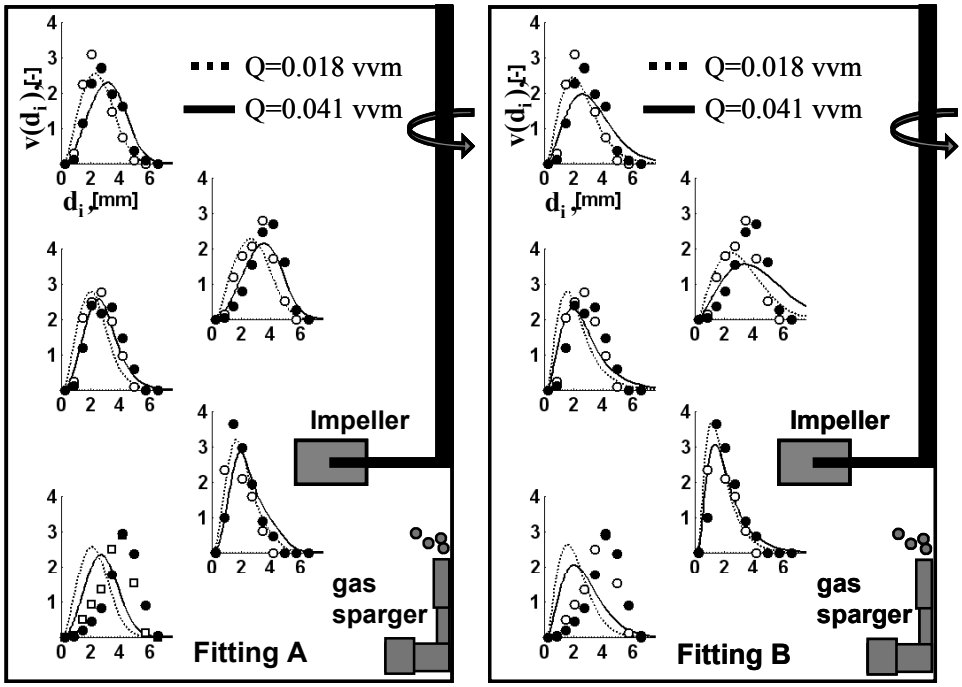

Figure 20. Simulated (lines) and measured (markers) volumetric BSDs, air – tap water, 200 dm^3 vessel, N = 220 rpm.

The simulated local BSDs with the fitting C are compared to the measured volume BSDs in Figure 21. Multiblock simulations with the closure models of Lehr et al. (2002) are included to the comparison (Eqs. 38, 39 for breakage with C_7=1.0 and Eq. (44) for the coalescence). The Lehr's model has been successful in bubble column studies (Wang et al. 2005) and it is interesting to evaluate its applicability for the gas-liquid agitation. The turbulence correction of slip was included in these simulations with slightly smaller value of correction parameter C_1=0.038 to produce reasonable gas holdup predictions compared to the present measurements.

The comparison in Figure 21 shows that the Lehr's model predicts smaller bubble sizes compared to the present measurements elsewhere but in the location E. The fitting C shows better agreement as expected. This shows that care is needed, when breakage and coalescence closures are applied to a new flow environment. In the location E, the fitting predicts a larger size range of bubbles compared to the capillary measurement. The size range of existing bubbles may however be wider than the measurements indicates, because only 1.2 – 6 mm bubbles were detected with a 1.2 mm capillary.

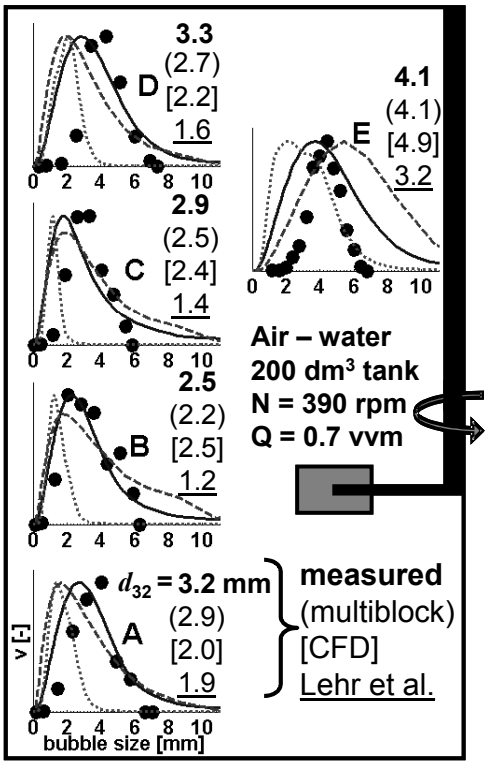

Figure 21. Local volume BSDs. ● Photography (A-D) and capillary (E) measurements, ——— multiblock and – – – CFD simulations (fitting C), ····· multiblock prediction with the model of Lehr et al. 2002), Sauter mean diameters d_{32} [mm]: measured **bold**, multiblock (parentheses), CFD [brackets], Lehr et al. (2002) underlined.

The adjusted model predicts larger tails in the BSDs near the wall compared to the photographing measurements. One reason is that some bubbles pass the impeller without breaking. The measured BSD from location B is bimodal and indicates similarly that all bubbles may not break in the impeller region. Large bubbles may also originate from gas vortices behind the impeller blades. It is noted that up to 10 mm bubbles were found, when large number of photographs was checked. The analysis of 600-1000 bubbles for one BSD is not statistically significant for large bubbles, because the majority of bubbles is extremely small. A 10 mm bubble can have a significant effect on volume BSD. It is therefore possible that these tails existed but were not observed. Another issue related to the measurement

accuracy is that due to dense dispersion camera lens had to be focused to the tank wall. The amount of large bubbles may be smaller near the wall due to wall effects. The CFD simulations predict larger tails in the volume BSDs than multiblock model. In the CFD simulations it was possible to use only 20 bubble size classes. Numerical tests showed that with 20 classes mean bubble size is over-predicted few percents when compared to the accurate solution with 400 classes.

In Figure 22 multiblock and CFD predictions (fitting C) are compared to the measured local Sauter mean diameters from air – tap water dispersion in the 200 L tank. The trends from the multiblock and CFD simulations are similar. The largest bubbles are found above the gas sparger. Bubbles rise from the sparger to the impeller. In the impeller region gas holdup is relatively high. As a consequence, bubble size decreases due to breakage not until in the impeller discharge flow. The smallest bubbles are found below the impeller near the bottom of tank. Above the impeller bubble size increases from the wall towards impeller shaft. This agrees with the capillary measurement in the point E. Near the impeller shaft and near the wall below the impeller bubbles are trapped by the downward liquid flow. This generates high local gas holdups that favour coalescence.

The simulated trends of spatial bubble size variation in Figure 22 agree with the observations of Barigou and Greaves (1992), who investigated local BSDs in a Rushton turbine agitated vessel with capillary suction probe. Sauter mean bubble diameters varied in their experiments in the range 3 – 4.5 mm above the impeller, but actual variation may have been larger due to limitations of capillary technique. In the impeller discharge flow Barigou and Greaves (1992) observed smaller bubbles compared to the predictions in Figure 22. It is noted that the sampling of large bubbles into capillary is more difficult in that region than in quiescent regions, because bubbles break more easily at the nose of capillary in intense, transverse liquid flow.

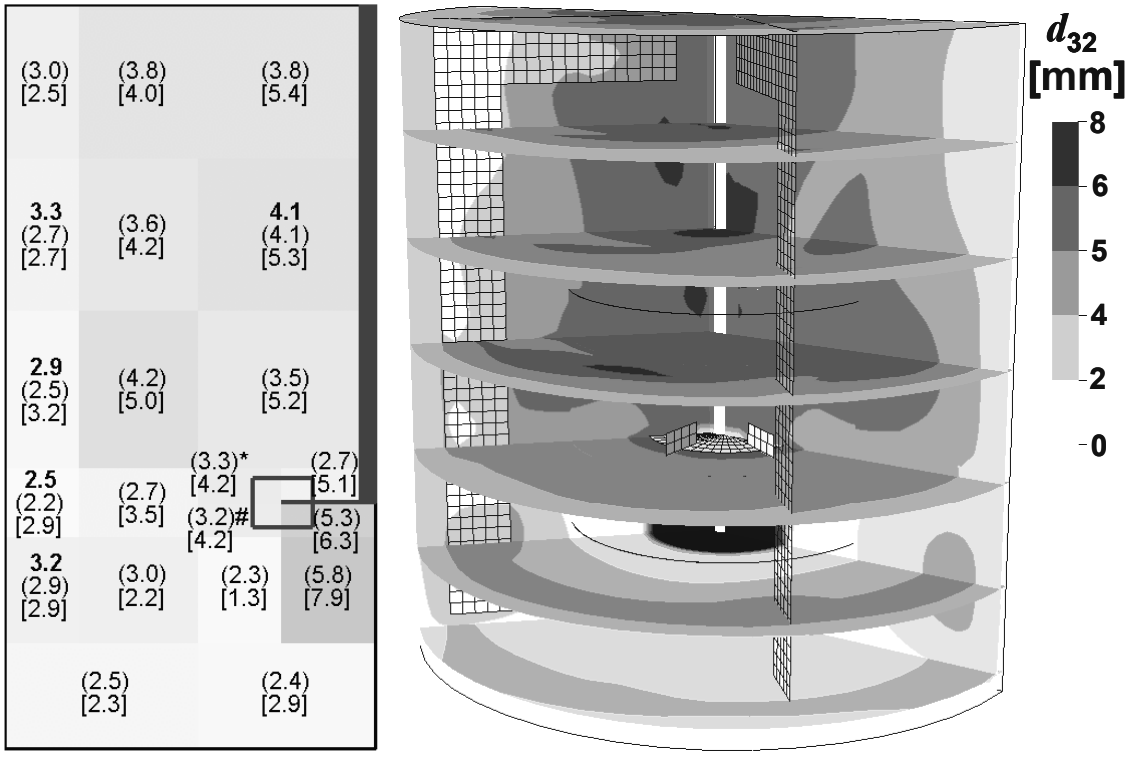

Figure 22. Local Sauter mean diameters d_{32} (fitting C), air – tap water, N = 390 rpm, Q = 0.7 vvm, 200 L tank. (multiblock simulation left, CFD right), Numbers in millimeters: measured **bold**, multiblock (parentheses), CFD [brackets], *behind, #in front of impeller blade.

CFD simulations in Figure 22 predict that bubble size first increases and then decreases near the wall from the impeller plane towards the surface. This disagrees with the multiblock simulations and experiments. It is noted that in the MUSIG model (CFX-5.7) different sized bubbles have a common velocity field while in the multiblock model slip velocities are solved for each size class.

The fitting C is compared to the measurements from CO_2 – n-butanol dispersion in the 14 L vessel in Figure 23. The volume BSD at gas inlet is included to show that breakage and coalescence control local BSDs in the tank.

The adjusted model predicts the skewed shape of number BSDs successfully. A majority of gas volume is in large bubbles, which produces more symmetrical volume BSDs. The measurements and simulations of air – water system showed a similar trend [VI]. The measurements of Takahashi and Nienow (1992) and Machon et al. (1997) from the agitated tanks have shown similarly that number probability density has a pronounced peak of extremely small bubbles with a long tail of few large bubbles.

The tails in the predicted volume BSDs are larger than the measurements indicate. Similarly as in the case of 200 L tank there are secondary peaks in the experimental volume BSDs. This indicates that all bubbles do not break when they pass the impeller region. The simulations indicate that there is a fraction of 8 mm primary bubbles. It is possible that these large bubbles were not observed due to limitations of measurement technique. Other possible causes are the deficiencies of closure models, flow field or primary bubble size estimation. The Lehr's model predicts again narrow BSDs with too few small and large bubbles compared to the present measurements.

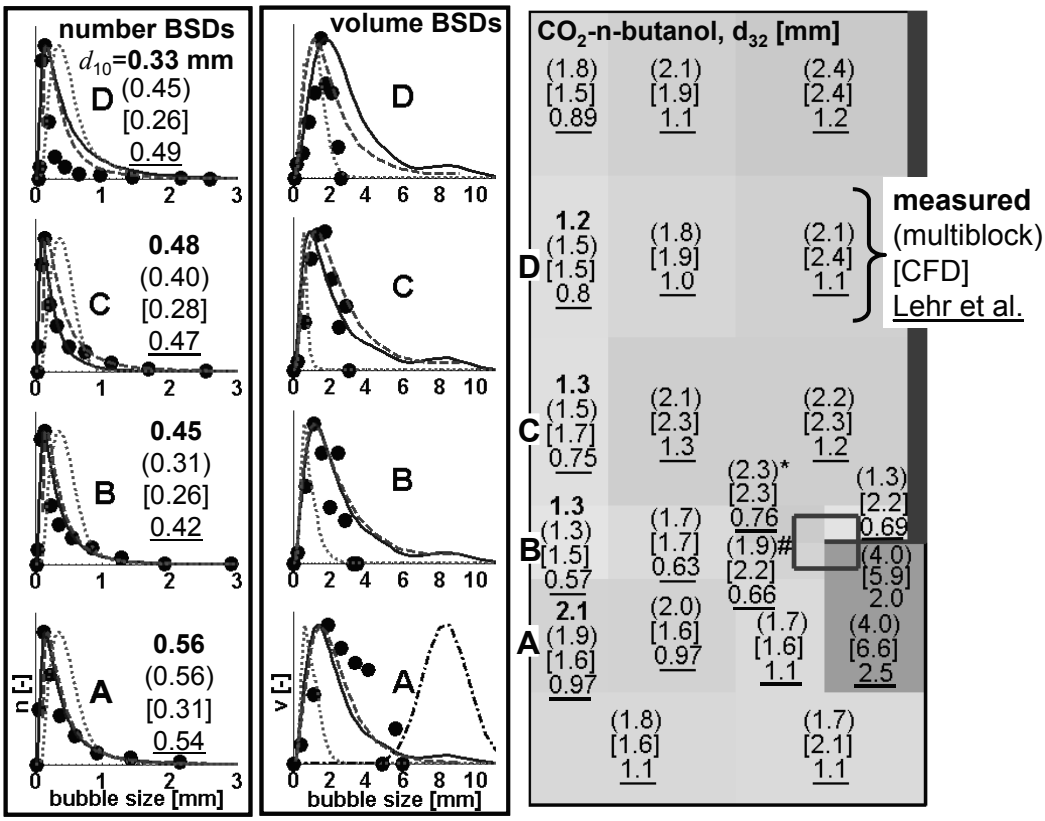

Figure 23. Local BSDs, CO_2 – n-butanol, 14 L tank, N = 700 rpm, Q = 0.7 vvm. ● Measured, ——— multiblock and – – – CFD (Fitting C), ····· multiblock (Lehr et al. 2002), —·— feed size distribution, Mean diameters [mm]: measured **bold**, multiblock (parentheses), CFD [brackets], Lehr et al. (2002) underlined. *behind and #in front of impeller blade.

The predicted spatial inhomogeneities of BSDs are similar in the 14 and 200 L tank (Figure 22). The multiblock simulations show that bubble size increases from the impeller plane (location B) towards the surface in both investigated systems while CFD predicts a maximum in the location C. The multiblock simulations agree better with the measurements from air – water dispersion than CFD simulations. In the case of CO_2 – n-butanol system, CFD shows better agreement to the measurements.

The comparisons show that adjusted breakage, coalescence and turbulent slip closures predict the general trends of local gas-liquid hydrodynamics successfully, although there remains room for improvements. Most importantly, the results demonstrate the potential of population balances for the detailed description of local gas-liquid hydrodynamics and interfacial areas available for mass transfer. Due to complexity of turbulent gas-liquid flow and several superimposed phenomena it seems that the fitting against local measured BSDs alone is not sufficient for the validation of bubble breakage and coalescence mechanisms. The fitting still improves the accuracy of predictions as the comparison to the model of Lehr et al (2002) shows [VI]. It can be concluded that phenomenological breakage and coalescence closures are not fully predictive at the moment and need experimental validation for varying chemical systems and flow environments.

6.4.2 Air – aqueous xanthan

The multiblock simulations with the adjusted PB closure models for aqueous xanthan systems (fitting D, Table 3) are compared to the experiments in Figure 24. The model describes qualitatively the dependence of BSDs on xanthan concentration and hence the liquid viscosity. The predicted cumulative volume BSDs agree with the measurements from 0.13 and 0.25 w-% xanthan dispersions, but larger deviation can be found in the case of 0.5 w-% solution. It is noted that reliable measurement of BSDs from viscous dispersions (>0.5 w-%) was demanding due to wide range of bubble sizes (0.1 – 100 mm). The model predicts the increasing fraction of stagnant bubbles from approximately 20 % in the 0.5 w-% solution up to 50 % in the 2.5 w-% solution. This agrees with the observations that tiny bubbles gradually accumulated to high viscosity solutions.

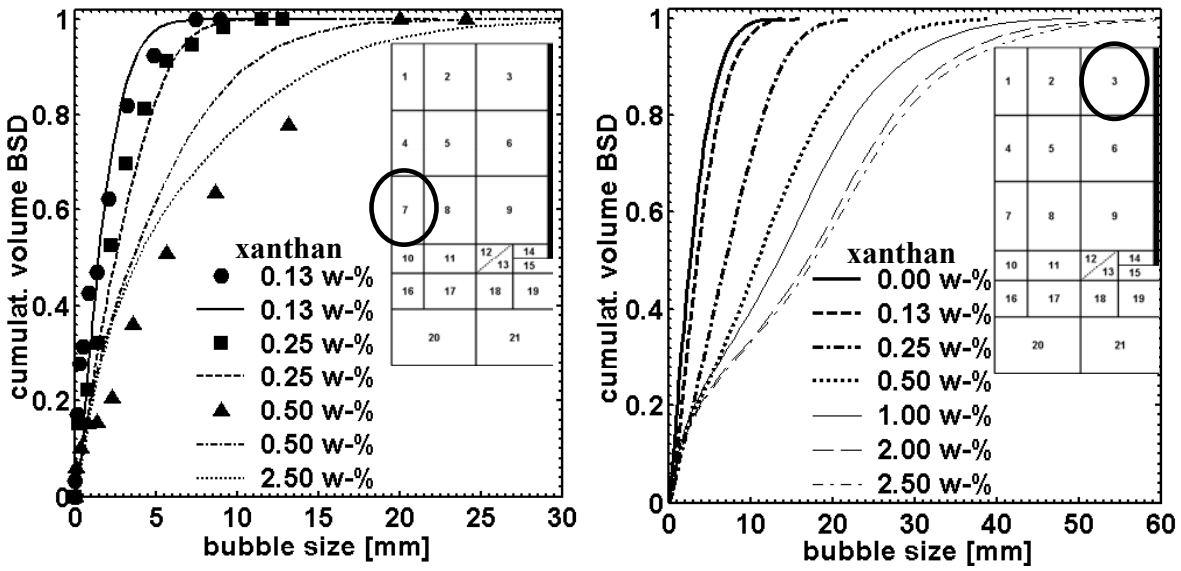

Figure 24. Simulated (lines, fitting D) vs. measured (markers) cumulative volume BSDs at varying xanthan concentrations near the wall (left) and near the surface (right) in the 200 L tank, N = 390 rpm, Q = 0.5 vvm.

The predicted BSDs near the impeller shaft close to the surface of dispersion are shown on the right hand side of Figure 24. The simulations predict the existence of up to 60 mm bubbles at high xanthan concentrations. This agrees with the observation that large gas slugs raised out from viscous xanthan solutions. The simulations predict that rising bubbles stop at the edge of nearly stagnant, viscous liquid layer and start to coalescence until the buoyancy becomes so large that gas slugs can pass through it. Visual observations confirmed this behaviour.

The simulated overall gas holdups are compared to the measurements in Figure 25. Actually, gas volume holdup showed to be time-dependent at high xanthan concentrations. This obviously results from the slow accumulation of tiny bubbles. The measured gas holdups were mostly dynamic including the gas that rises out within few minutes after the agitation and gassing have been stopped. The foaming and the fluctuations due to bursting gas slugs disturbed heavily the detection of dispersion height at high xanthan concentrations. Overall, the agreement is satisfactory although scatter in the measurements is large. Contrary to the experiments the model predicts a slight increase of gas holdup also at high gas feed rates. The difference is accepted, because simulated gas holdups include small stagnant bubbles, which were not considered in dynamic gas holdup measurements.

The xanthan simulations studies show that the multiblock stirred tank model with the adjusted breakage and coalescence models captures the main features of complex gas-liquid hydrodynamics successfully. The population balances for bubbles are a significant improvement in the modelling of viscous gas-liquid agitation.

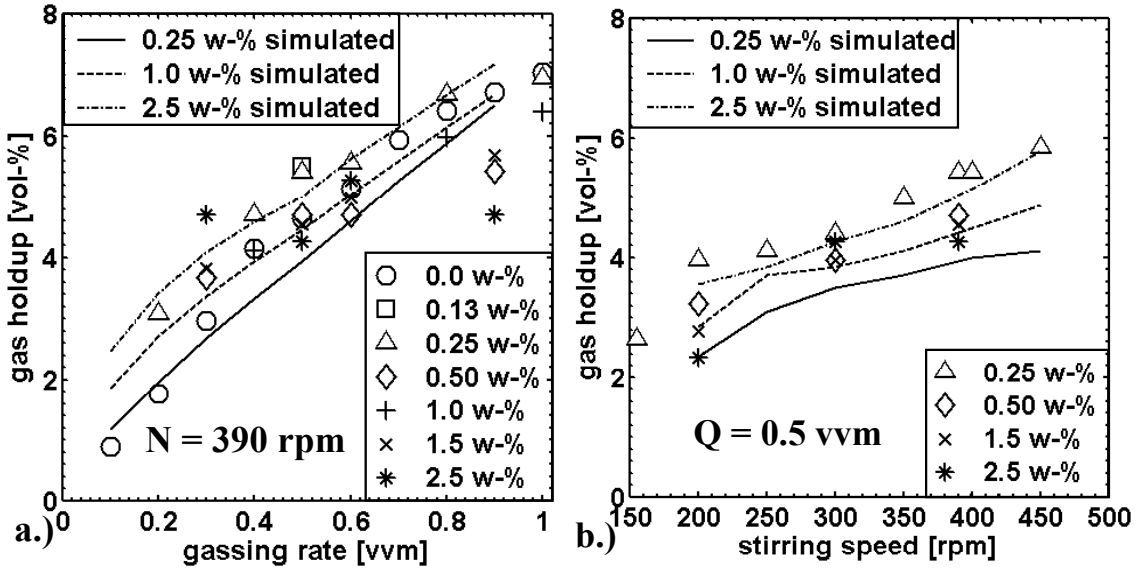

Figure 25. Simulated (fitting D) and measured gas holdups at varying a.) gas feeds and b.) stirring speeds at varying xanthan concentrations in the 200 L tank.

6.5 Predicted vs. measured gas-liquid mass transfer

6.5.1 Air – water

Figure 26 presents a comparison between the fittings A and C and oxygen absorption and desorption experiments. The agreement is good for varying agitation conditions. This also gives further confidence to the validated bubble breakage and coalescence closures.

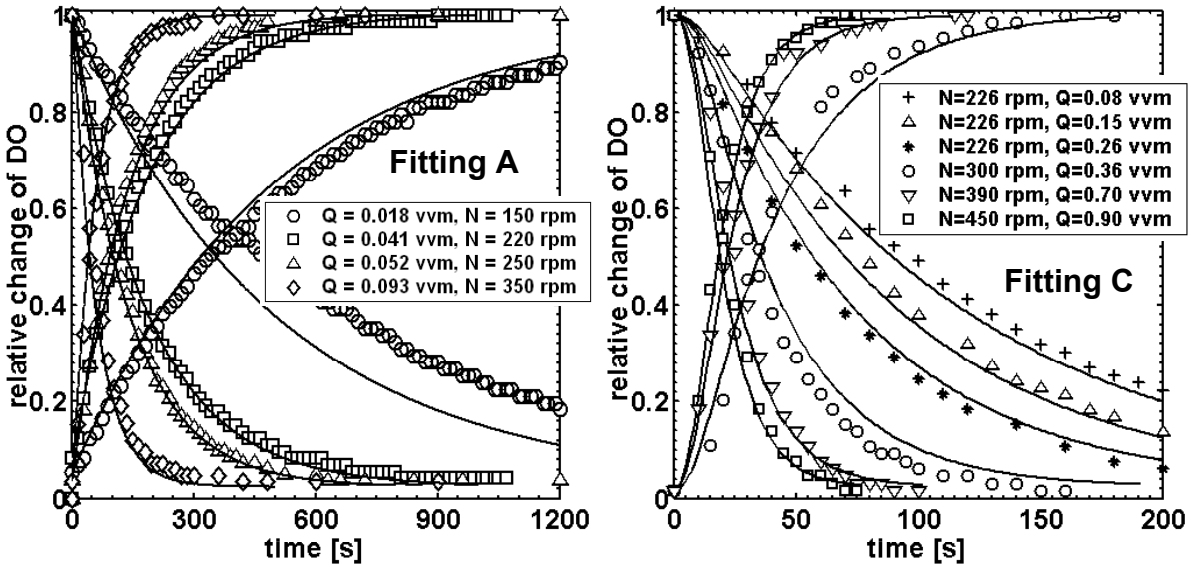

Figure 26. Simulated (lines) and measured (markers) oxygen concentration profiles during desorption and absorption, air – tap water, 200 L tank.

Local mass transfer coefficients are calculated from the multiblock and CFD simulation results as

$$k_L a' = \frac{N_{GL,O2}(t) \cdot A_{GL}}{c_{L,t}\left(x_{I,O2}(t) - x_{B,O2}(t)\right)}. \tag{59}$$

The vessel-averaged mass transfer coefficients are then obtained from

$$\overline{k_L a'} = \frac{1}{V_{Lt}} \sum_{i=1}^{NB} V_{L,i} \cdot k_L a'. \tag{60}$$

The predicted volumetric oxygen transfer coefficients from Eq. (60) were compared to some empirical $k_L a$-correlations to evaluate the adjusted model (fitting C). Middleton (1992) has presented the following correlation

$$k_L a(20^\circ C) \Big/ s^{-1} = 1.2 \cdot \left(\frac{P_g / kW}{V_L / m^3} \right)^{0.7} \cdot \left(v_s / m \cdot s^{-1} \right)^{0.6}, \quad (\pm 10\,\%), \tag{61}$$

which was claimed to avoid the effect of gas phase dynamics. Kapic and Heindel (2006) developed a correlation for 'After Large Cavity'–flow regime

$$k_L a \Big/ s^{-1} = K \cdot \left(v_s / m \cdot s^{-1} \right)^E \left(\frac{N}{N_{CD}} \right)^F \left(\frac{T}{D_I} \right)^G, \tag{62}$$

where K = 1.59, E = 0.93, F = 1.342 and G = 0.415. Eq. (62) is based on total 282 data point from several literature sources and was reported to describe the measurements within ±20 % accuracy. Yawalkar et al. (2002) fitted the correlation of type Eq. (62) without geometry parameter T/D_I for the agitated tanks of diameter T = 0.39 to 2.7 m. The fitting was made against data from several experimental studies in literature. The accuracy of correlation was found to be ±22 %. The resulting parameter values were K = 3.35, E = 1.0, F = 1.464 and G = 0.

The minimum impeller speed for complete dispersion N_{CD} in Eq. (62) is evaluated from (Nienow et al. 1977)

$$N_{CD}/s^{-1} = \frac{4 \cdot \left(Q/m^3 s^{-1}\right)^{0.5} \left(T/m\right)^{0.25}}{\left(D_I/m\right)^2} \tag{63}$$

The simulated, vessel-averaged mass transfer coefficients from Eq. (59) are compared to the correlations of Middleton (1992), Yawalkar et al. (2002) and Kapic and Heindel (2006) in Figure 27a. The simulations agree (±20 %) with the correlation of Middleton (1992), while they differ significantly from the correlations of Yawalkar et al. (2002) and Kapic and Heindel (2006) at k_La's larger than 0.04 s^{-1}. Figure 27b presents the same comparison with an exception that k_Las are determined by fitting Eq. (7) to the simulated and measured 'oxygen concentration vs. time'–profiles. The simulated k_Las agree with the present measurements as expected, but it is interesting that they also agree with the correlations of Yawalkar et al. (2002) and Kapic and Heindel (2006). The difference to the correlation of Middleton (1992), instead, is larger with this definition of k_La.

The results in Figures 27a and 27b indicate that k_La-correlations of Yawalkar et al. (2002) and Kapic and Heindel (2006) include the effects of non-ideal mixing, apparently, because ideal-mixing has been assumed commonly in the analysis of mass transfer model parameters from the experiments (Eq. 7). It therefore seems that vessel-averaged k_La-correlations are not be suitable for the calculation of local mass transfer rates. The dependence of mass transfer model on flow fields can be minimised by using a detailed stirred tank model for the analysis of mass transfer experiments similarly as in the present work. The influence of varying modelling assumptions is evaluated next based on the multiblock simulations.

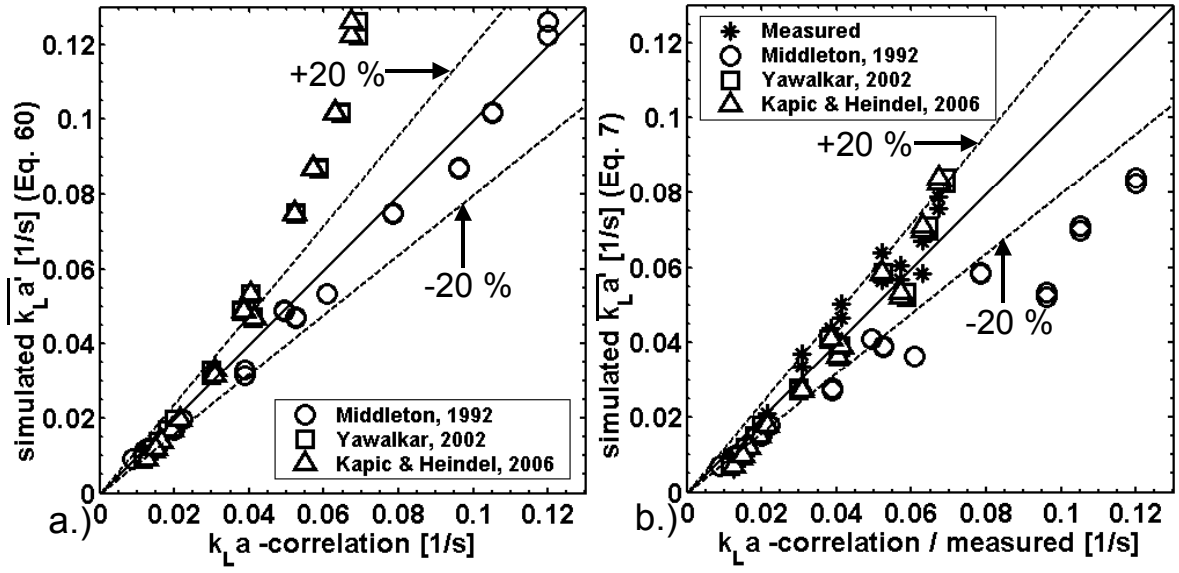

Figure 27. a.) Simulated (fitting C) k_Las vs. the correlation of Middleton (1992), b.) Simulated (fitting C) k_Las (Eq. 7) vs. measured k_Las (Eq. 7), air – tap water, 200 dm^3 tank.

The simulated and measured concentrations of oxygen and nitrogen in exit gas during oxygen desorption are compared in Figure 28a. A quantitative comparison is presented in Table 4, where the simulated and measured times for reaching 5 % of the initial oxygen concentration are shown. During the first 20 seconds, exit gas concentrations change rapidly after which slow oxygen transfer rates become a limiting step. The comparisons in Figure 28a and Table 4 indicate that multiblock model describes gas phase dynamics successfully under varying vessel-operating conditions.

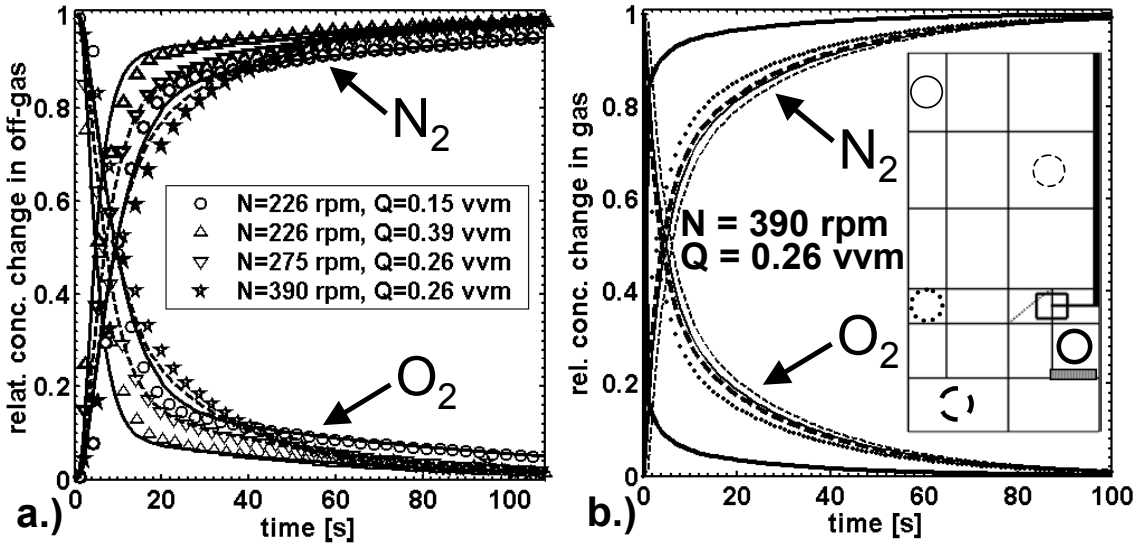

Figure 28. a.) Simulated and measured a.) off-gas concentrations b.) local gas concentrations during oxygen desorption, air – tap water, 200 dm^3 tank.

The simulated spatial inhomogeneity of oxygen in gas phase is presented for one simulation case on the right hand side of Figure 28b. Near the gas sparger, concentrations change rapidly while above the impeller the change is much slower as expected. The simulations show that gas phase is neither ideally mixed nor plug flow. Gas phase concentrations affect the mass transfer, because instant gas solubilities and hence the driving force depend on them.

Table 4. The predicted and measured times needed for reaching 5 % of the initial oxygen concentration in the off-gas during oxygen desorption.

N [rpm]	Q [vvm]	Measured [s]	Predicted [s]
225	0.15	107	108
225	0.26	63	65
225	0.39	45	41
275	0.26	67	65
390	0.26	63	59

Figure 29 presents the inhomogeneity of oxygen transfer coefficients (Eq. 59) in two simulation cases. At high agitation speed and low gas feed (Q=0.36 vvm, N=475 rpm) bubbles are smaller and gas is dispersed effectively below the impeller thus leading to more homogeneous k_Las compared to the case where stirring speed is low and gas feed is high (Q=0.7 vvm, N=312). Mass transfer rates are largest near the gas sparger, in the impeller discharge flow and near the wall where mass transfer area, turbulence dissipations and the driving forces are largest. The driving forces vary mainly due to changes in gas phase concentrations (Figures 28a and 28b). The liquid phase concentrations are practically homogeneous. The hydrostatic pressure slightly improves gas solubilities at the bottom of tank, but due to small liquid height pressure effect is small.

The analysis of multicomponent mass transfer effects showed that liquid side diffusion controls the transfer of oxygen, nitrogen and argon, although there is small resistance in the gas side as well. Interfacial gas concentrations (y_I) deviate generally less than 0.5 % from the bulk gas compositions (y_B) for other components but water. Water vaporises to dry gas feed

and up to 20 % differences between interfacial and bulk gas compositions can exist near the gas sparger. The interactions between transferring components showed to be negligible. Obvious reasons are the similarity of binary diffusion coefficients and small gas solubilities. Similarly, the influence of high flux correction was small. Due to its generality the present mass transfer model is applicable to cases where multicomponent interactions and gas side mass transfer resistances are significant. This may occur, if dissimilar chemical compounds are present, pressure is high or components are more soluble. It is emphasized that the computational cost of present mass transfer model is only slightly higher compared to simpler, less rigorous models, if good initial guess e.g. from previous time step is available for the iteration of fluxes.

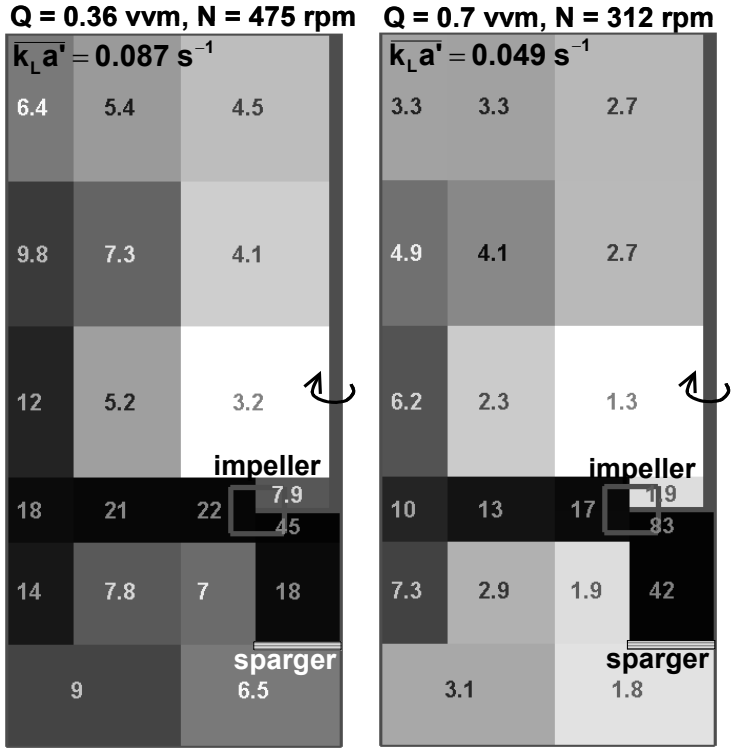

Figure 29. Predicted (fitting C) local oxygen transfer coefficients k_La' [$\cdot 10^{-2}$/s] in air – tap water system, 200 L tank.

6.5.2 Air – aqueous xanthan

The predicted oxygen concentration profiles from the fitting D (Table 3) are compared to the measurements in Figure 30. Electrolytes were included to aqueous xanthan to mimic actual fermentation broths [VII]. The fitting describes the influence of vessel operation conditions and xanthan concentration on mass transfer successfully. This gives further confidence to the mass transfer area predictions with the PBs. A comparison of multiblock simulations to the empirical correlation of Garcia-Ochoa et al. (2000) for actual xanthan fermentation broths at higher xanthan concentrations showed similarly good agreement [VII]. This indicates that the adjusted model is applicable to the modelling gas-liquid mass transfer in actual xanthan fermentation broths.

The simulated local k_Las in the laboratory tank at three xanthan concentrations are presented in Figure 31. The effective volume available for mass transfer decreases with increasing xanthan concentration. The reason is the increase of liquid viscosity, which causes the decrease of turbulence energy dissipations and the increase of bubble sizes (Figure 24) resulting into smaller gas-liquid interfacial areas in the quiescent regions of tank.

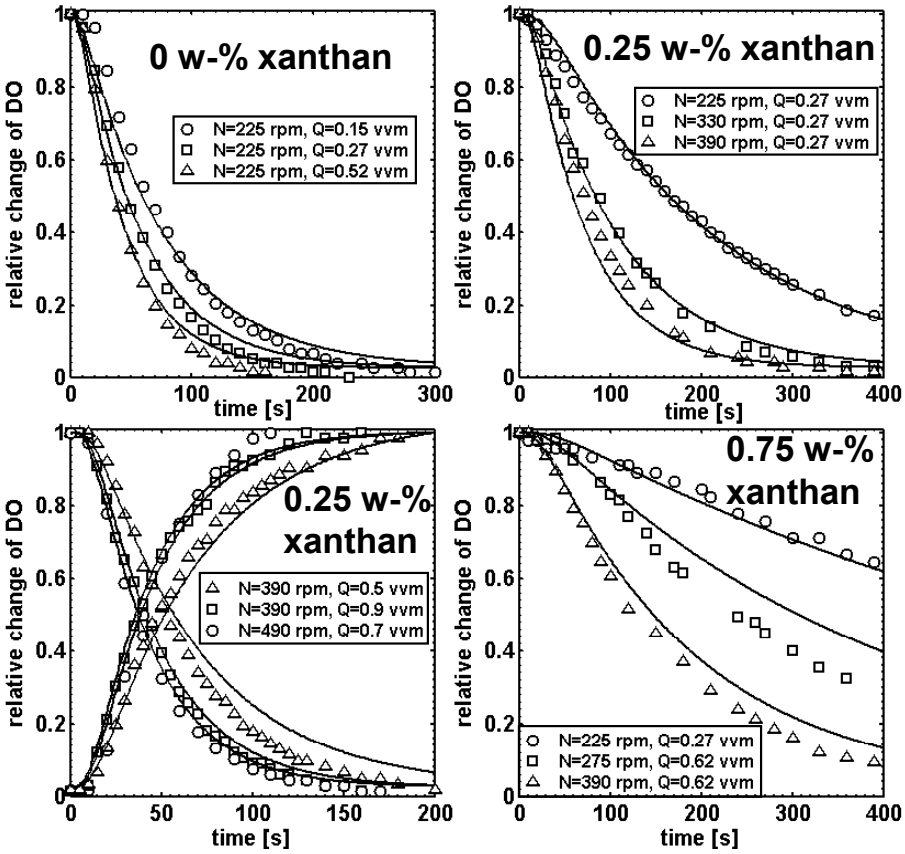

Figure 30. Simulated (fitting D) and measured dissolved oxygen concentrations in aqueous xanthan during absorption and desorption at varying agitation conditions, 200 L tank.

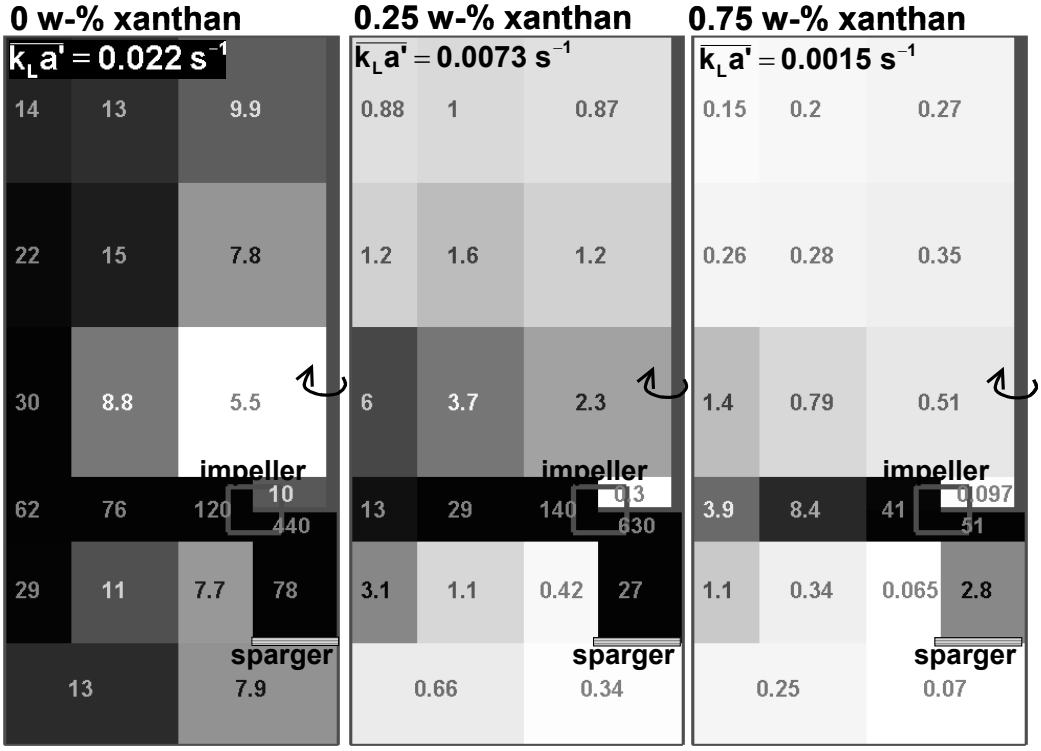

Figure 31. Predicted (fitting D) local k_La's [$\cdot 10^{-3}$/s] at varying xanthan concentrations, 200 L tank, N = 225 rpm, Q = 0.27 vvm.

7. GAS-LIQUID MASS TRANSFER SIMULATIONS WITH CFD

7.1 CFD implementation

The multicomponent gas-liquid mass transfer model and the physical property/component databases of Flowbat flowsheet simulation program (Aittamaa and Keskinen, 2005) were incorporated to a commercial CFD program (CFX-5.7) through user routines [VIII]. The linking of CFD program and user models is illustrated in Figure 32.

The Flowbat database and the input file are loaded at the start of mass transfer simulation by calling the FLOWIN routine. The chemical components and the thermodynamics supplied by Flowbat, the needed user workspace and other model parameters are defined in a separate input file. The transferring components are defined in the CFD program as user scalars with convection and diffusion in both gas and liquid phase. Mass transfer is defined through source and sink terms, which are calculated by calling the linking routine MTRSRC. The MTRSRC routine passes local turbulence dissipations, pressure, temperature, concentrations and the initial guess to the mass transfer model. The convergence within just few iteration steps is ensured by saving the result to the user data area (MMS). The result is then used as an initial guess for the next iteration. At the end of simulation, user workspace is deleted and Flowbat database is closed (FLOWEN).

Local gas-liquid interfacial transfer areas are calculated from the MUSIG population balance model of CFX-5.7 (Lo, 2000) with the adjusted bubble breakage and coalescence models. Local turbulent energy dissipation rates predicted by the turbulence model are scaled with the measured power consumption of mixing. The scaled local energy dissipations are then passed to breakage, coalescence and mass transfer models. This minimises the dependence of results on the turbulence model and the CFD simulation grid. The interfacial drag is calculated based on local Sauter mean diameters by including the turbulence dampening of slip (Eq. 32).

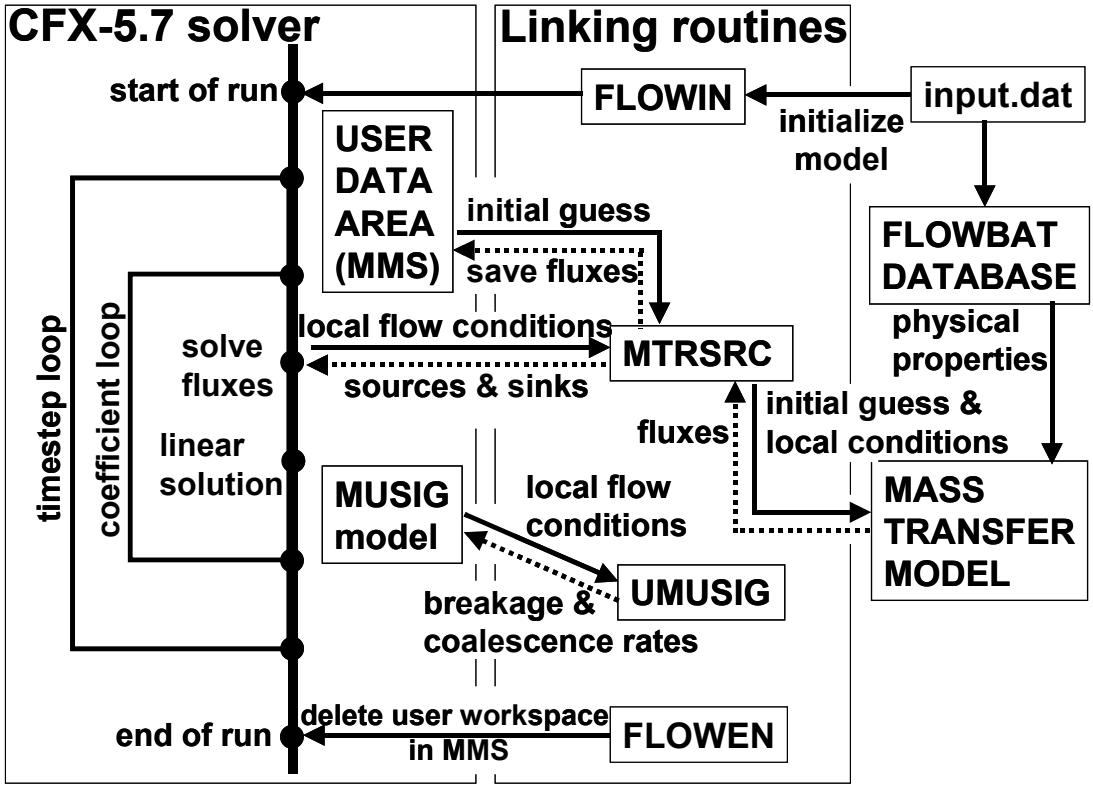

Figure 32. The linking of mass transfer model to CFX-5.7.

7.2 Simulation of local gas-liquid mass transfer in a 200 L tank

The coupled 'mass transfer – PB – CFD' -model was used to investigate gas-liquid mass transfer in the 200 L laboratory stirred tank [VIII]. Water, oxygen, nitrogen and argon were included as transferring components in the simulations. A 180° segment of the grid was modelled with a structured grid of 109 000 volume elements. The simulations were made with the standard k-ε turbulence model and MRF technique of impeller motion. The fitting C was used (Table 3). The BSDs were described by 20 MUSIG size classes with geometric discretization. The drag coefficients were calculated from the correlation of Tomiyama (1998) (Eq. 31) based on local Sauter mean diameters. The turbulence dampening of slip (Eq. 32) was included. The BSDs at gas inlet were estimated from the photographing measurements.

Three combinations of stirring speed and gassing rate were investigated: 300 rpm/0.36 vvm; 390 rpm/0.7 vvm; 450 rpm/0.9 vvm. The CFD results showed slight dependence on time step. A short time step should produce more accurate predictions. This however leads to long computation times, because process time needs to be simulated roughly 25 seconds to get a converged pseudo steady-state solution. Therefore time step was decreased gradually from 50 ms at the start to 5 ms at the end of simulation. The computation time for reaching a pseudo steady-state solution was approximately 10 days cpu-time in a linux (1.7 GHz AMD/1 Gb) workstation. The iteration of fluxes (abs. tolerance $1 \cdot 10^{-19}$) took ~9 % of the total CPU time. Good initial guess from the previous time step was important for the rapid convergence of fluxes within few iteration steps.

The CPU-time requirement of CFD is more than 1000-fold compared to the multiblock model, but the results are still comparable. It therefore seems that the multiblock model is an optimal trade-off between computational cost and accuracy. The computational efficiency of the coupled 'mass transfer – PB – CFD'-model could be improved by using alternative methods for the solution PBs. The method of moments (Ramkrishna, 2000) requires fewer equations for an accurate solution thus decreasing the computational cost compared to the traditional method of classes. Another alternative could be the high-order moment-conserving method of classes of Alopaeus et al. (2006), which produces very accurate solutions of PBs with low number of bubble size classes.

The CFD simulations in Figure 33 show a strong inhomogeneity of oxygen transfer coefficients in the agitated tank. The distribution of $k_L a$'s is very similar to the multiblock model predictions in Figure 29. The largest oxygen transfer coefficients are found in the impeller region, near the gas sparger and near the wall where dissipation rates are high. The accumulated gas behind impeller blades in gas cavities, near the wall below the impeller and in the centre of upper liquid circulation loop explains high local $k_L a$s. Local Sauter mean bubble diameters are large in the downward liquid flow near the wall below the impeller, where high gas holdup promotes coalescence, and near the impeller shaft above the impeller. Large bubble diameters partly compensate the increase of mass transfer area in the regions where gas holdup is high.

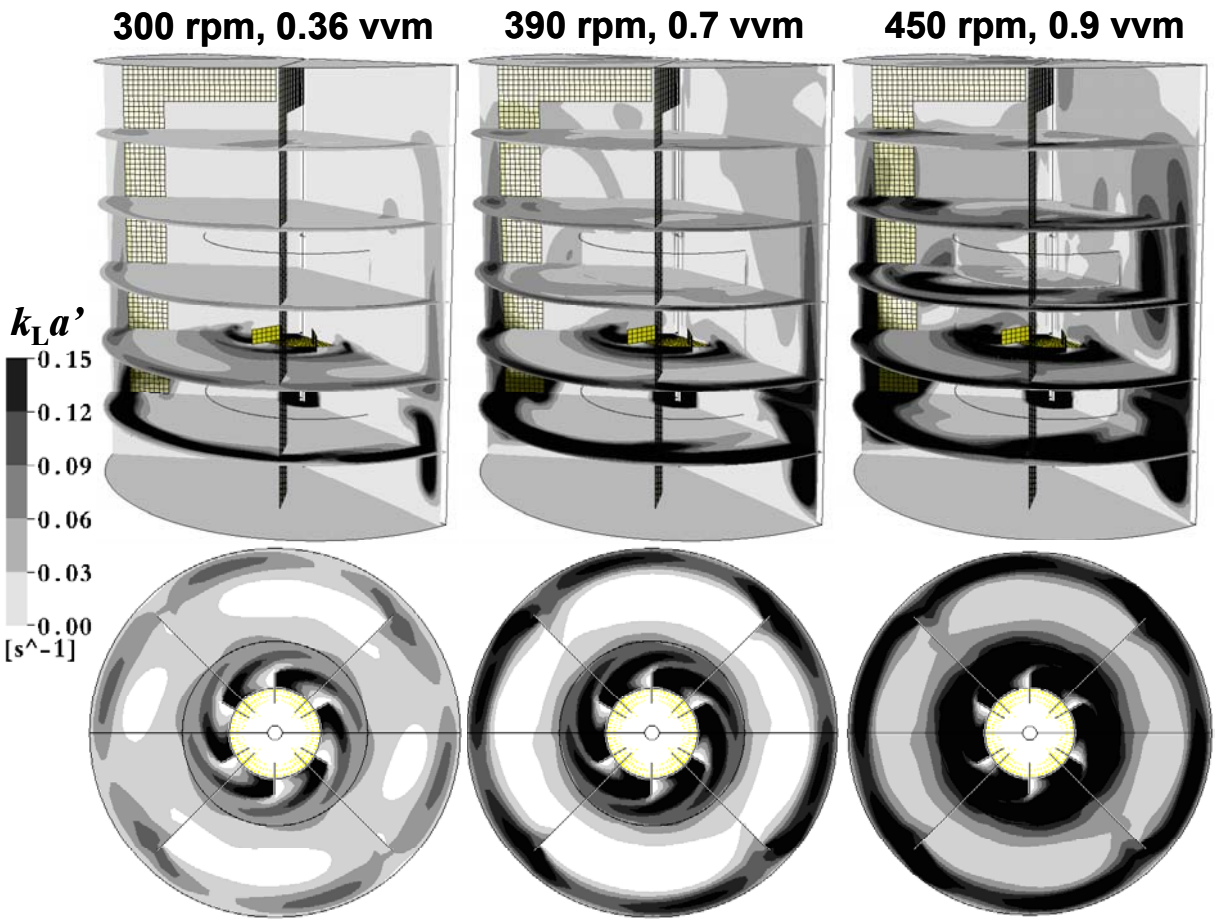

Figure 33. Predicted local oxygen transfer coefficients k_La' [s^{-1}] from CFD. The horizontal cut plane is at height T/3 from the bottom of tank (impeller plane).

A direct comparison between CFD simulations and mass transfer experiments is not possible, because the simulation of 'dissolved oxygen vs. time'–profiles is time-consuming. Therefore, CFD predictions were compared to the multiblock simulations. This should be a reasonable approximation, because multiblock simulations were validated against local BSD, overall gas holdup and oxygen transfer experiments. The vessel-averaged mass transfer parameters are compared in Table 5. The CFD slightly overpredicts bubble size and underpredicts $\overline{k_La'}$ compared to the multiblock model. This shows the sensitivity of mass transfer to local BSDs. Overall, the results are in the same range. The differences may partly result from the small number of bubble size classes and the assumption of common velocity field for bubble size classes in the MUSIG model. It is also noted that the multiblock model averages flow-fields compared to CFD.

Table 5. Vessel-averaged mass transfer parameters, **CFD (bold),** #multiblock simulation.

N [rpm]	Q [vvm]	d_{32} [mm]	α [vol-%]	A_{GL} [m^2/m_L^3]	$\overline{k_La'}$ [s^{-1}]
300	0.36	**3.0**, #2.8	**2.8**, #2.5	**50**, #56	**0.029**, #0.033
390	0.7	**3.2**, #3.1	**5.3**, #5.4	**91**, #105	**0.061**, #0.075
450	0.9	**3.6**, #3.1	**8.2**, #7.8	**126**, #151	**0.086**, #0.124

8. DYNAMIC MODELLING OF BATCH XANTHAN FERMENTATION

8.1 Xanthan fermentation cases

The validated population balance closures, mass transfer model (fitting D) and the fermentation kinetics of Garcia-Ochoa et al. (2000) were combined to the multiblock fermenter model (Figure 11) to investigate the dynamics of batch xanthan fermentation [VII]. Xanthan fermentation was chosen for the study, because it is a typical example of the process, which is limited heavily by the gas-liquid mass transfer and non-ideal mixing. The economical value of this process is significant. This apparently explains why it has been studied so widely. The apparent viscosity of broth increases during the fermentation. This causes a significant oxygen transfer limitation to the microbial growth.

The effects of mixing on xanthan fermentation were investigated in two simulation cases: at constant agitation speed (**S1**) and at gradually increasing agitation speed (**S2**). Biomass, xanthan, nitrogen and carbon source were included as reacting scalar components in the liquid phase. Water, carbon dioxide, nitrogen and oxygen were included as transferring components between gas and liquid. The consumption of dissolved oxygen and the production of carbon dioxide act as a link between bioreaction kinetics and gas-liquid mass transfer. The BSDs were described by 40 bubble size classes. More size classes would have slightly improved the numerical accuracy of the PB solution, but this was not critical compared to other modelling uncertainties. The details of simulation setup and initial conditions are presented in the paper [VII].

The simulation of a 70-hour fermentation batch took approximately four days wall-clock time. The simulation time is rather long and seems to result from strong skewing of BSDs. Few large bubbles constitute a significant fraction of the gas volume, but their breakage rates are high. This necessitates a short integration time step. It is noted that the updates of PB discretization and low updating frequencies for local phenomena and flow fields increased the computation speed significantly.

8.2 Overall performance of fermenter

The predicted overall performance of fermenter is presented in Figure 34. The comparison between cases S1 and S2 shows the positive effect of stirring speed on fermentation. The time needed for reaching the final xanthan concentration (2.5 w-%) is 70 hours for the S1 while only 29 hours are needed in the case S2. During first few hours of fermentation DO concentration is 100 sat-%. After this, DO decreases rapidly below 30 % of the saturation. In the case S2, DO decreases more slowly compared to S1, because mass transfer and mixing limitations are partly compensated by increasing the agitation speed. The mass transfer limitation mostly results from the decrease of gas-liquid interfacial area. Oxygen transfer rates are small at the start of fermentation, because microbial concentrations and xanthan production rates are small, but increase rapidly reaching a maximum. Due to oxygen transfer limitation xanthan reaction rates decrease towards the end of fermentation. The simulated trends agree with experimental xanthan fermentation studies (Garcia-Ochoa et al. 2000, Amanullah et al. 1998).

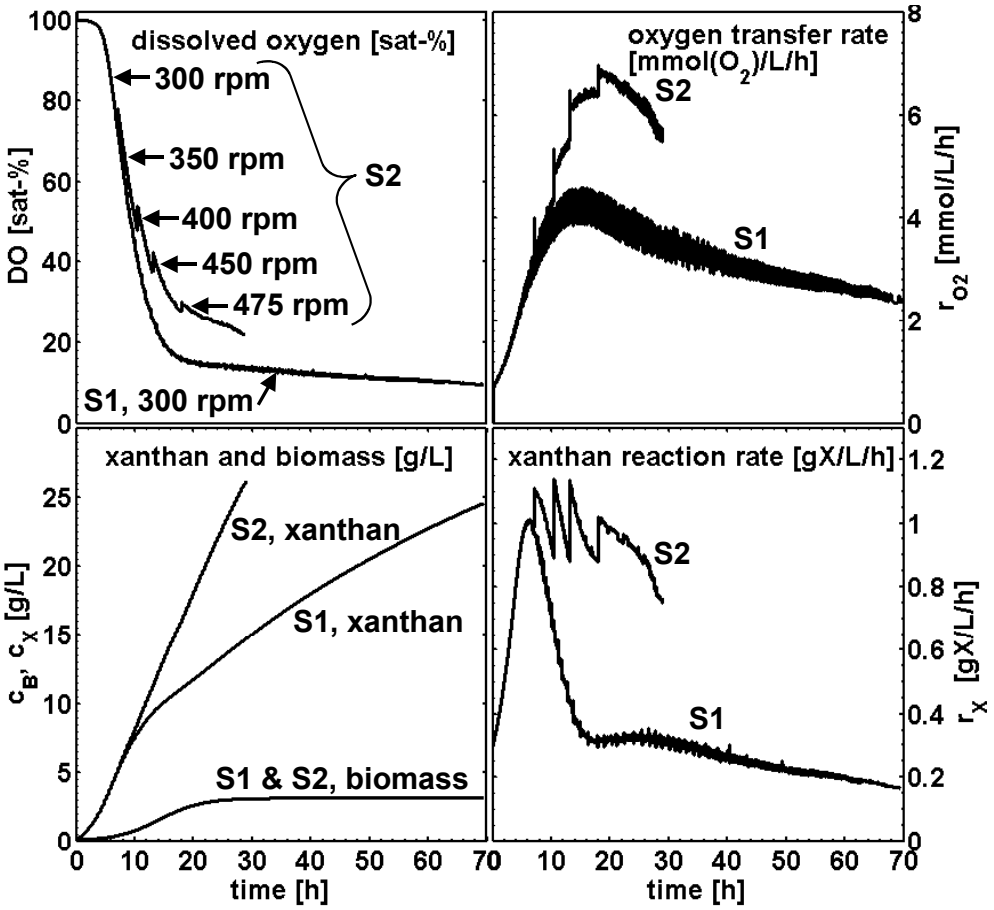

Figure 34. Predicted overall performance of pilot xanthan fermenter.

8.3 Local mass transfer and reaction conditions

Figure 35 presents local mass transfer and reaction conditions in the fermenter at the end of fermentation batch at agitation speed 300 rpm (case S1). High turbulence energy dissipations favour the bubble breakage leading to larger mass transfer rates and DO concentrations in the impeller regions. The DO concentrations and reaction rates are distributed more homogeneously than bubble size or $k_L a$. It seems that even low liquid flow rates smooth out the inhomogeneity of DO while xanthan reaction rates are related strongly to local DO. Mass transfer occurs also in the quiescent zones of reactor. Tiny bubbles have low slip velocities and they are transported to quiescent zones even at low liquid flow rates. Due to continuous breakage-coalescence process in the impeller region, these tiny bubbles seem to be effective for the mass transfer.

Statistical analysis showed that reaction rates are more homogeneous at high (S2) than at low (S1) agitation speed as expected [VII]. The overall inhomogeneity of reaction mixture is largest at the time when oxygen transfer rates are largest (Figure 34). The hydrostatic pressure gradient and the depletion of oxygen from gas cause the decrease of xanthan reaction rates towards the surface of dispersion. At high xanthan concentrations, liquid viscosity increases and most of bioreaction occurs in the impeller zones (Figure 35). This explains why local reaction rate gradients increase towards the end of fermentation batch in both simulation cases [VII].

Xanthan fermentation studies show that the multiblock reactor model together with the population balances for bubbles, rigorous mass transfer model and bioreaction kinetics allows detailed investigation of agitated gas-liquid reactors. It is emphasized that with this modelling

approach long-term reactor performance can be analysed. This is not possible with CFD at present computational capabilities, when rigorous submodels are incorporated in the simulations.

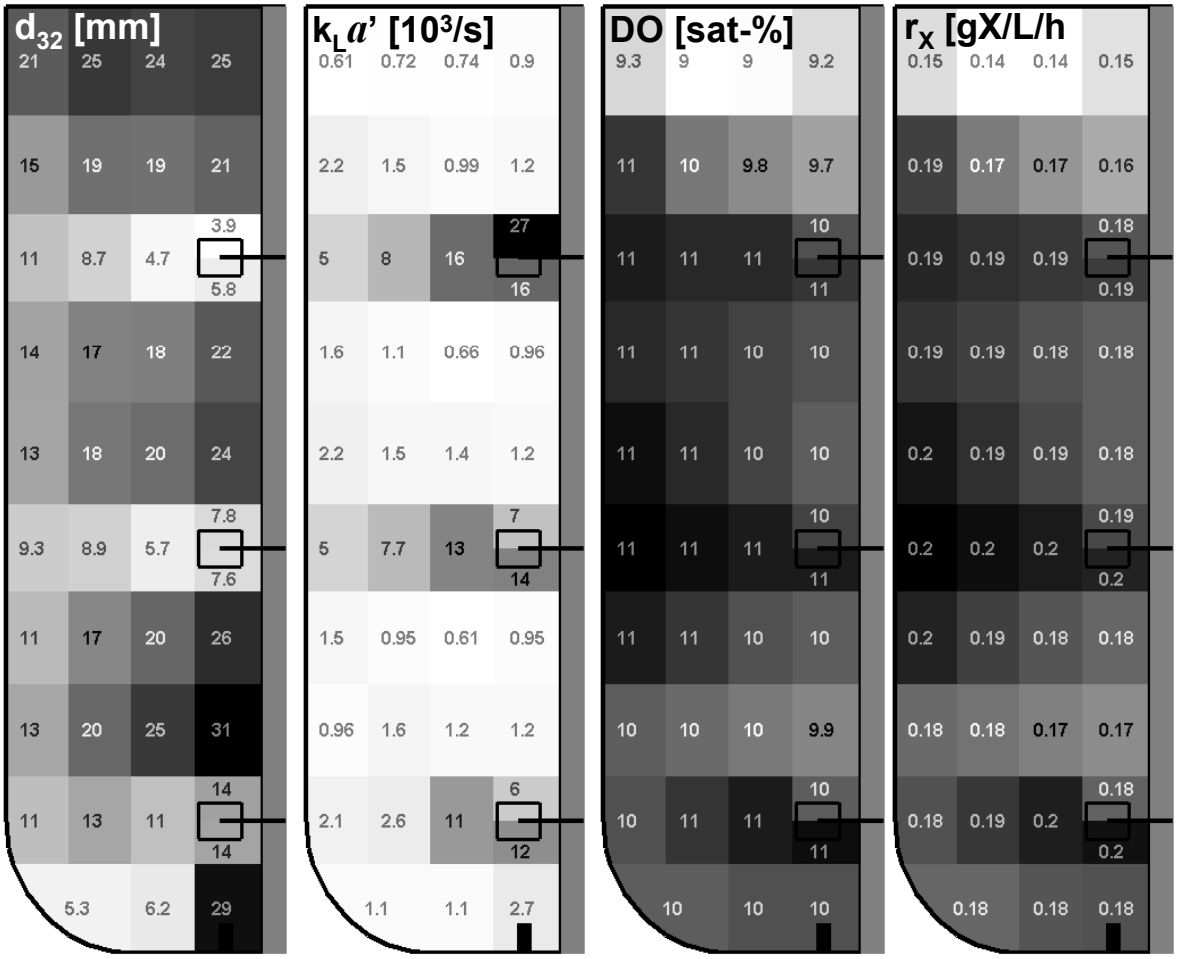

Figure 35. The predicted local mass transfer and reaction conditions in the pilot xanthan fermenter, N=300 rpm, c'_x=2.4 w-%, t=65 h.

9. CONCLUSIONS

Rigorous gas-liquid mass transfer models were developed and validated against experiments for agitated gas-liquid reactors. Local mass transfer fluxes and gas-liquid interfacial areas originate from different phenomena and were modelled separately. Fluxes were described based on the two-film theory and simplified solution of Maxwell-Stefan multicomponent diffusion. Local Bubble Size Distributions (BSDs) and mass transfer areas were solved from the Population Balances (PB) for bubbles.

Local BSDs were measured from agitated laboratory tanks to get information for the model validation. The measurement of local BSDs showed to be a demanding task, because bubble sizes vary in a wide range. The limitations of detectable bubble size range cause the biasing of BSDs. The photography seems to be the most reliable technique for bubble size measurements, but it cannot be applied easily for dense and opaque dispersions. The manual analysis of bubbles from photographs is needed in these cases due to problems with automatic bubble identification and the arrangement of lightning. From lean dispersions, flow fields can

be measured simultaneously with other hydrodynamic parameters by incorporating bubble size analysis techniques to particle image velocimetry.

The experiments showed a significant spatial inhomogeneity of BSDs in the laboratory stirred tanks. The population balances are a natural choice for the modelling of local BSDs, which are related complicatedly to bubble breakage and coalescence rates, slip velocities and liquid flow fields.

A multiblock stirred tank model with the adaptively discretized population balances for bubbles and multicomponent gas-liquid mass transfer model was developed. The model considers the inhomogeneity of dispersion and is computationally efficient. This makes it useful for the fitting of unknown model parameters and investigation of long-term dynamics. The multiblock model flow fields were obtained from the CFD simulations. This was laborious but can be accelerated by developing suitable algorithms.

The fitting of unknown parameters in phenomenological bubble breakage, coalescence and turbulent slip models was needed to predict local BSDs accurately. The models were adjusted to describe both number and volume BSDs. This issue has been neglected in most studies, where only mean diameters or number BSDs have been compared. The multiblock model was used to describe macroscopic inhomogeneities of dispersion in the fitting to minimise the effect of vessel geometry on the adjusted models.

The validated models predict the influence of physical properties and vessel operating conditions on local BSDs in a limited range. The mass transfer simulations with the validated mass transfer and PB closures are in good agreement with the oxygen transfer and exit gas experiments. The stirred tank simulations with the breakage and coalescence closures of Lehr et al. (2002) show that care is needed, when models are transferred to a new flow environment. The fitting studies indicate that measured local BSDs alone are not sufficient for the validation of bubble breakage, coalescence or turbulent drag mechanisms. Experimental and modelling uncertainties cannot be attributed to a specific error source due to many superimposed phenomena and the complexity of gas-liquid mixing. More basic research and isolated experiments from turbulent flows and dense gas-liquid dispersions are needed. Comparisons between simulated and measured local BSDs from agitated tanks are useful for validating the overall model performance. The fitting can also guide in the development of new models.

Turbulent energy dissipation is an important parameter in the mass transfer modelling but its accurate estimation is often difficult. So far, most validation studies have focused on the investigation of bubble columns. The experiments under mild turbulence conditions may not be adequate for validating breakage and coalescence closures in which turbulence is the driving force. In agitated tanks, turbulent energy dissipation can be related to the power consumption of impeller, which can be measured quite easily. In the CFD simulation studies local dissipation rates should be scaled based on experimental values before they are passed to the closure models. This minimises the dependence of results on the simulation grid and the turbulence model.

The comparison of multiblock and CFD simulations showed that multiblock model is an optimal trade-off between the accuracy and CPU time, when local mass transfer rates are of interest. Both modelling approaches with the validated closure models predict a significant inhomogeneity of mass transfer in the 200 L laboratory stirred tank. This results mostly from the spatially varying gas-liquid interfacial areas, but also from varying gas phase concentrations and turbulence energy dissipations. Traditional k_La-correlations include the effects of non-ideal mixing and seem not to be suitable for the calculation of local mass transfer rates. The models validated in the present work include no geometry dependent

parameters, are related to local micro-scale turbulence and local physical properties of dispersion. Therefore they should be suitable for detailed reactor scale-up and design studies.

The validated population balance and mass transfer closures for aqueous xanthan together with the bioreaction kinetics from literature were incorporated to the multiblock fermenter model to investigate batch xanthan fermentation. The simulation results show the need of population balances for the detailed investigation of reactive, viscous gas-liquid dispersions in which mass transfer and mixing limitations are present. The model describes the effects of mixing on reactor performance successfully. The results highlight the potential of multiblock modelling for the detailed investigation of complex multiphase reactors.

10. NOTATION

$\#(v_p/2)$	index number of bubble size class of characteristic volume $v_p/2$
a	surface area of bubble, m^2
a_h	projected area of bubble in the direction of flow (Eq. 30), m^2
A_{GL}	specific mass transfer area, m^2/m^3liquid
A	flow area between adjacent subregions (see Figure 9), m^2
a_{ij}, b_{ij}	adjustable parameters in Eq. (24)
$b(d_n)$	bubble growth rate, m/s
B	baffle width (Eq. 26), m
$B(d_n)$	volumetric bubble growth rate, m^3/s
c	concentration, mol/m^3
c'	concentration, kg/m^3
C_1, $C_3 - C_8$	
C_{10} - C_{11}	adjustable model parameters
C_2	adjustable model parameter, $m^{-2/3}$
C_9	adjustable model parameter, m^{-2}
C_D	bubble drag coefficient
C_{flow}	correction factor defined by Eq. (27)
d	bubble diameter, m
d_{10}	arithmetic mean diameter ($=\Sigma d_i/\Sigma i$), m
d_{32}	Sauter mean diameter ($=\Sigma d_i^3/\Sigma d_i^2$), m
D	diffusion coefficient, m^2/s
D_I	impeller diameter, m
Eo	Eotvos number ($=d^2g(\rho_L - \rho_G)/\sigma$)
$erf()$	error function
$erfc()$	complementary error function
$E(d)$	bubble aspect ratio
f	breakage volume fraction (Eq. 35)
F^*	liquid flow number defined by Eq. (14)
F_I^*	impeller flow number defined by Eq. (26)
F_B	bubble induced backflow of liquid due to slip, m^3/s
F_{drag}	drag force on bubble, $kg/m/s^2$
F	liquid flow rate, m^3/s
Fo	Fourier number ($=D_G \cdot t_{life}/d_{32}^2$)
g	acceleration due to gravity ($=9.81\ m/s^2$)
$g(d_n)$	breakage rate, 1/s
$h(d_n,d_p)$	coalescence rate, m^3/s
$H(T,p)$	Henry's law constant at temperature T and pressure p, Pa

k mass transfer coefficient, m/s
K consistency index in the power law viscosity model, $kg \cdot s^{n-2}/m$
k_La mass transfer coefficient defined by Eq. (7), 1/s
k_La' local mass transfer coefficient defined by Eq. (59), 1/s
L distance to the surface of dispersion, m
m amount of scalar, kg
N agitation speed, 1/s
N_{GL} mass transfer flux, defined positive from gas to liquid, $mol/m^2/s$
n flow index
$n(d_i)$ dimensionless number density of bubbles (Eq. 1).
n_b number of observed bubbles in an experiment, Eqs. (1) and (2)
NB number of multiblock model subregions
NC number of chemical compounds
n_G moles in gas phase, mol
n_L moles in liquid phase, mol
NP number of bubble size classes
N_p power number of mixing (Eq. 56)
NS number of scalar components in liquid phase
P mixing power, $kg \cdot m^2/s^3$
p pressure, $kg/m/s^2$
Q gas feed to the vessel or gas funnel, m^3/s
r reaction rate, mol/m^3liquid/s
r' reaction rate, kg/m^3liquid/s
R_{ab} ratio of minor and major axes of an oblate or prolate ellipsoid
Re bubble reynolds number ($=d \cdot U_{slip} \rho_L / \mu_L$)
Re_I impeller Reynolds number ($=D_I^2 \cdot N \cdot \rho_L / \mu_L$)
s variable in Eq. (24)
T diameter of tank, m; or temperature, K
t time, s
U bubble or gas velocity, m/s
v_n bubble volume, m^3
$v(d_n)$ dimensionless volume density of bubbles (Eq. 2)
V_i volume of subregion, m^3
$V_{L,i}$ volume of liquid in a subregion, m^3
$\overline{V}_{G,m}$ partial molar volume in gas, m^3/mol
v_s superficial gas velocity, m/s
V_{Lt} total liquid volume in the tank, m^3
vvm gas feed rate, m^3gas/m^3liquid/min
We Weber number, ($=\rho_L d^{5/3} \varepsilon^{2/3} / \sigma$)
x component mole fraction in the liquid
y component mole fraction in gas
Y_k number of bubbles per unit volume, $1/m^3$
z total composition of mixture, (); or axial coordinate, m
$\hat{z}$ unit vector in axial direction
Z bubble size discretization parameter

Greek letters

∇p dynamic pressure gradient, $kg/m^2/s^2$
∇p^* scaled dynamic pressure gradient, kg/m^2
$[\Xi]$ high flux correction matrix in Eq. (48)

α	volume fraction
$\beta(d_n,d_p)$	probability that a bubble of size d_n is formed when d_p breaks, 1/m
γ	shear rate, 1/s
γ *	dimensionless shear rate
Δd	the width of bubble size category, m
ε	dissipation rate of turbulent energy, m^2/s^3
θ	rotational coordinate, radians
$\lambda(d_n,d_p)$	coalescence efficiency
λ_{min}	minimum size of turbulent eddy, m
μ	molecular viscosity, kg/m/s
μ_{eff}	effective (= molecular + turbulent) viscosity, Eq. (32), kg/m/s
ξ	ratio of minimum eddy size and bubble size (Eq. 35)
ρ	density, kg/m^3
σ	surface tension, kg/s^2
τ	lag time, s
τ_{flow}	relaxation parameter in Eq. (25)
φ	relative dissipation rate of mixing energy
ω	mass fraction of liquid in a subregion of the total mass of liquid in the tank

Subscripts

0	initial concentration
∞	equilibrium concentration
B	bulk phase (or biomass in Figure 34)
CD	complete dispersion
F	gas collection funnel
g	gassed
G	gas
I	gas-liquid interface
i, j, k	index of multiblock model subregion
L	liquid
m	index of chemical compound
max	maximum
min	minimum
mix	mixing
n, p	index of bubble size category
O2	oxygen
P	oxygen probe
ref	reference value
t	total concentration
u	ungassed
X	xanthan

Abbreviations

BSD	bubble size distribution
CFD	computational fluid dynamics
CSP	capillary suction probe
DI	digital imaging (photography)
DO	dissolved oxygen
DSD	daughter size distribution
FBT	flat-blade impeller

MRF	multiple frames of reference technique
MS	mass spectrometry
PB	population balance
PDA	phase Doppler anemometry
PIV	particle image velocimetry
RT	Rushton turbine
VLE	vapour-liquid equilibrium

11. REFERENCES

Aittamaa, J., Keskinen, K.I., *Flowbat – User's instruction manual*, Helsinki University of Technology, 21.6.2005. http://www.tkk.fi/Units/ChemEng/research/Software/index2.html.

Alopaeus, V., Nordén, H.V., A calculation method for multicomponent mass transfer coefficient correlations, *Computers & Chem. Eng.* **23** (1999) 1177-1182.

Alopaeus, V., Koskinen, J., Keskinen, K., Simulation of the population balances for liquid-liquid systems in a nonideal stirred tank. Part 1 Description and qualitative validation of the model, *Chem. Eng. Sci.* **54** (1999a) 5887-5899.

Alopaeus, V., Aittamaa, J., Nordén, H.V., Approximate high flux corrections for multicomponent mass transfer models and some explicit methods, *Chem. Eng. Sci.* **54** (1999b) 4267-4271.

Alopaeus, V., Koskinen, J., Keskinen, K.I., Majander, J., Simulation of the population balances for liquid-liquid systems in a nonideal stirred tank. Part 2 – parameter fitting and the use of the multiblock model for dense dispersions, *Chem. Eng. Sci.* **57** (2002) 1815-1825.

Alopaeus, V., Mass-transfer calculation methods for transient diffusion within particles, *AIChE J.* **46** (2000) 2369-2372.

Alopaeus, V., Laakkonen, M., Aittamaa, J., Solution of population balances with breakage and agglomeration by high-order moment-conserving method of classes, *Chem. Eng. Sci.* **61**(2006) 6732-6752.

Alves, S.S., Maia, C.I., Vasconcelos, J.M.T., Serralheiro, A.J., Bubble size in aerated stirred tanks, *Chem. Eng. J.* **3990** (2002a) 1-9.

Alves, S.S., Maia, C.I., Vasconcelos, J.M.T., Experimental and modelling study of gas dispersion in a double turbine stirred tank, *Chem. Eng. Sci.* **57** (2002b) 487-496.

Amanullah, A., Tuttiett, B., Nienow, A.W., Agitator speed and dissolved oxygen effects in xanthan fermentations. *Biotech. Bioeng.* **57** (1998) 198-210.

Aubin, J., Le Sauze, N., Bertrand, J., Fletcher, D.F., Xuereb, C., PIV measurements of flow in an aerated tank stirred by a down- and up-pumping axial flow impeller. *Exp. Thermal Fluid Sci.* **28** (2004) 447-456.

Bakker, A., van den Akker, H.E.A., A computational model for the gas-liquid flow in stirred reactors. *Chem. Eng. Res. Des.* **72A** (1994), 594-606.

Barigou, M., Greaves M., Bubble size in the impeller region of a Rushton turbine, *Chem Eng. Res. Des.* **70** (1992b) 153-160.

Barigou, M., Greaves, M., Bubble-size distributions in a mechanically agitated gas-liquid contactor. *Chem. Eng. Sci.* **47** (1992a) 2009-2025.

Barigou, M., Greaves, M., Gas holdup and interfacial area distributions in a mechanically agitated gas-liquid contactor, *Chem. Eng. Res. Des.* **74A** (1996) 397-405.

Barker, J.A., Determination of activity coefficients from total pressure measurements, *Austral, J. Chem.* 6 (1953) 207-210.

Bezzo, F., Macchietto, S., Pantelides, C.C., General hybrid multizonal/CFD approach for bioreactor modeling, *AIChE J.* **49** (2003) 2133-2148.

Boyer, C., Duquenne, A.-M. and Wild, G., Measuring techniques in gas-liquid and gas-liquid-solid reactors, *Chem. Eng. Sci.* **57** (2002) 3185-3215.

Brucato, A., Grisafi, F. Montante, G., Particle drag coefficients in turbulent fluids, *Chem. Eng. Sci.* **53** (1998) 3295-3314.

Calderbank, P.H., Physical rate processes in industrial fermentation, Part 1: The interfacial area in gas-liquid contacting with mechanical agitation, *Trans. Inst. Chem. Engrs.* **36** (1958) 443-463.

Chaouki, J., Larachi, F., Dudukovic M.P., Noninvasive and velocimetric monitoring of multiphase flows. *Ind. Eng. Chem. Res.* **36** (1997) 4476-4503.

Chaudhari, R.V., Hofmann, H., Coalescence of gas bubbles in liquids. *Rev. Chem. Eng.* **10** (1994) 131-190.

Chaumat, H., Billet-Duquenne, A.M., Augier, F., Mathieu, C., Delmas, H., Application of the double probe technique to distorted tumbling bubbles in aqueous or organic liquid, *Chem. Eng. Sci.* **60** (2005) 6134-6145.

Chen, P., Sanyal, J., Dudukovic, M.P., Numerical simulation of bubble columns flows: effect of different breakup and coalescence closures, *Chem. Eng. Sci.* **60** (2005) 1085-1101.

Chesters, K.A., The modelling of coalescence processes in fluid-liquid dispersions: A Review of current understanding, *Chem. Eng. Res. Design* **69** (1991) 259-270.

Chigier, N., Optical imaging of sprays, *Prog. Energy Combustion Sci.* **17** (1991) 211-262.

Clift, R., Grace, J.R., Weber, M.E., *Bubbles, Drops and Particles*, Academic Press, London England, 1978.

Costes, J., Couderc, J.P., Study by laser Doppler anemometry of the turbulent flow induced by a Rushton turbine in a stirred tank: Influence of the size of the units – I. Mean Flow and turbulence. *Chem. Eng. Sci.* **43** (1988) 2751-2764.

Coulaloglou, C.A., Tavlarides, L.L., Description of interaction processes in agitated liquid-liquid dispersions. *Chem. Eng. Sci.* **32** (1977) 1289-1297.

Cui, Y.Q., van der Lans, R.G.J.M., Luyben, K.Ch.A.M., Local power uptake in gas-liquid systems with single and multiple Rushton turbines. *Chem. Eng. Sci*. **51** (1996) 2631-2636.

Danckwerts, P.V., Significance of liquid-film coefficients in gas absorption, *Ind. Eng. Chem.* **43** (1951) 1460-1467.

Deen, N.G., Solberg, T., Hjertager, B.H., Flow generated by an aerated Rushton impeller: Two-phase PIV experiments and numerical simulations, *Can. J. Chem. Eng.* **80** (2002) 638-652.

Dhanasekharan, K.M., Sanayal, J., Jain, A., Haidari, A., A generalized approach to model oxygen transfer in bioreactors using population balances and computational fluid dynamics, *Chem. Eng. Sci.* **60** (2005) 213-218.

Elson, T.P., Cheesman, D.J., Nienow, A.W., X-ray studies of cavern sizes and mixing performance with fluids possessing a yield stress, *Chem. Eng. Sci.* **41** (1986) 2555-2562.

Fogg, P.G.T., Gerrard, W., *Solubility of gases in liquids, A critical evaluation of gas/liquid systems in theory and practice*. New York, John Wiley and Sons. 1991.

Frössling N. On the evaporation of falling droplets. *Gerlands Beitage Geophysik*. **52** (1938) 170-216.

Gaddis, E., Vogelpohl, A., Bubble formation in quiescent liquids under constant flow conditions, *Chem. Eng. Sci.* **41** (1986) 97-105.

Galindo, E., Larralde-Corona, C.P., Brito, T., Cordova-Aquilar, M.S., Taboada, B., Vega-Alvarado, L., Corkidi, G., Development of advanced image analysis techniques for the in situ characterization of multiphase dispersions occuring in bioreactors, *J. Biotechnol.* **116** (2005) 261-270.

Garcia-Ochoa, F., Gomez-Castro, E., Santos, V.E.. Oxygen transfer and uptake rates during xanthan gum production, *Enzyme and Microbial Tech*. **27** (2000) 680-690.

Garcia-Ochoa, F., Gomez, E., Theoretical prediction of gas-liquid mass transfer coefficient, specific area and hold-up in sparged stirred tanks, *Chem. Eng. Sci.* **59** (2004) 2489-2501.

Geary, N.W. Rice, R.G.,Bubble size prediction for rigid and flexible spargers, *AIChE J.* **37**: (1991) 161-168.

Genenger, B., Lohrengel, B., Measuring device for gas/liquid flow, *Chem. Eng. Proc.* **31** (1992) 87-96.

Gentric, C., Mignon, D., Bousquet, J., Tanguy, P.A., Comparison of mixing in two industrial gas-liquid reactors using CFD simulations, *Chem. Eng. Sci.* **60** (2005) 2253-2272.

Grau, R.A., Heiskanen, K., Visual technique for measuring bubble size in flotation machines, *Minerals Eng.*, **15** (2002) 507-513.

Gray, J.B., *Mixing-Theory and Practice*, New York: Academic Press, 1966, vol 1, chap 4. pp. 180-184.

Guet, S., Luther, S. and Ooms, G., Bubble shape and orientation determination with a four-point optical fiber probe, *Exp. Therm. Fluid Sci.* **29** (2005) 803-812.

Hagesaether, L., *Coalescence and break-up of drops and bubbles*, Ph.D thesis, Norweigian university of Science and Technology, Trondheim, Norway, 1999, 212 p.

Hagesaether, L., Jakobsen, H.A., Svendsen, H.F., A model for turbulent binary breakup of dispersed fluid particles, *Chem. Eng. Sci.* **57** (2002) 3251-3267.

Hamme, R.C., Emerson, S.R., The solubility of neaon, nitrogen and argon in distrilled water and seawater, *Deep-Sea Research I* **51** (2004) 1517-1528.

Hernandez-Aquilar, J.R., Coleman, R.G., Gomez, C.O., Finch, J.A., A comparison between capillary and imaging techniques for sizing bubbles in flotation systems, *Minerals Eng.* **17** (2004) 53-61.

Hesketh, R.P., Etchells, A.W., Russell, T.W.F., Experimental observations of bubble breakage in turbulent flow, *Ind. Eng. Chem. Res.* **30** (1991a) 835-841.

Hesketh, R.P., Etchells, A.W., Russell, T.W.F., Bubble breakage in pipeline flow, *Chem. Eng. Sci.* **46** (1991b) 1-9.

Higbie, R., The rate of absorption of a pure gas into a still liquid during short periods of exposure, *Trans. Am. Inst. Chem. Engrs.* **31** (1935) 364-389.

Hinze, J.O., Fundamentals of the hydrodynamic mechanism of splitting in dispersion processes, *AIChE J.* **33** (1955) 289-295.

Honkanen, M., Saarenrinne, P., Multiphase PIV method with digital object separation methods, *5th Symp. on Particle Image Velocimetry*, Busan, Korea, 2003.

Honkanen, M., Saarenrinne, P., Turbulent bubbly flow measurements in a mixing vessel with PIV, *11th Int. Symposium on Applications of Laser Techniques to Fluid Mechanics*, Lisboa, 2002, Paper 3.2.

Hristov, H., Mann, R., Lossev, V., Vlaev, S.D., Seichter, P., A 3-D analysis of gas-liquid mixing, mass transfer and bioreaction in a stirred bio-reactor, *Chem. Eng. Res. Des.* **79** (2001) 232-241.

Hsia, A.M., Tavlarides, L.L.,Simulation analysis of drop breakage, coalescence and micromixing in liquid-liquid stirred tanks, *Chem. Eng. J.* **26** (1983) 189-199.

Hu, B., Pacek, A.W., Stitt, E.H., Nienow, A.W., Bubble sizes in agitated air-alcohol systems with and without particles: Turbulent and transitional flow, *Chem. Eng. Sci.* **60** (2005) 6371-6377.

Ishii, M., Zuber, N., Drag coefficient and relative velocity in bubbly, droplet or particulate flows, *AIChE J.* **25** (1979) 843-855.

Jakobsen, H.A., Lindborg, H., Dorao, C., Modeling of bubble column reactors: Progress and limitations. *Ind. Eng. Chem. Res.* **44** (2005) 5107-5151.

Kapic, A., Heindel, T.J., Correlating gas-liquid mass transfer in stirred tank reactor, *Chem. Eng. Res. Des.* **84**(2006) 239-245.

Kawase, Y., Halard, B., Moo-Young, M., Liquid-phase mass transfer coefficients in bioreactors, *Biotech. Bioeng.* **39** (1992) 1133-1140.

Khare, A.S., Niranjan, K., Impeller-agitated aerobic reactor: the influence of tiny bubbles on gas hold-up and mass transfer in highly viscous liquids. *Chem. Eng. Sci.* **50** (1995) 1091-1051.

Khopkar, A.R., Aubin, J., Xuereb, C., Le Sauze, N., Bertrand, J., Ranade, V.V., Gas-liquid flow generated by a pitched-blade turbine: particle image velocimetry measurements and computational fluid dynamic simulations, *Ind. Eng. Chem. Res.* **42** (2003) 5318-5332.

Khopkar, A.R., Rammohan, A.R., Ranade, V.V., Dudukovic, M.P., Gas-liquid flow generated by a Rushton turbine in stirred vessel: CARPT/CT measurements and CFD simulations, *Chem. Eng. Sci.* **60** (2005) 2215-2229.

Kostoglou, M., Karabelas, A.J., Towards a unified framework for the derivation of breakage functions based on the statistical theory of turbulence, *Chem. Eng. Sci.* **60** (2005) 6584-6595.

Kraume, M., Zehner, P., Experience with experimental standards for measurements of various parameters in stirred tanks: A comparative test, *Chem Eng. Res. Des.* **79A** (2001) 811-818.

Kulkarni, A.A., Joshi, J.B., Bubble formation and bubble rise velocity in gas-liquid systems: A review, *Chem. Eng. Res. Des.* **44** (2005) 5873-5931.

Laari, A., Turunen, I., Prediction of coalescence properties of gas bubbles in a gas-liquid reactor using persistence time measurements, *Chem. Eng. Res. Design* **83** (2005) 881-886.

Lane, G.L., Schwarz, M.P., Evans, G.M., Numerical modelling of gas-liquid flow in stirred tanks, *Chem. Eng. Sci.* **60** (2005) 2203-2214.

Lee, C.-H., Erickson L.E., Glasgow, L.A., Bubble breakup and coalescence in turbulent gas-liquid dispersions, *Chem. Eng. Comm.* **59** (1987a) 65-84.

Lee, C.-H., Erickson L.E., Glasgow, L.A., Dynamics of bubble size distribution in turbulent gas-liquid dispersions, *Chem. Eng. Comm.* **61** (1987b) 181-195.

Lehr, F., Millies, M., Mewes, D., Bubble-size distributions and flow fields in bubble columns. *AIChE J.* **48** (2002) 2426-2443.

Lewis, W.K., Whitman, W.G., Principles of gas absorption, *Ind. Eng. Chem.* **16** (1924) 1215-1220.

Linek, V., Kordăc, M., Fujasová, M., Moucha, T., Mass transfer coefficient in stirred tanks interpreted through idealized eddy structure of turbulence in the bubble vicinity, *Chem. Eng. Proc.* **43** (2004) 1511-1517.

Linek, V., Moucha, T., Kordăc, M., Mechanism of mass transfer from bubbles in dispersions Part I: Danckwerts' plot method with sulphite solutions in the presence of viscosity and surface tension changing agents, *Chem. Eng. Proc.* **44** (2005a) 353-361.

Linek, V., Kordăc, M., Moucha, T., Mechanism of mass transfer from bubbles in dispersions Part II: Mass transfer coefficients in stirred gas-liquid reactors and bubble column, *Chem. Eng. Proc.* **44** (2005b) 121-130.

Litster, J.D., Smit, D.J., Hounslow M.J., Adjustable discretized population balance for growth and aggregation. *AIChE J.* **41** (1995) 591-603.

Lo, S., Application of population balance to CFD modeling of gas-liquid reactors, *Trends in Numerical and Physical Modelling for Industrial Multiphase Flows*, Corse, France, 2000.

Luo, H., *Coalescence, break-up and liquid circulation in bubble column reactors*, Dr. Ing. Thesis, Department of Chemical Engineering, The Norwegian Institute of Technology, Trondheim, Norway, 1993.

Luo, H., Svendsen, H.F., Theoretical model for drop and bubble breakup in turbulent dispersions. *AIChE J.* **42** (1996) 1225-1233.

Machon, V., Pacek, A.W., Nienow, A.W., Bubble sizes in electrolyte and alcohol solutions in a turbulent stirred vessel, *Chem Eng. Res. Design* **75A** (1997) 339-348.

Mann, R., Hackett, L.A., Fundamental of gas-liquid mixing in a stirred vessel: An analysis of networks of backmixed models. In *Proceedings of 6th European conference on mixing*, Pavia, Italy, 24-26th May (pp. 321-328). BHRA, 1988.

Marchisio, D.L., Vigil, R.D., Fox, R.O., Quadrature method of moments for aggregation-breakage processes, *J. Colloid Interface Sci.* **258** (2003) 322-334.

Martínez-Bazán, C., Montañés, J.L. and Lasheras, J.C., On the breakup of an air bubble injected into a fully developed turbulent flow. Part 2. Size PDF of the resulting daughter bubbles, *J. Fluid Mech.* **401** (1999) 183-207.

Mavros, P., Flow visualization in stirred vessels – A review of experimental techniques. *Chem Eng. Res. Design* **79A** (2001) 113-127.

Metzner, A.B., Otto, R.E., Agitation of non-newtonian fluids, *AIChE J.* (1957) 1-3.

Middleton, J.C., Gas-liquid dispersion and mixing, in *Mixing in the Process Industries*, eds. Harnby, N., Edwards, M.F., Niewnow, A.W., Butterworth-Heinemann, Oxford 1992, pp. 322-363.

Middleton, J.C., Smith, J.M., Gas-liquid mixing in turbulent systems, in *Handbook of Industrial Mixing: Science and Practice*, eds. Paul, E.L., Atiemo-Obeng, V., Kresta, S.M., Wiley, New York 2004, pp. 585-638.

Miyahara, T., Yamanaka, S., Mechanics of motion and deformation of a single bubble rising through quiescent highly viscous newtonian and non-newtonian media, *J. Chem. Eng. Jpn* **26** (1993) 297-302.

Morud, K.E., Hjertager, B.H., LDA measurements and CFD modelling of gas-liquid flow in stirred vessel, *Chem. Eng. Sci.* **51** (1996) 233-250.

Narsimhan, G., Gupta, J.P., Ramkrishna D., A model for transitional breakage probability of droplets in agitated lean liquid-liquid dispersions. *Chem. Eng. Sci.* **34** (1979) 257-265.

Nienow, A.W., Wisdom, D.J., Middleton, J.C., 1977, The effect of scale and geometry on flooding, recirculation, and power in gassed stirred vessels, *2nd European Conference on Mixing*, Stephens, H.S., Clarke, J.A. (Eds), (BHRA Fluid Engineering, England), paper F1.

Nilars, M.S., Spragge, P. and Tuck, C., In-flight measurements of droplets sizes from agricultural nozzles, a comparison of two commonly used laser systems, *8th Int. Conf. of Liquid Atomization and Spray Systems*, 2000, Pasadena, USA.

Otake, T., Tone, S., Nakao, K., Mitsuhashi, Y., Coalescence and breakup of bubbles in liquids, *Chem. Eng. Sci.* **32** (1977) 377-383.

Pacek, A.W., Nienow, A.W., Measurement of drop size distribution in concentrated liquid-liquid dispersions: Video and capillary techniques, *Chem Eng. Res. Des.* **73** (1995) 512-517.

Poizat, T., Jallut, C., Accary, A., Lieto, J., A novel experimental technique for measurement of mass transfer between liquids and gas bubbles in agitated vessels: Application to highly viscous liquids, *Chem. Eng. J.* **48** (1992) 41-48.

Poling, B.E., Prausnitz, J.M., O'Connell, J.P., *The properties of gases and liquids,* McGraw-Hill, New York, 2000.

Poorte, R.E.G, Biesheuvel, A., Experiments on the motion of gas bubbles in turbulence generated by an active grid, *J. Fluid Mech.* **461** (2002) 127-154.

Prince, M.J., Blanch H.W., Bubble coalescence and break-up in air-sparged bubble columns. *AIChE J.* **36** (1990) 1485-1499.

Ramkrishna, D., *Population balances: theory and applications to particulate systems in engineering*, Academic Press, San Diego, 2000.

Ranade, V.V., *Computational flow modeling for chemical reactor engineering*, Academic Press, San Diego, USA 2002.

Ranade, V.V., Joshi, J.B., Flow generated by a disc turbine: Part I Experimental, *Chem. Eng. Res. Des.* **68** (1990) 19-30.

Ranade, V.V., Perrard, M., Xuereb, C., Le Sauze, N., Bertrand, J., Influence of gas flow rate on the structure of trailing vortices of a Rushton turbine: PIV measurements and CFD simulations, *Chem. Eng. Res. Des.* **79** (2001) 957-964.

Revill, B.K., Pumping capacity of disc turbine agitators. A literature review, in *Proceedings of the 4th European Conference on Mixing*, BHRA Fluid Engineering, Noordwijkerhout, The Netherlands, pp. 11-24.

Risso, F. Fabre, J., Oscillations and breakup of a bubble immersed in a turbulent field, *J. of Fluid Mech.* **372** (1998) 323-355.

Ruchti, G., Dunn, I.J., Bourne, J.R., Practical quidelines for the determination of oxygen transfer coefficients (KLa) with the sulfite oxidation method, *Chem. Eng. J.* **30** (1985) 29-38.

Schäfer, M., Wächter, P., Durst, F., Experimental investigation of local bubble size distributions in stirred vessels using Phase Doppler Anemometry, In: *10th European Conference on Mixing (2000)*, Van den Akker, H.E.A., Derksen J.J. (Eds.), Elsevier, Delft, The Netherlands, pp. 205-212.

Sridhar, T., Potter, O.E., Interfacial areas in gas-liquid stirred vessels, *Chem. Eng. Sci.* **35** (1980) 683-695.

Takahashi, K., Nienow, A.W., Bubble sizes and coalescence rates in an aerated vessel agitated by a Rushton turbine, *J. Chem. Eng. Jpn*, **26** (1992) 536-542.

Tatterson G.B., Fluid mixing and gas dispersion in agitated tanks. New York: McGraw-Hill, 1991.

Taylor, R., Krishna, R., *Multicomponent Mass Transfer*, Wiley, New York 1993.

Tomiyama, N., Struggle with computational bubble dynamics, *Third international conference on Multiphase Flow, ICMF 98*, Lyon, France, 1998.

Tzounakos, A., Karamanev, D.G., Margaritis, A., Bergougnou, M.A., Effect of the surfactant concentration on the rise of gas bubbles in power-law non-newtonian liquids, *Ind. Eng. Chem. Res.* **43** (2004) 5790-5795.

Uusi-Kyyny, P., Pokki, J.P., Laakkonen, M., Aittamaa, J., Liukkonen, S., Vapor-Liquid equilibrium for the binary systems 2-methylpentane+ 2-butanol at 329.2 K and n-hexane + 2-butanol at 329.2 K and 363.2 K with a static apparatus, *Fluid Phase Equilib.* **201** (2002) 343-358.

Valentas, K.J., Amundson, N.R., Breakage and coalescence in dispersed phase systems. *Ind. Eng. Chem. Fund.* **5** (1966) 533-542.

Van't Riet, K., Review of measuring methods and results in nonviscous gas-liquid mass transfer in stirred vessels. *Ind. Eng. Chem. Process Des. Dev.* **18** (1979) 357-364.

Van't Riet, K., Smith, J.M., The behaviour of gas-liquid mixtures near Rushton turbine blades, *Chem. Eng. Sci.* **28** (1974) 1031-1037.

Vasconcelos, J.M.T., Alves, S.S., Barata, J.M., Mixing in gas-liquid contactors agitated by multiple turbines. *Chem. Eng. Sci.* **50** (1995) 2343-2354.

Venneker, B.C.H., Derksen, J.J., Van den Akker, H.E.A., Population balance modelling of aerated stirred vessels based on CFD, *AIChE J.* **48** (2002) 673-685.

Vlaev, D., Mann, R., Lossev, V., Vlaev, S.D., Zahradnik, J., Seichter, P., Macro-mixing and streptomyces fradiae – Modelling oxygen and nutrient segregation in an industrial bioreactor, *Chem. Eng. Res. Des.* **78** (2000) 354-362.

Vlaev, S.D., Valeva, M.D., Mann, R.. Some effects of rheology on the spatial distribution of gas holdup in a mechanically agitated vessel, *Chem. Eng. J.* **87** (2002) 21-30.

Vrábel, P., van der Lans, R.G.J.M., Luyben, K.C.A.M., Boon, L., Nienow, A.W., Mixing in large-scale vessels stirred with multiple radial or radial and axial up-pumping impellers: modelling and measurements, *Chem. Eng. Sci.* **55** (2000) 5881-5896.

Walter, J.F., Blanch, H.W., Bubble break-p in gas-liquid bioreactors: break-up in turbulent flows, *Chem. Eng. J.* **32** (1986) B7-B17.

Wang, T., Wang, J., Jin, J., Population balance model for gas-liquid flows: Influence of bubble coalescence and breakup models, *Ind. Eng. Chem. Res.* **44** (2005) 7540-7549.

Wang, T., Wang, J., Jin, Y., A novel theoretical breakup kernel function for bubbles/droplets in a turbulent flow, *Chem. Eng. Sci.* **58** (2003) 4629-4637.

Weissenberger, S., Schumpe, A., Estimation of gas solubilities in salt solutions at temperatures from 273 K to 363 K, *AIChE Journal* **42** (1996) 298-300.

Wellek, R.M., Arawal, A.K., Skelland, A.H.P., Shapes of liquid drops moving in liquid media, *AIChE J.* **12** (1966) 854-862.

Wells, G.J., Ray, W.H., Methodology for modeling detailed imperfect mixing effects in complex reactors. *AIChE J.* **51** (2005) 1508-1520.

Wilke, C.R., Chang, P., Correlation of diffusion coefficients in dilute solutions, *AIChE J.* **1** (1955) 264-270.

Wilkinson, P.M., Schayk, A., Spronken, J.P.M., Dierendonck, L.L., The influence of gas density and liquid properties on bubble breakup, *Chem. Eng. Sci.* **48** (1993) 1213-1226.

Yawalkar, A.A., Heesink, A.B.M., Versteeg, G.F., Pangarkar, V.G., Gas-liquid mass transfer coefficient in stirred tank reactors, *Can. J. Chem. Eng.* **80** (2002) 840-848.

Zahradnik, J., Mann, R., Fialova, M., Vlaev, D., Vlaev, S.D., Lossev, V., Seichter, P., A network-of-zones analysis of mixing and mass transfer in three industrial bioreactors, *Chem. Eng. Sci.* **56** (2001) 485-492.

Zlokarnik, M., *Stirring – Theory and Practice*, Wiley-VCH, Weinheim, Germany 2001.